Mesoscopic physiological interactions in the human brain reveal small-world properties and associations with behavior

A DISSERTATION PRESENTED
BY
JIARUI WANG
TO
THE DEPARTMENT OF THE DIVISION OF MEDICAL SCIENCES

IN PARTIAL FULFILLMENT OF THE REQUIREMENTS
FOR THE DEGREE OF
DOCTOR OF PHILOSOPHY
IN THE SUBJECT OF
BIOLOGICAL AND BIOMEDICAL SCIENCES

HARVARD UNIVERSITY
CAMBRIDGE, MASSACHUSETTS
MAY 2021

©2021 – JIARUI WANG

ALL RIGHTS RESERVED.

Thesis advisor: Professor Gabriel Kreiman Jiarui Wang

Mesoscopic physiological interactions in the human brain reveal small-world properties and associations with behavior

ABSTRACT

Cognition depends on rapid and robust communication between neural circuits spanning different brain areas. Here we investigated the mesoscopic network of cortico-cortical interactions in the human brain in an extensive dataset consisting of 6,024 hours of intracranial field potential recordings from 4,142 electrodes in 48 subjects. Communication between brain areas was evaluated in a pairwise fashion and at the network level across different frequency bands. The interaction networks were validated against known anatomical measurements and neurophysiological interactions in humans and monkeys. The resulting human brain interactome is characterized by a broad and spatially specific, dynamic, and extensive. The physiological interactome revealed small-world properties, which we conjecture might facilitate efficient and reliable information transmission. The interaction dynamics correlate with the brain sleep/awake and also with natural behaviors. These results constitute initial steps towards understanding how the interactome orchestrates cortical communication and provide a reference for future efforts to assess how dysfunctional interactions may lead to mental disorders.

Contents

Figures

Tables

Acknowledgements

Nothing in this dissertation would have been possible without the help and support from the following people. I want to thank everyone at the University who have passed on their valuable experience and invested in my development through countless hours of conversations, lectures, and discussions. I would like to thank Anne O'Shea, Daniel Gonzalez, Kate Hodgins, and Professor Susan Dymecki in the Biological and Biomedical Sciences office who made my education experience enjoyable. I would like to thank my program advisor Professor Bruce Zetter for his patience and for introducing me to my thesis advisor. I would like to thank Professors Dominic Walsh and Michael Rogers for providing critical feedback on my dissertation proposal drafts. I would like to thank Professors Tracy Young-Pearse, Pascal Kaeser, and Sandeep Robert Datta for serving on my qualifying exam and encouraging me to examine the historical foundations of neuroscience. I would like to thank Professors Connie Cepko, Wei-Chung Lee, Richard Born, and Randy Buckner for providing feedback and support during our many Dissertation Advisory Committee sessions, especially Randy Buckner for meeting with me to develop my understanding of neuroanatomy. I would like to finally thank my thesis advisor Professor Gabriel Kreiman for passing on his fierce commitment to scientific principles, for investing countless hours to my scientific development, and for believing in my mission every day for the past six years.

I would like to thank my collaborators for all that they have contributed to making this dissertation possible. I would like to thank Professor Monica Rosenberg for her initiative and dedication in bringing the behavioral annotation project from a summer school idea into reality, and Eleonora Iaselli for her commitment to continuing the behavior project. I would like to thank Alyssa Marconi, Jacklyn Sarette, and Meredith Alfred for the heroic task of annotating behaviors.

I would like to thank Jay Chandra and Elisa Pavarino for their continued patience working with the complex behavioral annotations. I would like to thank Vishal Kapoor and Wu "Will" Xiao for their initiative and dedication in experimenting with graph theory analysis. I would like to thank Annabelle Tao for her initiative in bringing the sleep project from start to finish, for her committed persistence over the last 4 years, and for always constructively challenging my philosophical views. I would like to thank Dr. Phillip Pearl, Dr. Joseph Madsen, Dr. William Anderson, Dr. Eun-Hyong Park, Dr. Daniel Weisholtz, Melissa Kiernan, Michael Gunnuscio, and Rebecca FitzGerald for sharing their clinical expertise. I would like to thank fellow lab members Jie Zheng, Nimrod Shaham, and David Mazumder for painfully reading through my manuscript and providing meticulous feedback. Finally, I would like to thank my dissertation examination committee, Professors Randy Buckner, Henry Kennedy, Jan Drugowitsch, and Margaret Livingstone, for their dedication in scrutinizing my thesis.

I would like to thank my fellow lab members for sharing their perspectives during our daily conversations and for helping me see my work from a broader perspective. I would like to thank Pranav Misra and Katarina Bendtz for always being available to help in times of need. I would like to thank Mengmi Zhang and Jie Zheng for being great officemates and for making difficult days feel easy. I would like to thank Vincent Jacquot and Charlotte Moerman for their patience in introducing me to European values. I would like to thank my fellow graduate student classmate Joseph Olson for 5 years of his unconditional friendship and support. I would like to thank my mom and dad for sharing their experiences from graduate school.

I would like to thank the numerous people I have met over the years who have made undeniable contributions to my scientific thinking: Professor Michael Arcaro, William Lotter, Leyla Isik, Jiye Kim, Frederico Azevedo, Martin Schrimpf, Leonardo Pollina, Yuchen Xiao,

Emma Krause, Elizabeth Shtrahman, Andrzej Banburski, Daniel Estandian, Alexi Choueiri, Luis Seoane, Maxwell Collard, Darian Hadjiabadi, Gang Wang, Simon Kluters, Rudger Hess, Jens Smiatek, and Joey Studts. I would like to thank all my classmates in the BBS and HBTM programs for their friendship and support. I would like to thank all the people at the Center for Brains, Minds, and Machines for creating a diverse research environment. To all those who have sacrificed their valuable time and convenience to make me the best version of myself, I am forever in your debt.

Introduction

Computational neuroscience occasionally likes to entertain itself with the useful metaphor that the brain is the computer of the human body, using terms like “algorithms”, “circuits”, and “coding/decoding” (Churchland, 1992). The study of how different parts of the brain interact during tasks (Gregoriou et al., 2009; Madhavan et al., 2019; Zhou et al., 2016) provided an empirical foundation for network neuroscience (Bassett and Sporns, 2017), and today there are many who find the internet to be a useful metaphor (Graham, 2021). Thus, cognitive computations rely on the transformation of signals and communication between brain areas.

Neuronal communication between brain areas correlates with computation and behavior in non-human animals (Bastos et al., 2015; Gregoriou et al., 2009; Womelsdorf et al., 2007) and humans (Baldauf and Desimone, 2014; Michalareas et al., 2016). Furthermore, computational models of cognition require communication between different processing stages (Zhao, 2016). However, neurophysiological investigations of brain function have largely focused on individual brain areas. At least partly, the emphasis on individual brain areas has been dictated by the use of single electrodes or multielectrode arrays that target a limited region of the brain. In humans, multiple single-neuron studies (Fried et al., 2014) and field potential studies (Schwiedrzik et al., 2018) have characterized the activity of individual brain areas in isolation, while fewer studies have measured correlations between two areas (Fu et al., 2019; Madhavan et al., 2019).

Anatomical connectivity patterns provide essential clues about the *potential* flow of information between brain areas. Long-range anatomical connections between brain areas have been reported through tract tracing studies in monkeys (Felleman and Van Essen, 1991; Gămănuţ et al., 2018; Markov et al., 2012). Studies of anatomical connections in humans are challenging

(Sparks et al., 2000): only a small number of post-mortem analyses have been conducted (Burkhalter and Bernardo, 1989), revealing connectivity over limited distances. Anatomical studies constrain the potential mechanisms of communication between brain areas, but do not reveal dynamics (Hutchison et al., 2013), and in which frequency ranges those interactions occur (Bastos et al., 2015).

Non-invasive studies capitalize on the ability to study the human brain from the outside. Diffusion tensor imaging methods produce probabilistic maps of putative white matter tracts (Assaf and Pasternak, 2008). Scalp electroencephalography (EEG) (Nolte et al., 2004) methods have provided indirect measures of macroscopic correlations. Functional magnetic resonance imaging (fMRI) (Baldauf and Desimone, 2014; Glasser et al., 2016; Power et al., 2011; Thomas Yeo et al., 2011) represent the overwhelming majority of published works on mesoscopic networks in the human brain. Although fMRI techniques are statistically robust and capable of collecting data in large quantities, their coarser spatiotemporal sensitivity, shorter durations of recordings, and smaller range of behaviors do not eliminate the need for invasive studies (Logothetis et al., 2001).

While examining correlations between brain areas has provided important insights about computation in specific tasks, the large-scale study of interactions affords the possibility of evaluating communication in the whole network (Barabási and Albert, 1999; Bassett and Bullmore, 2017; Bullmore and Sporns, 2009; Graham, 2021; Muldoon et al., 2016; Sporns et al., 2005; Watts and Strogatz, 1998). Here we quantify the interactions between human brain areas at the *mesoscopic* level. We analyzed an extensive dataset comprising intracranial field potentials (IFP) from patients diagnosed with pharmacologically intractable epilepsy; the IFPs were continuously recorded for 0.9 to 10.4 days. IFP recordings show high signal-to-noise ratio signals

with millisecond temporal resolution and millimeter spatial resolution (Buzsáki et al., 2012; Crone et al., 2006; Dubey and Ray, 2019). IFP studies have identified key neurophysiological features that correlate with cognitive and behavioral functions (Anumanchipalli et al., 2019; Dubey and Ray, 2019). We validated the methodology by comparing both anatomical and functional interactions from data in macaque monkeys.

Previous studies of mesoscopic networks examined resting state interactions over short periods spanning several seconds to minutes (Betzel et al., 2019; Fox et al., 2020; Keller et al., 2014; Solomon et al., 2017; Trebaul et al., 2018), except for one study that followed 6 subjects for almost a whole day each (Kramer et al., 2011). By examining interactions between 148,404 electrode pairs in 48 subjects over week-long continuous recordings, we provide an extensive neurophysiological characterization of long-range interactions between brain areas in the human brain. The resulting network shows that interactions in the human brain follow a log-normal distribution, are correlated with structural constraints, and demonstrate small-world properties, whereby information can rapidly and flexibly travel from any one area to another. This work is accompanied by a Supplementary Website where it is possible to scrutinize interactions in each electrode pair and each pair of brain areas, both in individual subjects and a common brain (http://braininteractome.com).

Chapter 1

Preprocessing and validation of interactions

Introduction

Neuroscientists are indebted to Penfield for pioneering the technique of invasively recording extracellular electric potentials from the surface of the brain (Penfield and Rasmussen, 1950). In recent times, we have discovered the exciting ability to synthesize speech from physiological recordings (Anumanchipalli et al., 2019). Similar to how studies of the biophysical nature of the blood-oxygen-level-dependent signal have enabled analytical optimization of fMRI spatiotemporal resolution (Logothetis et al., 2001), simultaneously-recorded single unit and intracranial field potential (IFP) responses have played a crucial role in maximizing resolution in intracranial studies (Dubey and Ray, 2016) (Dubey and Ray, 2019). Advancements in our understanding of the organization of brain areas (Glasser et al., 2016) and electrode localization methods (Groppe et al., 2017) provide the opportunity to maximize anatomical resolution. There is ongoing work to define and evaluate metrics of interactions between pairs of IFP signals (Stepaniants et al., 2020). Recent studies of mesoscopic physiological interactions in the human brain (Betzel et al., 2019; Casimo et al., 2016; Fox et al., 2020; Keller et al., 2014; Kramer et al., 2011; Solomon et al., 2017; Trebaul et al., 2018) use a variety of data preprocessing methods

(Parvizi and Kastner, 2018), and thus provide an opportunity for designing an optimized preprocessing pipeline.

Methods that enable the analysis of large quantities of data have allowed researchers to study longer behaviors such as sleep (Muller et al., 2016) and spontaneous, naturalistic behaviors (Wang et al., 2016). Recent studies of mesoscopic physiological interactions have been able to study at most an average of 46 hours per subject and a total of 276 hours (Kramer et al., 2011). We designed a preprocessing pipeline that was able to handle a dataset size of an average of 125 hours per subject and a total of 6024 hours by leveraging the latest technologies in computer hardware and software. In addition to optimizing our choices of preprocessing methods, we validated our pipeline with IFP recordings from a macaque monkey (Yanagawa et al., 2013).

Results

Definition of pairwise interactions

We examined IFP recordings from 48 subjects with pharmacologically resilient epilepsy (3 to 47 years old, 42% female, 90% right-handed, **Table 1**).

Subject	Age	Gender	Hemisphere	Handedness	Days	Electrodes	Bipolar Electrodes
1	21	M	L	R	6.0	72	63
2	14	M	L	R	5.6	72	63
3	3	F	R	R	5.5	104	91
4	32	M	R	R	6.4	72	63
5	46	F	L	R	3.5	72	63
6	10	F	L	R	4.3	88	77
7	20	F	R	R	5.1	88	77
8	39	F	R	R	7.0	72	63
9	47	M	R	R	5.6	48	42
10	21	M	R	L	5.8	70	61
11	26	M	R	R	2.0	72	63

12	18	M	R	R	5.2	64	56
13	9	F	L	R	5.2	72	63
14	32	M	R	L	3.8	40	35
15	21	M	L	R	7.5	72	63
16	8	M	L	L	4.5	128	112
17	10	F	L	R	6.4	104	91
18	9	M	R	R	3.8	104	91
19	18	F	L	R	6.5	120	105
20	15	M	R	R	5.1	80	70
21	12	M	R	R	6.2	104	91
22	17	F	L	R	6.6	56	49
23	9	F	R	R	6.6	88	77
24	16	M	R	R	4.6	104	91
25	9	M	R	R	2.7	104	91
26	17	F	L,R	R	10.4	104	91
27	3	M	L	R	6.8	88	77
28	11	F	L	R	6.6	72	63
29	19	M	L	R	3.7	128	112
30	44	M	R	R	2.4	26	20
31	31	M	R	R	7.3	34	27
32	42	F	R	R	4.3	38	32
33	18	M	R	R	8.8	88	77
34	31	M	L	R	3.8	75	65
35	16	M	L	R	1.3	88	77
36	18	F	L	R	5.1	88	77
37	18	M	L	R	3.1	72	63
38	19	F	L	R	5.7	120	105
39	11	M	L	L	5.6	104	91
40	17	F	R	R	5.2	176	154
41	31	F	L	R	4.6	79	68
42	16	F	L	R	4.6	96	84
43	13	M	L	L	5.7	92	80
44	14	F	L	R	6.4	72	63
45	10	F	R	R	0.9	112	98
46	7	M	L	R	7.8	120	105
47	10	M	R	R	6.4	120	105
48	17	M	R	R	1.7	80	70

Table 1. List of subjects (n = 48).

Age, gender, handedness, and left/right hemisphere coverage are shown with the number of days of continuous intracranial field potential (IFP) recordings, number of electrodes, and number of bipolar electrodes (see Methods for bipolar electrode definition).

We analyzed continuous IFPs recorded for 0.9 to 10.4 days (5.2 ± 1.8, here and throughout, mean ± SD), from 4,142 electrodes (86±28 electrodes per subject, **Table 1**). The electrode

positions in each subject are illustrated in **Figure 1,** and the anatomical areas covered are listed in **Table 2**.

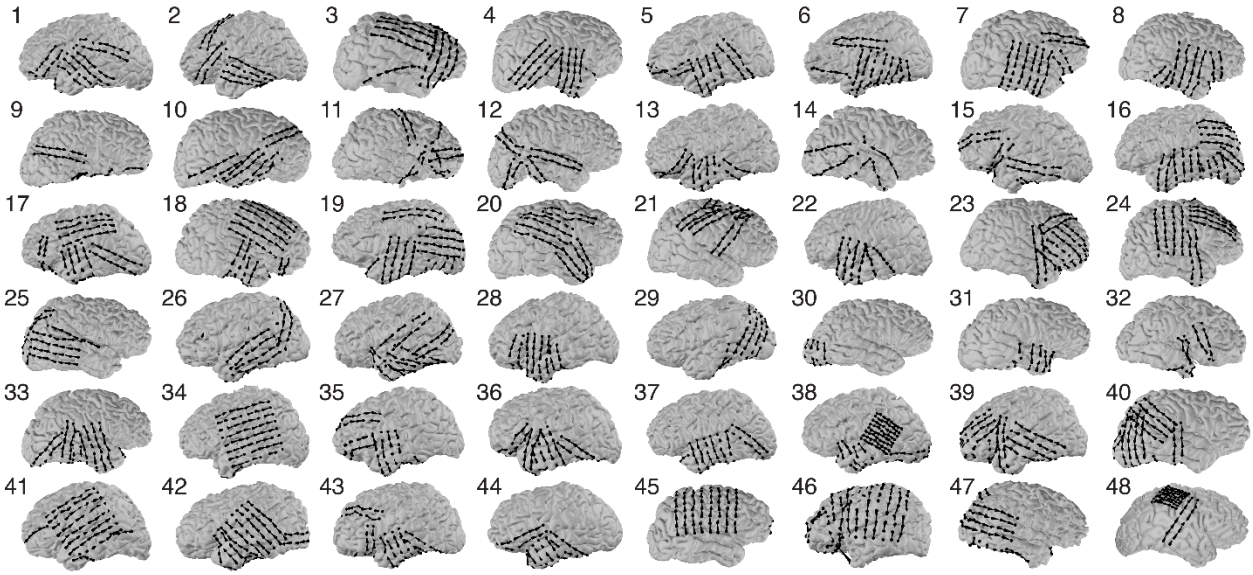

Figure 1. Location of electrodes in each of the 48 subjects.

Locations with respect to the reconstructed pial surfaces of 4,142 electrodes (black dots) in 48 subjects. Arrow markers join the two physical electrodes that were used to compute each bipolar referenced signal. An average of 86 ± 28 electrodes was implanted per subject (min: 26, max: 176). The number of electrodes per subject is shown in **Table 1** and a summary of electrode locations is shown in **Table 2**.

Desikan-Killiany Region	Abbreviation	Alias	Bipolar Electrodes	(%)	Left Hemisphere	Right Hemisphere
Middle Temporal	MTP	middletemporal	462	12.8%	297	165
Inferior Temporal	ITP	inferiortemporal	399	11.0%	263	136
Superior Temporal	STP	superiortemporal	330	9.1%	200	130
Fusiform	FUS	fusiform	266	7.4%	185	81
Rostral Middle Frontal	RMF	rostralmiddlefrontal	220	6.1%	97	123
Lateral Occipital	LOC	lateraloccipital	174	4.8%	90	84
Supramarginal	SMA	supramarginal	171	4.7%	84	87
Precentral	PRC	precentral	155	4.3%	60	95
Postcentral	PSC	postcentral	140	3.9%	52	88
Inferior Parietal	IPA	inferiorparietal	127	3.5%	47	80
Superior Frontal	SFR	superiorfrontal	117	3.2%	28	89
Lingual	LIN	lingual	115	3.2%	44	71
Lateral Orbitofrontal	LOF	lateralorbitofrontal	112	3.1%	71	41
Entorhinal	ENT	entorhinal	96	2.7%	69	27
Temporal Pole	TPP	temporalpole	83	2.3%	40	43
Pars Opercularis	POP	parsopercularis	80	2.2%	42	38

Precuneus	PCU	precuneus	75	2.1%	29	46
Pars Orbitalis	POR	parsorbitalis	71	2.0%	41	30
Pars Triangularis	PTR	parstriangularis	63	1.7%	44	19
Parahippocampal	PHC	parahippocampal	61	1.7%	52	9
Superior Parietal	SPA	superiorparietal	58	1.6%	17	41
Caudal Middle Frontal	CMF	caudalmiddlefrontal	49	1.4%	16	33
Cuneus	CUN	cuneus	38	1.1%	6	32
Isthmus Cingulate	ICN	isthmuscingulate	29	0.8%	14	15
Medial Orbitofrontal	MOF	medialorbitofrontal	28	0.8%	12	16
Paracentral	PCE	paracentral	23	0.6%	0	23
Posterior Cingulate	PCN	posteriorcingulate	21	0.6%	7	14
Frontal Pole	FRP	frontalpole	16	0.4%	7	9
Unknown	UNK	unknown	10	0.3%	5	5
Bank of Superior Temporal Sulcus	BST	bankssts	8	0.2%	4	4
Caudal Anterior Cingulate	CAC	caudalanteriorcingulate	7	0.2%	2	5
Pericalcarine	PCL	pericalcarine	6	0.2%	0	6
Corpus Callosum	CCA	corpuscallosum	3	0.1%	3	0
Rostral Anterior Cingulate	RAC	rostralanteriorcingulate	2	0.1%	0	2
Transverse Temporal	TVT	transversetemporal	0	0.0%	0	0
Insula	INS	insula	0	0.0%	0	0
		Total:	3615	100%	1928	1687

Table 2. Number of bipolar electrodes covering each area in the Desikan-Killiany parcellation (Desikan et al., 2006).

Three-letter abbreviations (as shown in **Figure 19**) and their *freesurfer* names are shown with the number of bipolar electrodes localized to those areas. After applying the coverage criteria (see **Methods**), 31 areas remained covered for physiological interaction network analyses (bolded).

We implemented rigorous and conservative pre-processing steps to ensure that the recordings were free from potential artifacts (**Methods**): (i) bipolar referencing (Shirhatti et al., 2016); (ii) custom algorithm to remove artifacts (**Table 3**, **Figure 2**); (iii) focus on seizure-free epochs; (iv) restriction to non-adjacent electrode pairs (**Figure 3**) (Nunez et al., 1997). A detailed description of each of these steps and their importance to ensure the high fidelity of the recordings is presented in the **Methods** section.

Criterion	Total	Mean (n=48)	Standard deviation	Minimum	Maximum

Amplitude, large (i)	0.72%	0.71%	1.4%	<0.01%	5.9%
Slope (ii)	0.44%	0.38%	0.63%	<0.01%	3.6%
Amplitude, small (iii)	0.10%	0.13%	0.45%	0%	2.9%
Events (iv)	0.49%	0.68%	1.8%	0%	10.5%
Electrodes (v)	0.34%	0.36%	0.36%	<0.01%	1.4%
Total	2.1%	2.3%	2.6%	<0.01%	12.1%

Table 3. Percentage of artifacts removed according to each criterion.

The total fraction of observed 1-second segments of IFP recordings marked as artifacts. Segments could satisfy more than one criterion, with the exception of (i) and (iii). The overall fraction of annotated artifacts was 2.1%. Please see **Methods** for definitions and **Figure 2** for illustration of the different types of artifacts

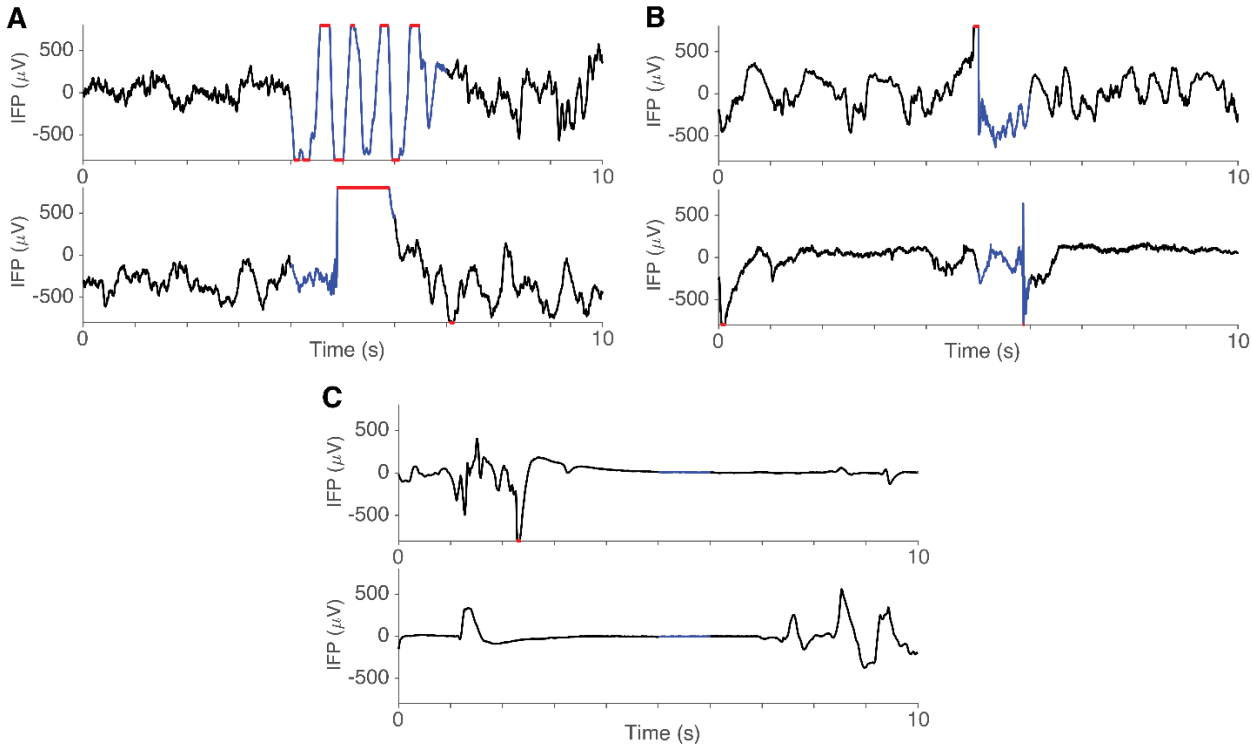

Figure 2. Examples of artifacts removed from analyses.

Artifacts were detected according to 3 criteria (**Methods**) and removed from analyses. We present 2 example 10-second segments from 2 electrodes for each criterion (artifacts are marked by blue lines superimposed on the IFP voltage traces shown in black, out-of-range points are indicated in red). (**A**) Large amplitude events where $\max[V(t)] - \min[V(t)] > 2000$ μV (0.72% of total events). Red markers indicate time points where the voltage values were out of the scale chosen here for illustration purposes only (± 800 μV). (**B**) Large slope events where the maximum rate of change in voltage over time exceeded a threshold of 100 μV/ms (0.44% of total events). (**C**) Low amplitude events where $\max[V(t)] - \min[V(t)] < 10$ μV (0.10% of

total events). In total, 2.1% of the data were marked as potential artifacts (95-percentile range across subjects: 1.4% to 11%).

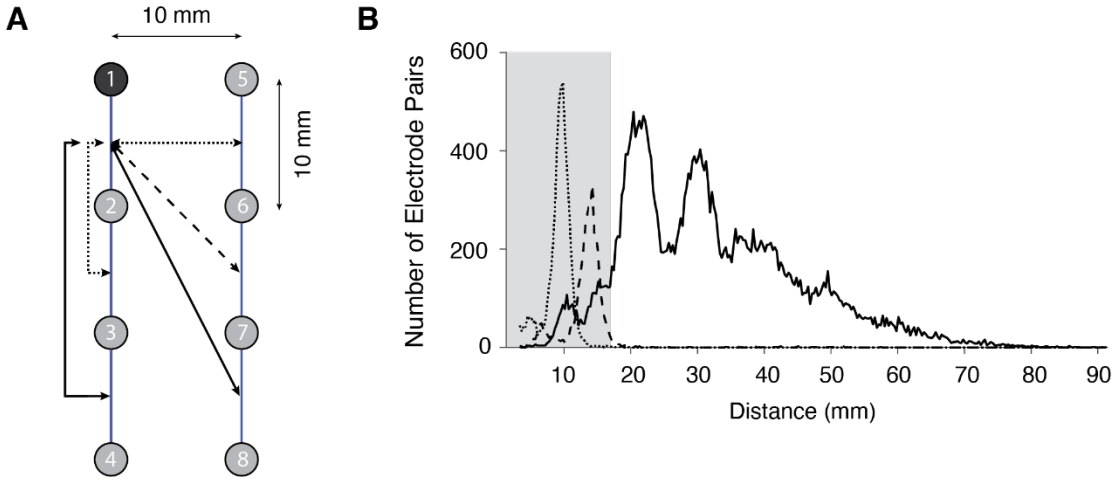

Figure 3. Nearby electrodes were excluded from analyses.

(**A**) Example schematic layout of 8 physical electrodes shown on a 4 by 2 grid. The blue lines show pairs of electrodes used for bipolar referencing (**Methods**). Focusing on electrode 1 (top left), the voltage was calculated with respect to electrode number 2. Here we show all five possible pairs for this electrode. Adjacent neighbors (dotted lines) and diagonal neighbors (dashed line) were excluded from analyses. The two remaining interactions (solid lines) were included in the analyses. (**B**) Histogram of the distance between electrodes that were adjacent neighbors (dotted line), diagonal neighbors (dashed line), or otherwise (solid line). The shaded region indicates pairs of bipolar-referenced electrodes that were less than 17 mm apart, which were excluded from analyses (**Methods**). The peaks at 20 and 30 mm reflect the typical geometry of electrode grids and strips.

We studied 148,404 electrode pairs over a total of 6,024 hours. To explain the methodology step-by-step, we start by showing an illustrative example 10-second segment of IFP signals from two electrodes, one in the right Superior Temporal gyrus and one in the right Pars Opercularis (**Figure 4A**). We defined the relationship between the IFP signals from these two electrodes by calculating the degree of coherence, which ranges from 0 to 1 (**Methods**). Throughout the manuscript, we refer to the coherence as a metric of *interaction* between the two signals (Bastos

et al., 2015; Madhavan et al., 2019; Zhou et al., 2016) (**Discussion**). We focus on interactions in the broadband frequency range (0.5 - 125 Hz, **Methods;** see below for coherence values in the gamma frequency band (**Figure 5, Figure 16, Figure 17**, **Figure 23**, **Figure 25, Figure 26, Figure 27**, **Table 4**) and see the Supplementary Website for other frequency bands). The coherence between the two signals in **Figure 4A** was 0.36. We computed coherence in non-overlapping windows over the whole duration of continuous recordings of up to 10.4 days (**Figure 4B-C**).

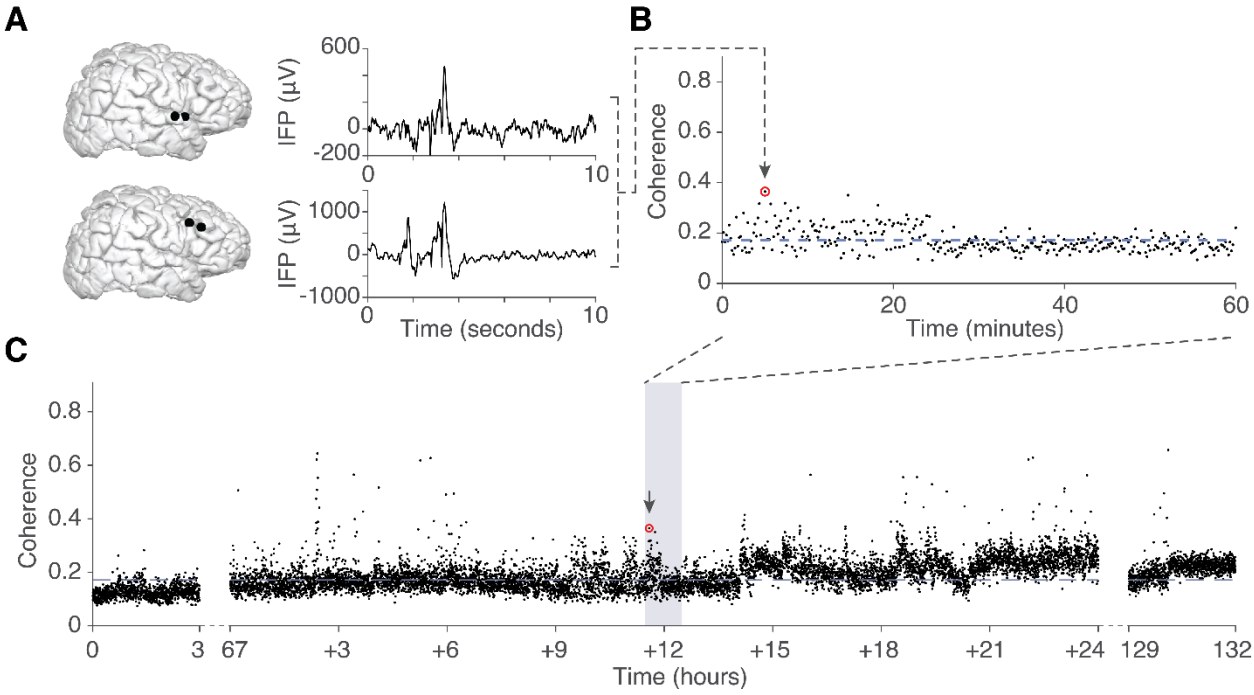

Figure 4. Example recordings and definition of interactions.

(**A**) Example pair of bipolar referenced intracranial field potentials (IFP) over a 10-second time window from subject 3. One bipolar electrode pair was located in the right Superior Temporal gyrus (top) and the other bipolar electrode pair was located in the right Pars Opercularis (bottom). The coherence between these two signals was 0.36. (**B-C**) Coherence was calculated in consecutive 10-second windows (represented by dots). A zoomed-in segment of 60-minute duration (gray rectangle in **C**) around the 10-second segment in **A** is shown in **B**. **C**. Coherence was calculated for the entire ~5.5 days of recordings. Part **C** shows a segment of 24 hours around the interval shown in **B** (note the two cuts in the x-axis).The arrows in **B**, and **C** mark the segment in **A**. The horizontal dashed lines indicate the coherence under the null hypothesis (**Methods**).

Validation of pairwise interactions

We assessed the statistical significance of coherence measurements by comparing them with a null model whereby we randomly shifted one of the signals in time (**Figure 6**, **Methods**). Inserting random temporal shifts in one of the two electrodes ensured that the statistical properties of the individual signals remained intact while removing any temporal structure leading to interactions. The coherence in **Figure 6A** decreased from 0.36 to 0.05 following the shifting procedure (**Figure 6A-D**). This approach defined a significance threshold for the coherence for each electrode pair (horizontal dashed lines in **Figure 6E-F**).

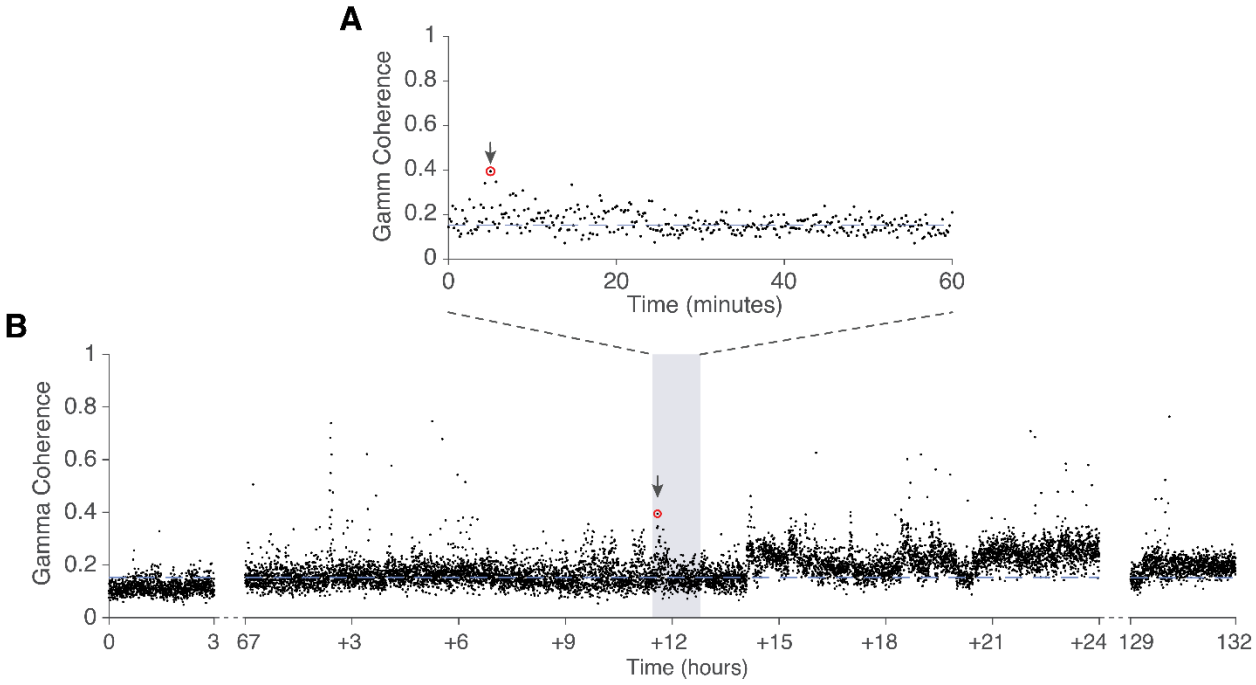

Figure 5. Example IFP recordings filtered in the gamma frequency band.

Extending **Figure 4** in the main text, this figure shows coherence between IFP activity from the same pair of electrodes filtered in the gamma frequency band [30,100) Hz. Format and conventions follow those in **Figure 4**. The gamma band coherence for the segment in **Figure 4A**

was 0.39 (arrow in (**A**)). The gamma band coherence is shown over 60 minutes (**A**) and over 24 hours (**B**).

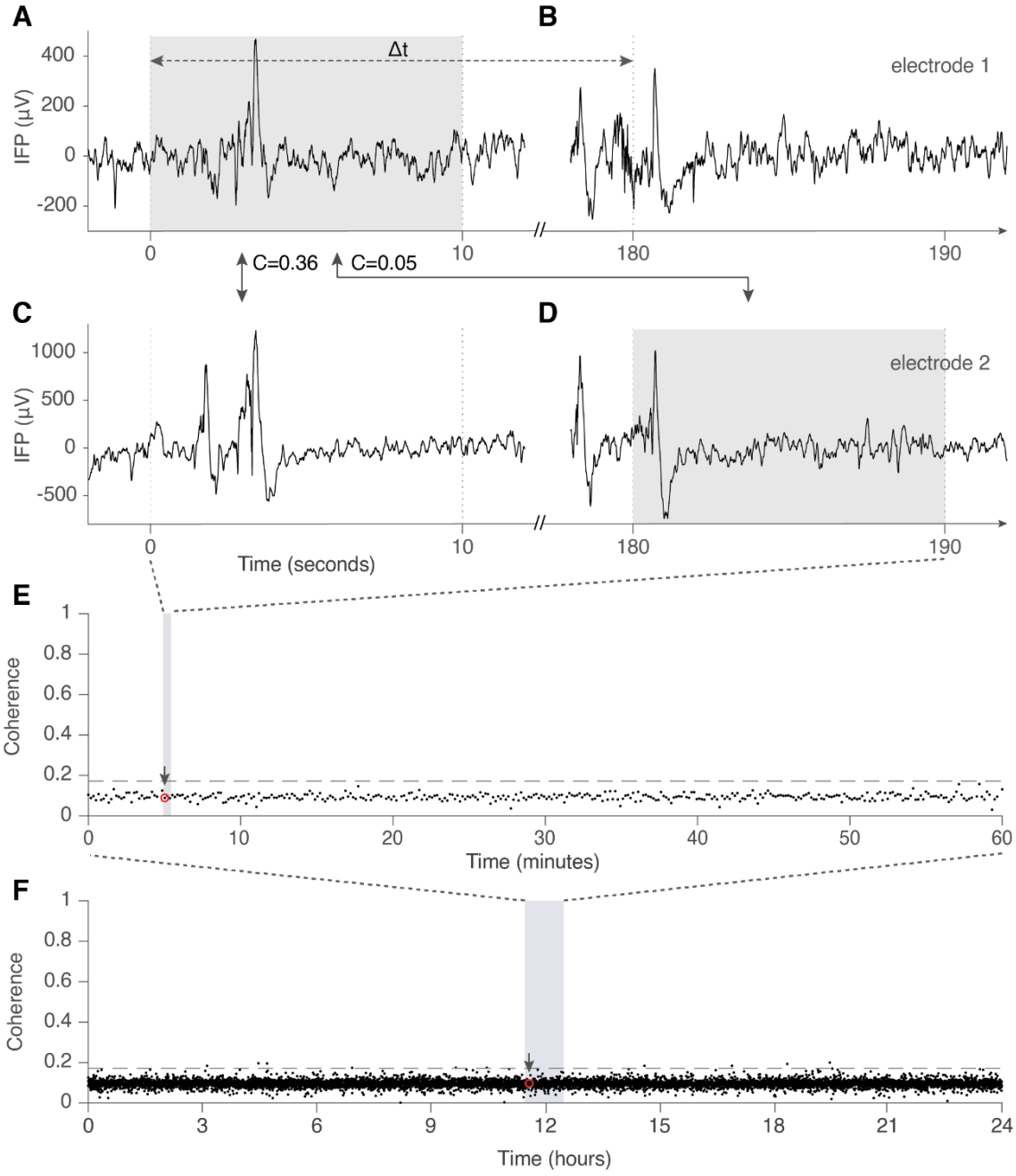

Figure 6. Null hypothesis defined by temporally shifting neural signals.

Segments of data from two electrodes (**A-B**: electrode 1, **C-D**: electrode 2). The segment in (**A**) was simultaneously recorded with the segment shown in (**C**). The coherence between these two segments was 0.36. We considered a random time shift Δt, in this case, $\Delta t = 180$ seconds (note the cut along the x-axis). The coherence between the segment in (**A**) and the one in (**D**) was 0.05. Electrode locations are the same as in **Figure 4A**. (**E-F**) The same procedure was repeated at

each time point using random values of Δt Δt, leading to the distribution of coherence values under the null hypothesis for 24 hours in (**F**), and the zoomed-in one-hour segment in (**E**). The horizontal dashed lines indicate the significance threshold C=0.17 (**Methods**). The arrows in (**E**) and (**F**) indicate the example coherence between the (**A**) and (**D**) segments.

We validated the use of coherence as a measure of neural interactions using anatomical and neurophysiological data from monkeys. We focused on monkey measurements for validation to leverage tract tracing studies of long-range anatomical connectivity (Markov et al., 2012) (**Figure 7A**), and known inter-areal neurophysiological interactions (Bastos et al., 2015; Zhou et al., 2016). We analyzed resting state neurophysiological data from 128 intracranial electrodes implanted throughout the macaque cortical surface (Yanagawa et al., 2013), computing pairwise interactions for every pair of electrodes using the same analyses as for the human dataset (**Figure 7B**, **Methods**). Electrode positions were localized to 39 areas in the Markov-Kennedy parcellation (Markov et al., 2012).

As a first validation test, we compared the pairwise interactions with anatomical connectivity (Markov et al., 2012) (**Figure 7A**). There was a weak but significant correlation between the anatomical connectivity matrix (**Figure 7A),** and the physiological interaction matrix (**Figure 7B**, Spearman correlation coefficient = 0.28; $p=1x10^{-8}$, two-sided t-test) after regressing out inter-electrode distances. Despite the differences between structural connectivity and physiological interactions, and the limited behavioral repertoire of the physiological recordings, the network described using the coherence metric approximated known long-range anatomical connections derived from tracing studies.

The second validation test examined transient interactions between brain areas while monkeys performed cognitive tasks, as positive controls to evaluate whether we could find evidence of those interactions using our metrics. We focused on two studies that documented interactions between visual areas V1 and V4, and between V1 and TEO (Bastos et al., 2015), and

also between V4 and TEad/TEpd (Zhou et al., 2016). In the resting state data, we found 44, 54, and 15 electrode pairs that mapped onto V1-V4, V1-TEO, and V4-TEad/pd, respectively. Of these, 100%, 94%, and 100%, respectively, showed interactions according to our metrics (**Figure 7F, H**). These high percentages were remarkable given the methodological differences across labs and studies, and especially given that we compared transient interactions over hundreds of milliseconds during cognitive tasks (Bastos et al., 2015; Zhou et al., 2016) against interactions evaluated over hours of resting-state recordings.

In the third validation test, we evaluated these same interactions between monkey visual cortical areas in the continuous human neurophysiological data. We used putative homologies to map the locations of electrodes on the monkey cortical surface onto human cortical surface coordinates (Van Essen, 2004) (**Methods**, **Figure 7C-E**). We found 248, 32, and 67 electrode pairs that mapped onto putative homologs of the V1-V4, V1-TEO, and V4-TEad/pd regions, respectively. Of these electrode pairs, 43%, 19%, and 4% demonstrated interactions in the human brain (**Figure 7F, H**). Despite the extrapolation across temporal scales, across species, and across experimental conditions, the coherence metric was able to detect interactions that were consistent with those previously reported in the literature.

As a final validation test, we evaluated whether the coherence metric was valid when reporting the *absence* of interactions. Negative controls are more challenging to find due to potentially infrequent or weak interactions that may be difficult to detect (Markov et al., 2012), and due to reporting biases favoring positive interactions. As a coarse approximation to a negative control, we considered pairs of areas that do *not* show anatomical connectivity (Markov et al., 2012): V1-area 2 (not to be confused with area V2), V1-area 5 (not V5), and V4-F5. We found 72, 27, and 20 pairs of electrodes, respectively, in the monkey resting-state neural data that mapped

onto those locations. Of those electrode pairs, 4%, 4%, and 0% showed significant interactions (**Figure 7G,I)**; these percentages are well below the 100%, 94%, and 100% reported in **Figure 7F,H**. We also found 27, 34, and 6 electrode pairs in the human data that mapped onto these locations. None of those electrode pairs showed significant interactions (**Figure 7G,I)**, in stark contrast with the 43%, 19%, and 4% values reported in **Figure 7F,H**.

In sum, coherence constitutes a reasonable metric to assess interactions between brain areas: the values were unlikely to arise by chance (**Figure 6**), the interactions correlate with anatomical measures (**Figure 7A-B**), and interactions measured from both human and monkey recordings are consistent with positive (**Figure 7F, H)** and negative (**Figure 7G, I)** neurophysiological and neuroanatomical examples from previous studies.

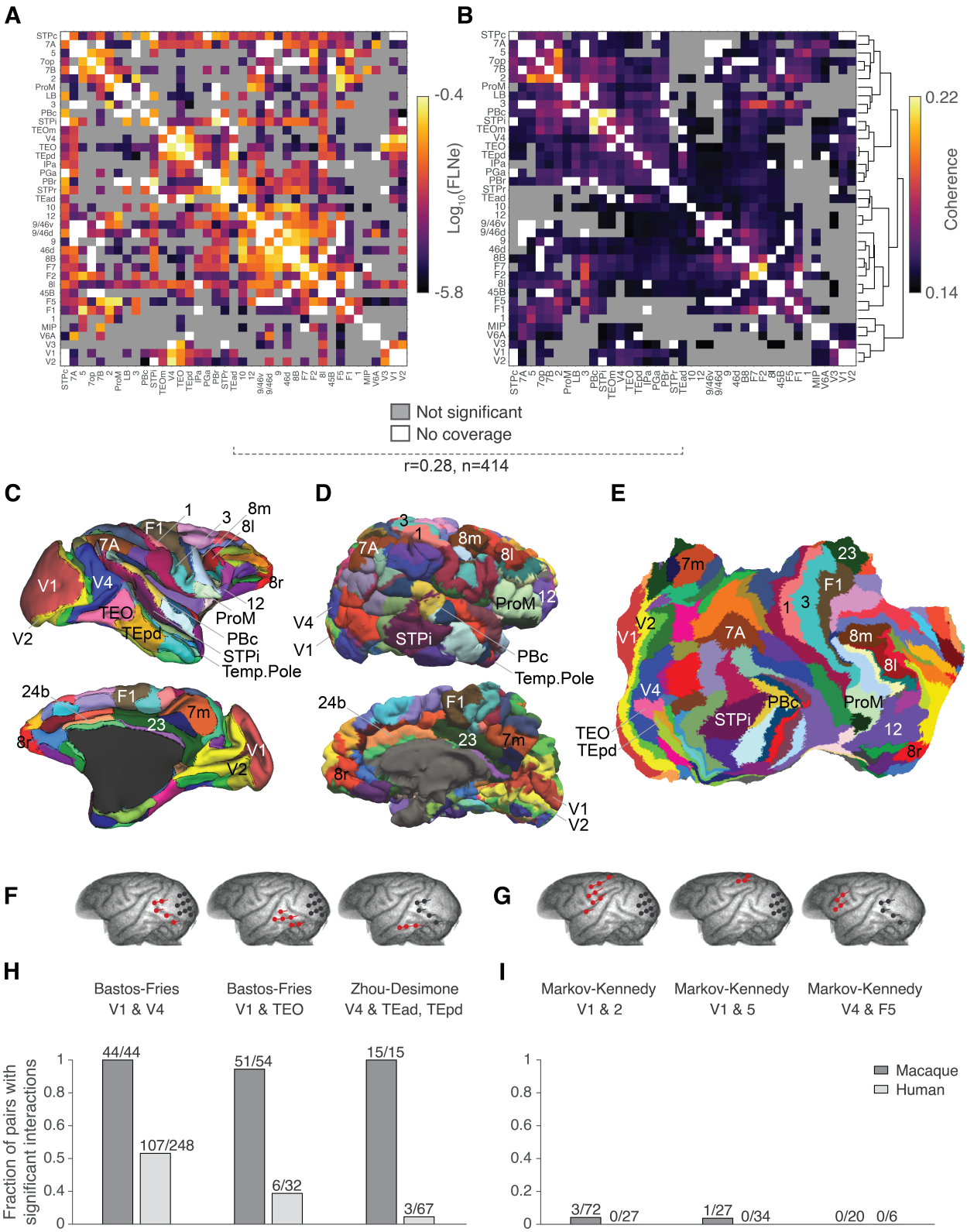

Figure 7. Validation using intracranial recordings in macaque monkeys.

(**A-B**) Comparison between neurophysiological recordings and neuronal tracing studies in monkeys. (**A**) Known anatomical cortico-cortico connections between 39 macaque monkey brain areas based on the M132 atlas (Markov et al., 2012). Entry (i, j) in this matrix shows the log of the symmetrized normalized fraction of neurons ($\log_{10}$ FLNe) projecting from area i to area j (see (Markov et al., 2012) for details). The color scale is shown on the right. (**B**) Summary of physiological interactions in the macaque monkey brain based on intracranial recordings from (Yanagawa et al., 2013) for the same 39 brain areas shown in **A**. The methodology to compute coherence is the same as the one described in the text for human data (**Methods**). Electrode positions were mapped onto the 39 corresponding brain areas used in the Markov-Kennedy connectivity atlas. Entry (i, j) in this matrix shows the degree of coherence between electrodes placed in area i and area j, the color scale is shown on the right. White entries denote location pairs where we did not have coverage in either anatomy (**A**) or neurophysiology (**B**). Gray entries denote location pairs where there were no significant anatomical connections (**A**) or physiological interactions (**B**). The Spearman correlation coefficient between the upper triangular matrix in (**A**), anatomical connections, and in (**B**), physiological interactions, was 0.28 ($p = 1 \times 10^{-8}$), controlling for interelectrode distances. The dendrogram in **B** displays the degree of similarity between areas according to hierarchical clustering on the coherence values (see **Figure 14** and **Methods**). A shorter horizontal fork length indicates higher similarity.

(**C-E**) **Mapping between human brain locations and macaque brain locations**. (**C**) Lateral view (top) and medial view (bottom) of macaque cortical areas (reproduced from Figure 1 in (Markov et al., 2012)). Each color denotes a different brain area, some of the area names are labeled. (**D**) The pial surface from human subject 3 was mapped to the 91-area Markov-Kennedy parcellation for interspecies comparisons. (**E**) The surface in **D** cut and flattened. Colors in (**D-E**) correspond to the brain areas in **C**. Inter-species registration was generated using the caret package (Van Essen et al., 2001) and flat maps were generated using the freesurfer package (Dale et al., 1999) (**Methods**).

(**F-I**) **Known physiological interactions in the macaque monkey were found in human and monkey neural recordings.** (**F**) Example macaque intracranial electrode locations from 2 studies that reported physiological interactions between a pair of brain areas (Bastos et al., 2015; Zhou et al., 2016). The locations shown are the macaque ECoG electrodes nearest to the originally reported locations in the corresponding studies. (**G**) Example macaque intracranial electrode locations from 3 pairs of areas that are not anatomically connected according to the tracing study of Markov *et al*. (Markov et al., 2012). Lines indicate the locations of bipolar references. (**H**) For each of the regions in the 2 studies in (**F**), we considered all possible electrodes in the macaque ECoG data (Yanagawa et al., 2013). We report here the proportion of electrode pairs that showed significant interactions (dark gray bars, see number of significant electrode pairs and total number of electrode pairs above each bar). Additionally, using the maps described in (**C-E**), we considered all the electrodes in our human intracranial field potential recordings. We report here the proportion of electrode pairs in the human data that showed significant interactions (light gray bars). (**I**) Number of electrode pairs showing significant interactions for the pairs of areas with no known anatomical connection as shown in (**G**). A larger fraction of interacting electrode pairs was found in electrodes with previously reported interactions (**H**) versus in electrode pairs with reported absences of anatomical tracts (**I**), both in macaque and humans. Pairs of areas with a reported absence of anatomical tracts showed lower average coherence compared to pairs of areas that were known to interact.

Mesoscopic interactions are dynamically modulated and spatially localized

We return to the 10-second IFP segment for the example electrode pair in **Figure 4A**. Other 10-second segments (**Figure 9**) show coherence values ranging from no statistical significance (**Figure 9A**) to typical coherence values (**Figure 9D**), to strong interactions (**Figure 9C**). Coherence measurements for a one-hour segment are shown in **Figure 4B**, and coherence measurements for a 24-hour segment within the whole period of 5.5 days are shown in **Figure 4C**. We considered the fraction of all 10-second windows that showed statistically significant coherence values as a measure of temporal consistency (**Methods**). Throughout the one-hour segment shown in **Figure 4B**, this electrode pair showed significant coherence 39% of the time. **Figure 8** shows the fraction of time that electrodes showed significant interactions for each pair of brain areas (**Methods**). Over 5.5 days, the temporal consistency was 41%, with a coherence averaged over significant segments of 0.22±0.05. In subsequent figures, we focus on this time-averaged coherence value as a summary metric. We define a pair of electrodes to show significant interactions when the temporal consistency was above 5%.

After examining the temporal dynamics of physiological interactions, we evaluated the degree of spatial specificity. We asked whether the interaction illustrated in **Figure 4A** was spatially restricted by considering IFPs from other locations. **Figure 10** shows three other electrodes that were simultaneously recorded with the electrode pair in **Figure 4**. None of the other 6 possible coherence measurements between the two ten-second segments shown in **Figure 4** and the three ten-second segments in **Figure 10B** reflected significant interactions. The maximum coherence for these 6 non-significant pairs was 0.13, compared to 0.36 for the interaction between

the example electrode pair in **Figure 4**. Of the 91 bipolar electrodes for this subject, there were 44 electrodes where we could evaluate potential interactions with the two electrodes in **Figure 4** after applying the exclusion criteria for both electrodes. Of these 44 electrodes, 8 (18%) showed significant coherence with one but not the other electrode, 22 (50%) showed significant coherence with both, and 14 (32%) did not show significant coherence with either (including the 3 electrodes in **Figure 10B**). In sum, both electrodes showed spatially selective interactions with only a specific subset of the other simultaneously recorded electrodes.

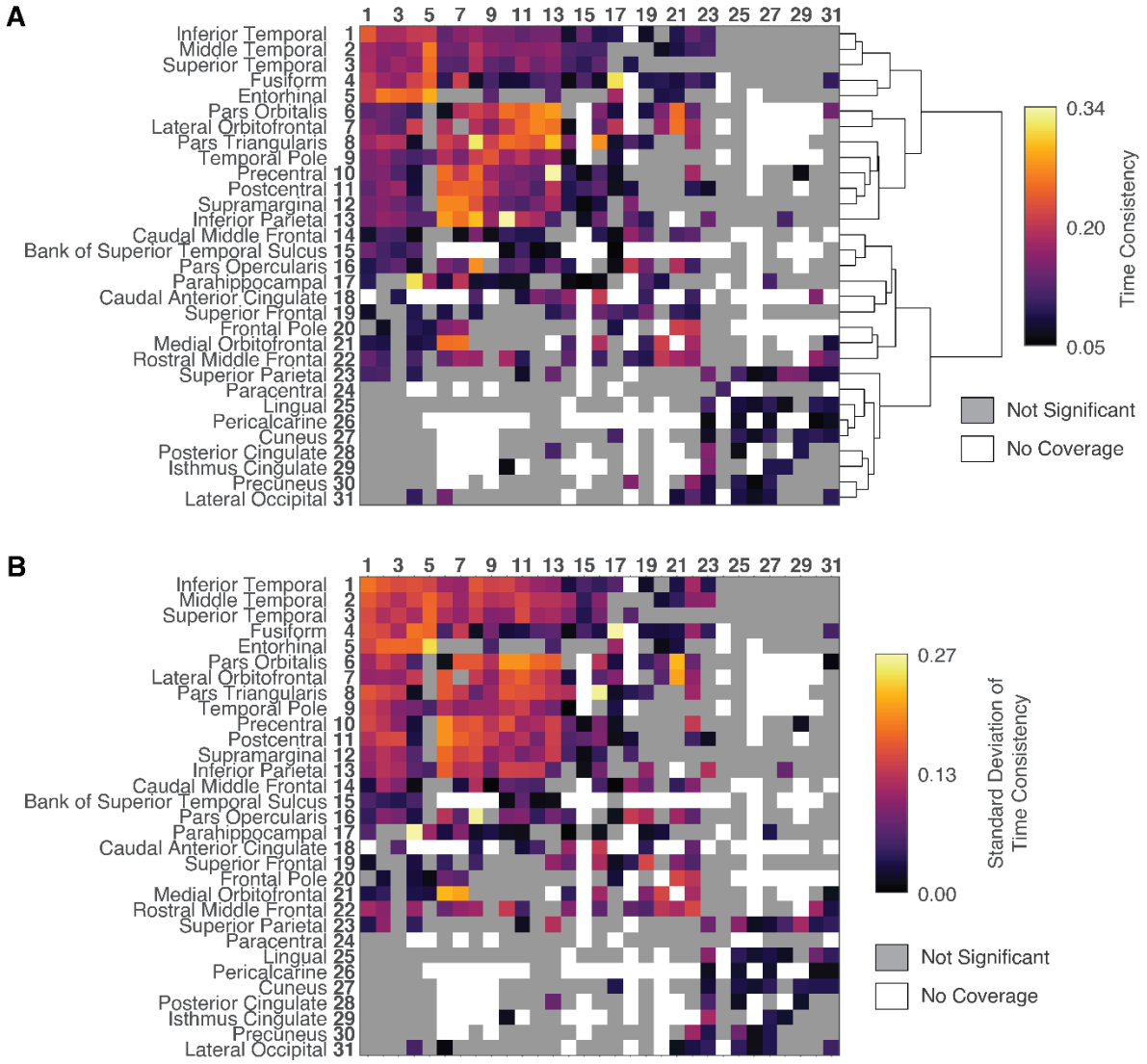

Figure 8. Time consistency of physiological interactions.

Following the format from Figure 4, the fraction of time showing significant interactions between Desikan region pairs is shown in (A), and the standard deviation of time consistency is shown in (B). The hierarchical clustering dendrogram on the right shows the relationship between Desikan-Killiany areas based on their similarities in time consistency with other areas (Methods).

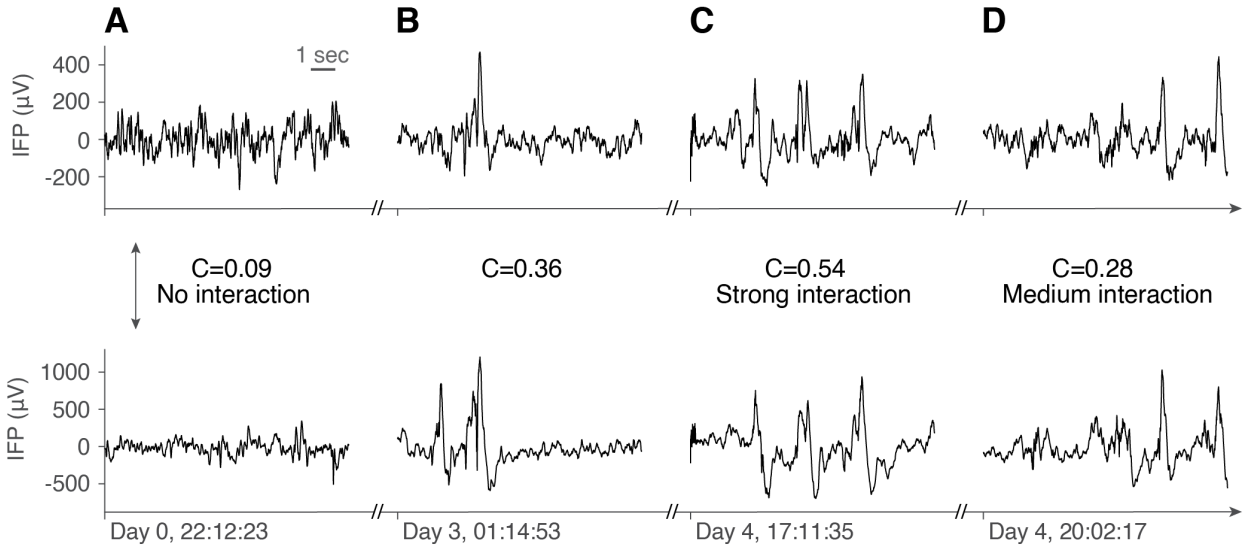

Figure 9. Coherence values change over time.

Following the format in **Figure 4**, here we show four 10-second segments spanning multiple days from the same two cortical areas (top: right Superior Temporal gyrus; bottom: right Pars Opercularis) (note cut along the x-axis). (**A**) Non-significant coherence (C=0.09), (**B**) Segment shown in **Figure 4A** (C=0.36). (**C**) High coherence segment (C=0.54). (**D**) Medium coherence segment (C=0.28).

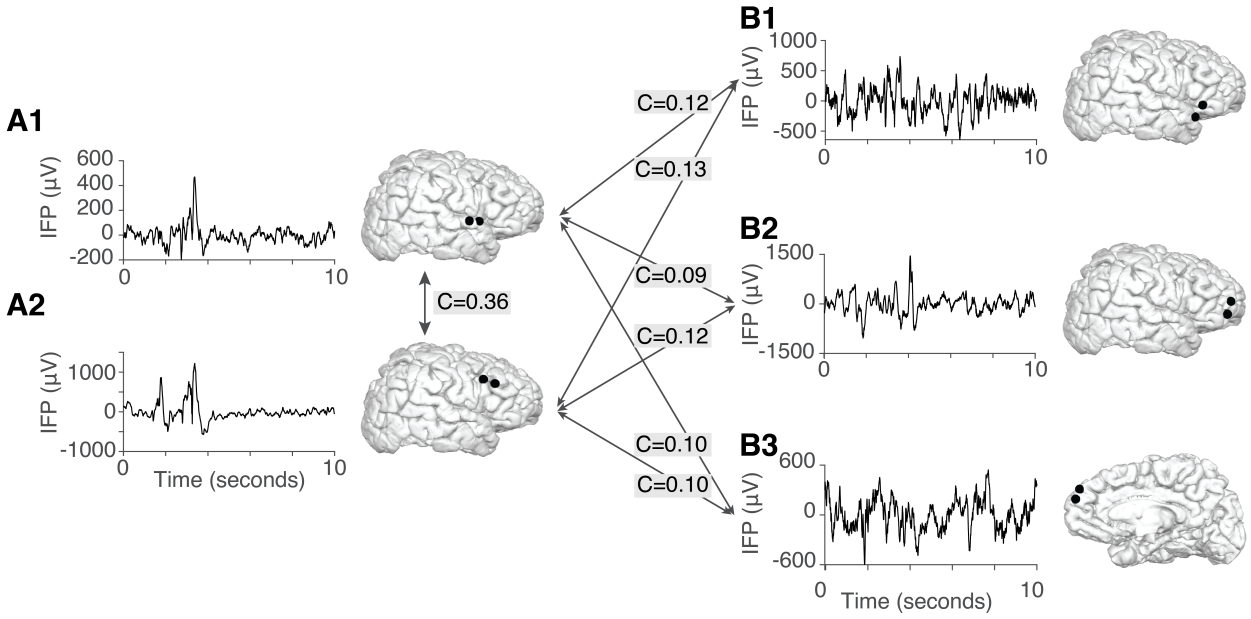

Figure 10. Physiological interactions show spatial specificity.

(**A**) Reproduction of **Figure 4A** in the main text for comparison. The coherence between the two bipolar electrode pairs in this segment was 0.36. (**B**) Three bipolar electrode pairs located in the left superior temporal gyrus, left rostral middle frontal gyrus, and left post-central gyrus, simultaneously recorded with the ones in (**A1/A2**). None of the 6 coherence values between (**A1/A2**) and (**B1/B2/B3**) were statistically significant.

We extended the study of spatial specificity from these example ten-second segments to time-averaged coherences calculated over the entire duration of recordings. In the same electrode pair as in **Figure 4A** and **Figure 11A**, we illustrate in **Figure 11B** all interactions for the electrode in the Superior Temporal gyrus (**Figure 4A**, top). This electrode interacted with 20 of the 75 electrodes remaining after applying the distance exclusion criterion (27%, **Figure 3**). Similarly, **Figure 11C** shows the 23 significant interactions out of 60 electrodes (38%) for the electrode in the Pars Opercularis (**Figure 4A**, bottom). Both electrodes showed spatially selective interactions with only a subset of other simultaneously-recorded electrodes.

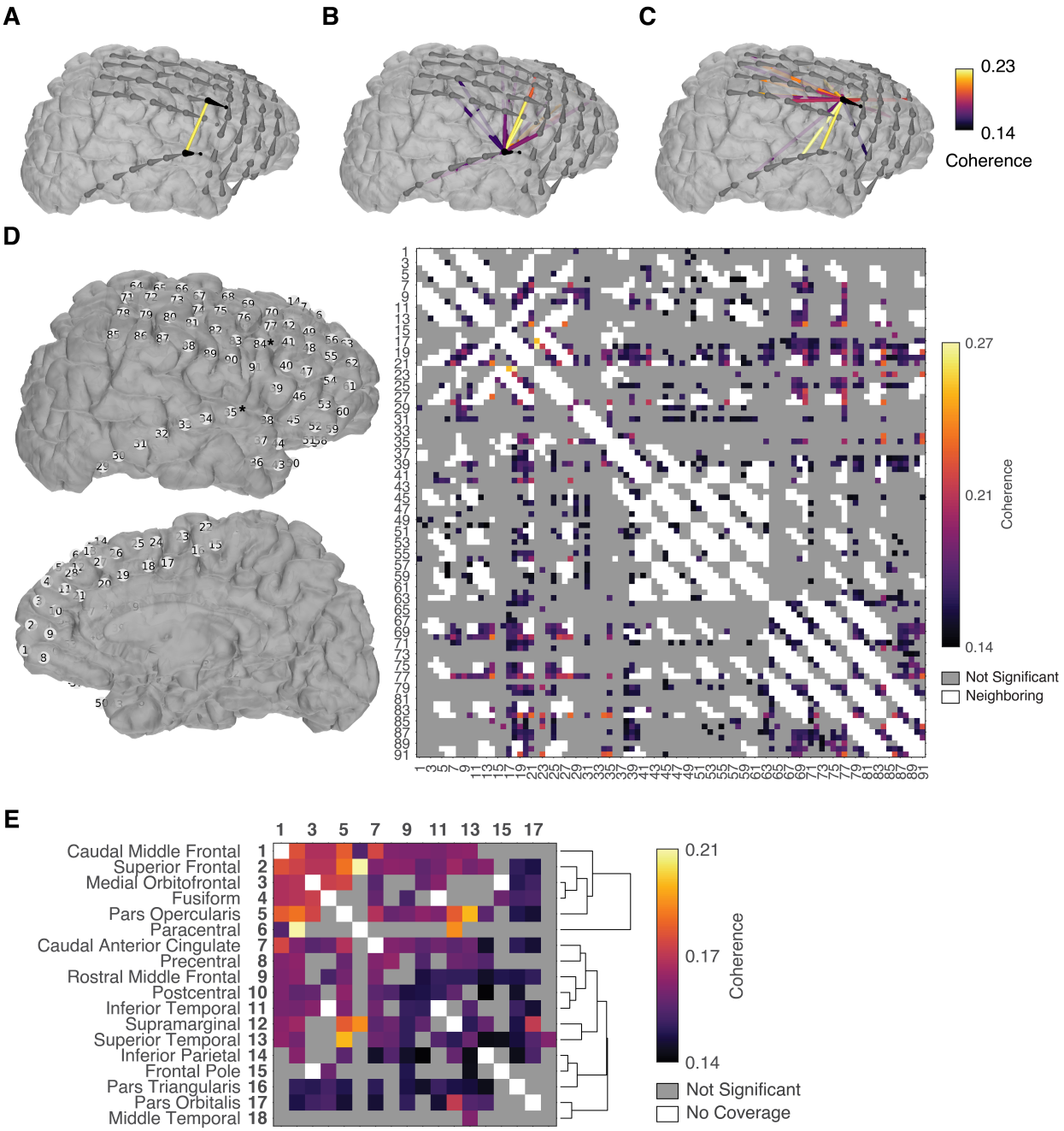

Figure 11. Time-averaged coherence values show spatial specificity.

All interactions shown here are measured by the time-averaged coherence in subject 3 for 5.5 days. Bipolar electrode pairs are indicated by the droplet-shaped markers where the head indicates the primary electrode and the tail points to the ground electrode. (**A**) The bipolar pair from **Figure 4A** are indicated in black. The time-averaged coherence was 0.22 and is represented by a colored line connecting the two bipolar electrode positions (dark circles, other bipolar electrodes are denoted by light circles). (**B**) All interactions with the electrode in the Superior Temporal gyrus from (**A**). (**C**) All interactions with the electrode in the Pars Opercularis from (**A**). (**D**) Interactions shown for all 91 electrodes in this subject (see electrode locations on the

left and color scale on the right). Of the 4,095 total possible pairwise combinations, 3,193 pairs satisfied the distance constraint (**Figure 3**). A total of 557 pairs (17%) showed statistically significant and temporally consistent interactions. (**E**) Interactions shown between all electrode pairs in this subject mapped onto the brain areas defined by the Desikan-Killiany parcellation (Desikan et al., 2006). The dendrogram shows relationships between areas, based on their similarities in coherence values. The interaction between the Superior Temporal gyrus and Pars Opercularis (**A**) can be found in row 18, column 2.

Discussion

We defined a preprocessing pipeline and metric for evaluating putative physiological interactions of the human cortex. We measured coherence between IFPs recorded from pairs of bipolar intracranial electrodes in a dataset of 48 subjects (**Figure 4A**). We were able to achieve wide coverage with 4,142 surface electrodes mapping to 31 of 36 areas in the Desikan-Killiany parcellation (**Table 3**) (Desikan et al., 2006). We found functional interactions that agreed with previous studies of both functional and anatomical connectivity in macaque monkeys (**Figure 7**).

We measured electric potentials from the surface of the brain using subdural grid electrodes. The bipolar IFP measured mesoscopic signals (Buzsáki et al., 2012) that were resolute to within ~3 mm (Dubey and Ray, 2019). At this resolution, bipolar electrodes spanned the surface of the cortex containing multiple neurons organized over a few cortical columns (Mountcastle, 1997). This level of investigation thus considered ensembles of functional units as the fundamental node of the cortical interaction network.

We used a temporal resolution of 4 milliseconds (see **Methods**) which captured both asynchronous activity (Miller et al., 2009) and oscillations up to 125 Hz (Buzsaki, 2006). At this resolution it was possible to not only to investigate slow oscillations, but also fast dynamics in

the IFP signal that agreed with previously reported interactions in the gamma frequency band (Gregoriou et al., 2009).

Stringent precautions were taken to avoid contamination from electrical noise, movement artifacts, seizures, and volume conduction, leading to conservative estimates of the number and magnitude of interactions (**Methods**). A caveat of these restrictions, especially the bipolar referencing and 17 mm minimum spacing (**Figure 3**), is the exclusion of short-distance interactions.

It is important to note that all the work here reflects recordings in patients with epilepsy. Seizure related activity was not included in the analyses (**Methods**) and the overall methodology was independently compared against monkey neuroanatomy and neurophysiology (**Figure 9**). Despite these precautions and validation, it is conceivable that some (or none, or all) of the conclusions could be different in non-epilepsy subjects. With current techniques, it is not possible to perform this type of long-term continuous monitoring for a week of invasive neurophysiological data at high spatiotemporal resolution from healthy subjects.

Coherence values do not necessarily reflect *direct* interactions. Anatomical connectivity correlated well with interactions as measured by coherence (**Figure 7A-B**). However, significant coherence values do not imply direct anatomical connectivity (Petersen and Sporns, 2015). Conversely, anatomical connectivity does not imply physiological interactions either. The coherence values are not directional, and no claim is made here about the causality of the interactions (Reid et al., 2019). One exciting possibility to assess causality is to quantify the consequences of current injection via electrical stimulation followed by examination of the evoked cortico-cortical potentials (Fox et al., 2020; Trebaul et al., 2018). One of these direct stimulation

studies revealed a network that partially exhibited small-world characteristics (Keller et al., 2014), consistent with the results reported here.

Methods

Neurophysiological recordings

We studied 48 subjects with pharmacologically intractable epilepsy (20 female, 43 right-handed, 24 right hemisphere coverage, aged 3-47 years old, 19±11, here and throughout we report mean ± standard deviation, **Table 1**). The recordings were conducted as described previously (Liu et al., 2009). Briefly, subjects with pharmacologically resilient epilepsy were recruited based on their need for long-term invasive monitoring by surgically implanted electrodes. All procedures were performed with the subjects' informed consent. Recruitment for the study was conducted according to protocols approved by the Institutional Review Boards at Boston Children's Hospital, Harvard Medical School (35 of 48 subjects), and Brigham and Women's Hospital, Harvard Medical School (13 of 48 subjects).

Subjects were implanted with platinum electrodes (Ad-Tech, Racine, WI, USA; 2.3 mm diameter exposed area, with inter-electrode distances of either 5 mm (64 of 4,142 electrodes) or 10 mm (4,078 of 4,142 electrodes), impedance < 1kOhm). The location and number of electrodes varied across patients as determined by clinical needs. There were 26 to 176 electrodes implanted per subject (86±28, **Table 1**). Electrodes consisted of either grids or strips and were implanted in the subdural cavity. We refer to the electrical signals from these electrodes throughout the text as the *intracranial field potential* (IFP). IFP signals were continuously recorded for 0.9 to 10.4 days

(5.2±1.8 days, **Table 1**), with a sampling rate of 250 Hz, 256 Hz, 500 Hz, 512 Hz, 1000 Hz, 1024 Hz, 2000 Hz, or 2048 Hz using Natus NeuroWorks software (Oakville, Ontario, Canada).

Electrode localization

We collected T1-weighted magnetic resonance imaging (MRI) images of the head before electrode implantation for each subject. The pial surface of each subject was then reconstructed from image sets using the *freesurfer* package (Dale et al., 1999). We followed the *recon-all* pipeline using the fully-automated option ("-autorecon-all" flag). Post-operation computed tomography (CT) images of the implanted electrodes were localized to the MRI reconstruction using the *iELVis* package (Groppe et al., 2017). CT gantry tilt was corrected using the *dcm2niix* package from www.nitrc.org. Electrode grid and strip orientation was identified in the CT scan based on pre-surgical sketches and platinum marker guides (Ad-Tech, Racine, WI, USA). **Figure 1** shows the resulting electrode locations for all subjects. Electrode placement and coverage varied across individuals, and this variation can be appreciated from the reconstructed coordinates in **Figure 1**. All subjects except subject 26 had unilateral electrodes. All analyses were limited to within-hemisphere interactions only. The accompanying Supplementary Website provides three-dimensional renderings of the electrode locations for each subject (http://braininteractome.com).

Signal preprocessing

Several precautions were taken to remove potential artifacts from raw IFP recordings. Here we describe each of these preprocessing steps.

Definition of bipolar electrode referencing

We aimed to measure *local* signals to investigate mesoscopic interactions between brain regions. Volume conduction effects could potentially lead to inflated measures of interactions (Nunez et al., 1997). We erred on the side of caution and removed signals that may arise from volume conduction. We maximized the locality of the signal by re-referencing the IFP following a bipolar montage, which measured voltages with respect to adjacent electrodes. The bipolar montage has been shown to reduce the cortical spread of underlying neural signals (Dubey and Ray, 2016; Kajikawa and Schroeder, 2011). Additionally, bipolar referencing helps remove sources of global artifacts by subtracting signals coming from the ground reference. The bipolar IFP response measured local neural activity, with a reported spatial resolution of up to 3 millimeters (Bansal et al., 2014; Dubey and Ray, 2019; Vidal et al., 2010). Coherence measurements from bipolar-referenced IFP signals were less prone to false-positive reports of physiological interactions (Kajikawa and Schroeder, 2011). We refer to the resulting voltage signal, i.e., the difference between voltage in two physical electrodes, as the signal coming from a "bipolar electrode." Throughout the main text and figures, we used the term "electrodes" to refer to "bipolar electrodes" for simplicity.

Bipolar IFP signals were defined by subtracting a pair of raw IFPs from adjacent electrodes *within* a strip or grid. The definition of bipolar electrodes from physical electrodes followed the clinical convention. Let $V_i(t)$ represent the voltage measured at time t at the physical electrode i ($i = 1, \ldots, n$). Voltage at bipolar electrode j was defined as $V_j(t)=V_i(t) - V_{i+1}(t)$ for $j= 1, \ldots, n-1$. Grid electrodes were first split into individual strips before following the same procedure as defined for

strips. In total, the number of bipolar electrodes per subject equaled the number of physical electrodes minus the number of strips, after converting grids into strips (**Table 1**).

We assumed that neighboring electrodes before implantation remained neighbors post-implantation. We checked this assumption by measuring the distances between physical electrodes using their electrode localization coordinates. For the 46 out of 48 subjects with a pre-implantation interelectrode distance of 10 mm, the average distance measured between physical electrodes defined as a bipolar electrode pair was 10 ± 2 mm (n = 3,440, **Figure 3B**). The variance in the inter-electrode distance was mainly attributed to the flexibility of the electrode housing material and precision of electrode localization. The interactions between pairs of bipolar electrodes reported throughout this study encompass 4 physical electrodes (two bipolar electrodes); we refer to this arrangement as a bipolar electrode pair. The average number of physical electrodes per subject was 86 (range: 26 – 176). After applying the bipolar reference, the average number of bipolar electrodes per subject was 75 (range: 20 – 154).

When mapping electrodes to a parcellation of the brain (e.g., **Figure 11**), bipolar electrodes were localized based on the positions of the two physical electrodes. If both physical electrodes mapped onto the same area, the bipolar electrode was assigned to that area (2,101 out of 3,615 bipolar electrodes). Otherwise, the bipolar electrode was mapped based on the primary physical electrode.

Data filtering

The recording system removed DC biases. Interference from power line noise was removed by using a fifth-order Butterworth notch filter at 60 Hz, 120 Hz, and 180 Hz with a bandwidth of

3 Hz (Liu et al., 2009). In subjects where IFPs were recorded with a sampling rate of 250 Hz, the power line interference of the third harmonic at 180 Hz was apparent as the aliased frequency of 70 Hz. For subjects with sampling rates of 256 Hz, the apparent frequency of the third power line oscillation was 76 Hz. Notch filters with centers of 180 Hz were adjusted to their corresponding apparent center frequencies according to the sampling rates of the signals being filtered. Interference at 20 Hz from medical devices was detected in some of the IFP recordings (Dzwonczyk et al., 2009), and was also removed by applying the same notch filter with a center frequency of 20 Hz and a bandwidth of 4 Hz. To ensure that this filtering did not impact the coherence, frequency samples between (17, 23) Hz were excluded. The analyses in **Figure 7** refer to data recorded from macaque monkeys (Yanagawa et al., 2013) (see "Comparisons with macaque monkey neurophysiological recordings"). In those recordings, the power line noise frequency was 50 Hz, and the notch filter centers were adjusted accordingly.

Sampling rate

We used the lowest sampling rate available for analysis over the whole dataset: 250 Hz. All recordings were down-sampled to 250 Hz after the data filtering steps. In 10 of 48 subjects, sampling rates were integer multiples of 256 Hz. In these cases, the target for down-sampling was 256 Hz. The difference between subjects with 250 or 256 Hz sampling rates was accounted for throughout our analyses and did not impact any of the results. We found these sampling rates to be adequate in achieving a high temporal resolution (4 ms).

To simulate the effect of coarser temporal resolution, we repeated the analysis of the interaction network for subject 3 after applying a gaussian filter (*scipy.ndimage.gaussian_filter1d*,

sigma = 0.1 seconds (Jones et al., 2001)) to bipolar IFP recordings and found that only 58 (2%) out of 3,193 bipolar electrode pairs showed significant interactions. This number was much smaller than the original 557 (17%) pairs found to be significant, demonstrating that 0.1 seconds is too coarse to adequately assess interactions and emphasizing the necessity of recordings with high temporal resolution.

Artifact removal

The IFP recordings may contain artifacts of non-physiological origin, which may affect the analyses, especially when considering such long recording sessions as the ones used in this study. Some of those artifacts may persist even after bipolar referencing. Bipolar IFPs were separated into one-second segments to determine the presence of potential artifacts. We used a series of conservative criteria to define 6 types of potential artifacts (three of which are illustrated in **Figure 2**):

(i) *Large amplitude*. The strongest evoked IFP signals that other groups and we have characterized span several hundred μV (Liu et al., 2009; Tang et al., 2014). A one-second segment was considered to contain a potential artifact if the voltage range exceeded 2,000 μV: $\max\left(V\left(t\right)\right)-\min\left(V\left(t\right)\right)>2000\,\mu V$.

(ii) *Large slope*. A one-second segment was considered to contain a potential artifact if the magnitude of the slope of voltage versus time exceeded 100 μV/ms, $\left|\frac{dV(t)}{dt}\right| > 100\frac{\mu V}{ms}$, at any time during the segment. This slope was much larger than the range of neurophysiological slopes observed in previous IFP studies (Liu et al., 2009; Tang et al., 2014).

(iii) *Small amplitude.* A one-second segment with a voltage range of less than 10 μV was also marked as a potential artifact: $\max\left(V(t)\right) - \min\left(V(t)\right) < 10\mu V$

Examples of these types of artifacts are shown in **Figure 2**. As a conservative measure, any segment with a potential artifact was removed from further analyses. These three criteria led to the removal of 0.72%, 0.44%, and 0.1% of the data, respectively.

(iv) *Seizure events*. Clinical experts defined seizure onset and offset events. Recordings from all channels starting 15 minutes before seizure onset and ending 15 minutes after seizure offset were removed from analyses. An average of 0.68±1.81% of the data was marked as seizures.

(v) *Electrical stimulation events*. Subjects received external cortical stimulation as part of the procedure to functionally map areas relevant for surgery. All the cortical stimulation events were removed from the analyses. An average of 0.41 ± 0.17% of the data was marked as stimulation events.

(vi) *Electrodes with many artifacts*. Individual bipolar electrodes that had >50% of the data segments marked as potential artifacts were not considered for further analyses. This criterion removed a total of 0.34% of the 3,615 bipolar electrodes (**Table 3**).

In total, 2.1% of the data were marked as potential artifacts (out of 1.6×10^9 one-second segments). Individual fractions of artifacts marked for each criterion are listed in **Table 3**. Coherence values (see "Definition of interactions") were computed over 10-second windows. Thus, there were 20 one-second segments for each coherence window, considering the two bipolar electrodes. We only computed coherence measurements for a pair of bipolar electrodes when none of these 20 one-second windows contained potential artifacts.

Neighboring electrodes

We used bipolar referencing to improve spatial resolution and minimize artifacts (Dubey and Ray, 2016; Kajikawa and Schroeder, 2011). To further reduce potential false positives, we removed interactions between *neighboring bipolar electrodes* from analyses.

Same-grid neighbor electrodes. Two electrodes were neighboring if they were adjacent on strips and grids, or diagonally adjacent on grids (**Figure 3A**). A bipolar electrode pair was determined to be neighboring if any of the 4 possible physical electrode pairs were neighboring. After applying

this definition to the 148,404 bipolar electrode pairs across 48 subjects, 16,451 (11%) same-grid pairs were removed from analyses.

Different-grid neighbor electrodes. For bipolar electrodes residing on different strips or grids, neighbors were defined as follows. We considered the 16,451 same-grid neighbor electrodes. A histogram of the electrode distances for this set is shown in **Figure 3B**. This distance was used to determine an optimal threshold for neighborhood classification. A threshold of 17 millimeters was sufficient to achieve a true-positive rate of 92.1% and a false positive rate of 1.8%. After applying this threshold to bipolar electrode pairs from different grids, 7,088 (4.8%) additional bipolar electrode pairs were removed from analyses (shaded gray area under the solid line in **Figure 3B**).

The combined fraction of bipolar electrode pairs removed due to both same- and different-grid electrodes was 15.9%, leaving 124,865 pairs for subsequent analyses. This distance constraint impacted our study of physiological interactions by removing short-distance interactions while ensuring high sensitivity in reported coherence measurements (**Discussion**).

Comparisons with macaque monkey neurophysiological recordings

This study focused on human neurophysiological data. As an independent validation, we also analyzed similar IFP recordings obtained in a macaque monkey from the study of Yanagawa and colleagues (Yanagawa et al., 2013). These recordings consisted of resting intracranial field potentials from 128 electrodes similar to the ones used in humans, covering 42 of the 91 areas in the Markov-Kennedy atlas (Markov et al., 2012; Yanagawa et al., 2013).

Data preprocessing

The same steps described above for the human data were used on the monkey IFP recordings. To account for the 5 mm interelectrode distance of the monkey intracranial electrodes, the electrode neighborhood exclusion threshold was decreased from 17 mm to 8 mm. The periods including and between the administration of anesthesia (time = 40 minutes), and the administration of the anesthesia antagonist (time = 85 minutes) were removed from analyses. Method parameters were taken as originally documented (Yanagawa et al., 2013). Signal preprocessing excluded 12% of the recordings, while the anesthesia condition removed an additional 39% of the recordings. In total, we analyzed 450 minutes across 112 bipolar electrodes and 6,216 bipolar electrode pairs.

Electrode localization

Electrodes were localized by referencing locations provided by the study of Yanagawa and colleagues (Yanagawa et al., 2013) to the Markov-Kennedy areas (Markov et al., 2012).

Comparison between human and macaque brain locations

The M132 parcellation of the macaque monkey cortex (Markov et al., 2012) was applied to human subjects using the surface-based interspecies registration method (Van Essen and Dierker, 2007) from the software package *caret* (Van Essen et al., 2001). The interspecies algorithm transformed each of the 91 areas in the M132 macaque parcellation into areas represented on the coordinate space of the human Population Average Landmark and Surface-

based (PALS) atlas (Van Essen, 2005). These areas were then mapped from the human PALS atlas to the human fsaverage atlas (Dale et al., 1999) by *caret_command* from the *caret* package. For each human subject, the putative macaque area homologs were mapped onto the individual coordinate space by *mris_apply_reg* from the *freesurfer* package (Dale et al., 1999). The calculations for registering each subject to the average surface was conducted with default parameters set by *freesurfer* and using automatic reconstructions of surfaces as described in the electrode localization methods (see "Electrode localization"). **Figure 7C-E** shows a comparison between original M132 areas on the surface of the monkey brain (**Figure 7C**) and the putative interspecies homologs mapped on the surface of the brain of human subject 3 (**Figure 7D-E**).

Comparison between neuroanatomical connections and physiological interactions

We compared physiological interactions calculated from monkey IFPs to tractography connectivity information from the study of Markov and colleagues (Markov et al., 2012) (**Figure 7A-B**). We used the extrinsic fraction of labeled neurons (FLNe) metric to quantify anatomical connections. We collapsed the directed matrix by combining FLNe values in the forward and reverse directions, averaging the directed values to create the symmetric connectivity matrix. A missing value connection was defined as the absence of connectivity between pairs of areas where only one direction was tested. These missing values were omitted from the symmetric matrix averaging. Cortical distances were predictive of connectivity strength (Markov et al., 2012). Thus, we regressed out the Euclidean interelectrode distances when computing the partial correlation between the anatomical connectivity network (**Figure 7A**) and the coherence network (**Figure 7B**).

Comparison with known physiological interactions

Electrode locations from two studies of known physiological interactions (Bastos et al., 2015; Zhou et al., 2016) (**Figure 7F,H**) were taken from their respective sources directly. Electrodes were localized to areas defined by the Markov-Kennedy parcellation (Markov et al., 2012).

Definition of physiological interactions

We considered pairwise interactions between two bipolar electrodes in a segment of duration T=10 seconds. Although we used segments of T=10 second duration, the millisecond temporal resolution of IFP signals was essential for the analyses. Similar results were observed when using T=5 seconds or T=15 seconds to calculate coherence.

Let $V_a(t)$ and $V_b(t)$ represent the voltage in bipolar electrodes a and b at time t $(0 \le t \le T)$. The autocorrelation of each voltage signal and the associated auto-spectral density are defined as:

$R_{aa}(\tau) = \sum_t V_a(t) V_a(t+\tau)$ and $G_{aa}(f) = \frac{1}{2\pi} \sum_{\tau=-\infty}^{\infty} R_{aa}(\tau) e^{-if\tau}$ (similarly for bipolar electrode b).

We omit spelling out the duration T in the variables for simplicity. The cross-correlation between the voltage signals and the associated cross-spectral density are defined as: $R_{ab}(\tau) = \sum_t V_a(t) V_b(t+\tau)$ and $G_{ab}(f) = \frac{1}{2\pi} \sum_{\tau=-\infty}^{\infty} R_{ab}(\tau) e^{-if\tau}$. From these variables, we define the *coherence* between the two signals as (Nunez et al., 1997):

$$C_{ab}(f) = \frac{|G_{ab}(f)|}{\sqrt{G_{aa}(f)G_{bb}(f)}}$$

The real-valued coherence ranges from 0 (no relationship between the two signals) to 1 (for two identical signals).

Several studies have documented physiological interactions in narrow frequency bands (Bastos et al., 2015), such as the gamma band (Gregoriou et al., 2009; Madhavan et al., 2019). Coherence was separately integrated over five conventional frequency bands: **broadband (0.5≤*f*<125Hz)**, theta (3≤*f*<8Hz), alpha (8≤*f*<12Hz), beta (12≤*f*<17Hz) and (23≤*f*<27Hz), and gamma (30≤*f*<100Hz). To ensure that power line filtering did not have any effect on coherence calculations, a bandwidth of ±4 Hz (56 – 64 Hz), which was larger than the notch filter used in preprocessing of ±3 Hz, was used to exclude confounding frequency samples. This exclusion removed artifacts arising from imperfect notch filtering. When the frequency interval included 60 Hz or harmonics (50 Hz and harmonics for the monkey data), a window of ±4 Hz was removed from the analyses. Throughout the main text, we focus on the broadband coherence analyses. The gamma-band analyses are shown in the figures (**Figure 5, Figure 23, Figure 17A, Figure 17D, Figure 25, Figure 26**). Results for the other frequency bands are shown in the Supplementary Website.

The coherence was computed using Welch's method of overlapping segments. The input parameters were chosen to minimize the mean of the null distribution of the magnitude of coherence computed over permuted time-shifted IFP signals. The input parameters were 0.2-second segment width and 80% segment overlap. These parameters resulted in a spectral resolution of 5 Hz and were used for computing the broadband and gamma coherence. For the theta, alpha,

and beta coherence, a segment width of 2 seconds and 50% overlap was used to achieve 0.5 Hz spectral resolution. Given the large amounts of data processed in this study, computations were accelerated by writing a graphics processing unit (GPU) coherence function based on Welch's method (Welch, 1967) using the package *reikna* (Opanchuk, 2014). The 95-percentile of the difference in the magnitude of coherence between the GPU-accelerated implementation and *scipy.signal.coherence* (Jones et al., 2001) was 0.00073 (n = 15,336 randomly sampled time segments). There was a 16-fold decrease in processing time compared to *scipy.signal.coherence*, bringing down the analysis time from months to weeks per run.

The coherence value does not necessarily reflect *direct* interactions between the two areas. Anatomical connectivity correlates with physiological interactions (**Figure 7A,B**). However, a significant coherence value does not imply direct anatomical connectivity between the two areas (Steven and Sporns, 2015). Conversely, direct anatomical connectivity does not imply a physiological interaction either.

The coherence calculations reported here are not directional, and we do not make any statements about the causality of the pairwise interactions. The incidence of reciprocity in axonal tracts in animal models is variable, with near-complete reciprocity in mice (Gămănuţ et al., 2018), and lower reciprocity in macaque monkeys (Markov et al., 2012). Functional differences due to anatomical directionality have been reported in the macaque monkey visual cortex (Bastos et al., 2015; Nassi et al., 2013). However, the construction of directional anatomical connectivity

maps and the extent to which these asymmetries may impact function in the human cerebral cortex is the subject of ongoing investigation (Teillac et al., 2019; Van Essen et al., 2013).

Statistical analyses and null hypothesis

To assess whether random voltage fluctuations could explain the coherence values between two signals, we defined a null hypothesis whereby one of the signals was randomly shifted in time, thus preserving all its structure except for the synchronous interactions. A permutation test for each bipolar electrode pair was performed by randomly shifting IFP signals in time: $V_b(t)\ \ V_b(t+\tau)$. The time shift $_\tau$ was chosen uniformly without replacement between 2 minutes and the upper bound set by the length of the recording (**Table 1**). The time window used for time-shifted coherence was the same window used in the other analysis, that is, 10 seconds. This permutation procedure was run 10,000 times per bipolar electrode pair. The resulting null distribution was fitted to a t-distribution using the MATLAB *fitdist* function (The MathWorks, Inc., Natick, MA). A coherence threshold was determined for each bipolar electrode pair by taking the inverse cumulative distribution function of the fitted t-distribution, using the MATLAB *icdf* function. The p-value used for *icdf* was corrected for multiple hypotheses testing by controlling the family-wise error rate (FWER = 0.05). Coherence values above this threshold were marked as significant interactions (**Figure 4B-C**). Further constraints were imposed by the temporal consistency and between-subject consistency, described next. In the total of 124,865 bipolar electrode pairs, the resulting coherence thresholds had a median of 0.22 ± 0.18 (broadband), 0.42 ± 0.19 (theta band), 0.25 ± 0.30 (alpha band), 0.28 ± 0.26 (beta band), and 0.15 ± 0.16 (gamma band).

Chapter 2

Network properties of physiological interactions

Introduction

Network neuroscience (Bassett and Sporns, 2017) has been successful in demonstrating the ubiquity of graph metrics, including log-normally distributed weights (Buzsáki and Mizuseki, 2014; Markov et al., 2012), small-world (Humphries and Gurney, 2008; Telesford et al., 2011; Watts and Strogatz, 1998), and scale-free (Barabási and Albert, 1999) properties. Noninvasive imaging methods have allowed us to characterize both resting-state and task-activated networks after segmenting the brain into 180 areas (Glasser et al., 2016). Anatomical networks mapped by tract tracing in monkeys provide us with a sensitive and robust anatomical network (Markov et al., 2012) where a model based on an exponential distance rule was capable of predicting network motif distributions (Ercsey-Ravasz et al., 2013). In contrast, previous studies of mesoscopic physiological interactions using intracranial recordings have not reported network properties consistently. A study of physiological interactions during sleep showed that coherence networks were not small-world (Kramer et al., 2011), yet another study using electrical cortical stimulation did report small-world properties (Keller et al., 2014).

Besides the study of sleep networks previously discussed (Kramer et al., 2011), there has not yet been an investigation into how mesoscopic interactions in the human brain may be modulated by naturalistic behaviors over long lengths of durations. There has been recent interest in using computational methods to overcome the technical challenges associated with analyzing large amounts of data by training machine learning and neural network classification models to decode aspects of audiovisual recordings of behaviors from intracranial signals (Wang et al., 2018; Wang et al., 2016). Behavioral annotations in these studies were extracted using computer vision algorithms and was thus limited to low-level features such as pose positions, and to behaviors involving only direct action rather than passive perception. Here, we performed manual annotations of two active and two passive naturalistic behaviors in three subjects for up to 24 hours each (Iaselli et al., 2018), and show that a machine learning classification model was able to predict annotated labels from our measures of physiological interactions. We extended our classification model to decode annotations of sleep vs. wake in 14 subjects for an average of 4 days each.

Results

A mesoscopic network of interactions between human brain areas

Continuing from Chapter 1, we considered all possible electrode pairs. **Figure 11D** (right) depicts all significant interactions between the 91 electrodes for this example subject. Entry *i, j* in this symmetric coherence matrix denotes the interaction between electrode *i* and electrode *j*. For example, row 35, column 84 shows the example electrode pair in **Figure 4A,** the whole row 35 shows the interactions in **Figure 11B** for the Superior Temporal gyrus electrode**,** and the whole

column 84 shows the interactions in **Figure 11C** for the Pars Opercularis electrode. White entries denote neighboring electrode pairs excluded from analyses (**Figure 3**). Gray entries denote pairs that did not reach statistical significance (**Figure 6**). Of the 4,095 possible electrode pairs (91 choose 2), 3,193 pairs (78%) remained after applying the distance exclusion criterion (**Figure 3**), and 557 of these pairs (17%) showed significant interactions.

We mapped each of the 91 electrodes (**Figure 11D**, left) to its corresponding brain area in the 36-area Desikan-Killiany parcellation (Desikan et al., 2006). The symmetric coherence matrix in **Figure 11E** shows the average coherence for all pairs that map onto the corresponding brain areas (18 areas with coverage). For example, row 2, column 18 shows the average of all pairs between the Pars Opercularis and the Superior Temporal gyrus, including the one in **Figure 4A**. The hierarchical clustering of the coherence matrix (**Figure 11E**, right) reflects the similarity between brain areas based on coherence values, where shorter horizontal distances mean higher similarity (**Methods**). The hierarchical clustering of physiological interactions approximates the known anatomical relationships between different brain structures.

We extended the analyses to the full cohort of 48 subjects. Using the same procedure illustrated for Subject 3 in **Figure 4** and **Figure 11**. We present 48 maps showing all the interactions in each individual subject in the Supplementary Website (**Methods**). Of the 148,404 electrode pairs across all subjects, we analyzed 124,865 pairs (84%) after applying the distance exclusion criterion. We found a total of 11,692 significant pairwise interactions (9.4%). The average fraction of significant pairwise interactions across subjects was 10±15%.

The variation in the fraction of interactions across subjects arises from the heterogeneity in electrode locations dictated by clinical needs (**Figure 1**, **Methods**). To compare results between subjects, we considered two complementary approaches to map electrode locations across brains:

(i) mapping all electrode positions onto 36 Desikan-Killiany areas (**Table 2** (Desikan et al., 2006)) as illustrated for Subject 3 in **Figure 11E**, and (ii) mapping all the electrodes onto a custom parcellation based on spatial clustering of electrode locations (**Figure 13A-B, Methods**).

To illustrate the methodology, we follow the two areas in **Figure 4**, the Superior Temporal gyrus and the Pars Opercularis. Thirty out of 48 subjects had electrode coverage in both areas. We found at least one pair of interacting electrodes in these areas in 10 out of these 30 subjects (33%). All interacting pairs between these two areas are shown in **Figure 12**. Of the total of 448 electrode pairs spanning the two areas in these 10 subjects, 49 (11%) showed physiological interactions. The average coherence between the Superior Temporal gyrus and Pars Opercularis was 0.30±0.13. It should be noted that these parcellations reflect large brain areas and we expect heterogeneity in the electrode positions within each area across subjects. Despite the variance in electrode positions across subjects, we consistently found significant interactions between these two regions.

We applied the same analyses to the rest of the electrode pairs. The analyses were restricted to 31 of the 36 possible areas due to lack of coverage in 5 areas (**Table 2, Methods**), resulting in 465 area pairs (31 choose 2). There was adequate electrode coverage in 378 area pairs (**Figure 3**, **Methods**), of which 193 (51%) showed significant interactions. These interactions are summarized in the symmetric matrix in **Figure 14**. The standard deviation in coherence measures, the numbers of significant electrode pairs, and the number of subjects for each area pair is shown in **Figure 15**. For example, row 3, column 10 in this matrix reflects the interactions between electrodes in the Pars Opercularis and Superior Temporal gyrus, after averaging over all interacting electrode pairs in these two areas as shown in **Figure 12**.

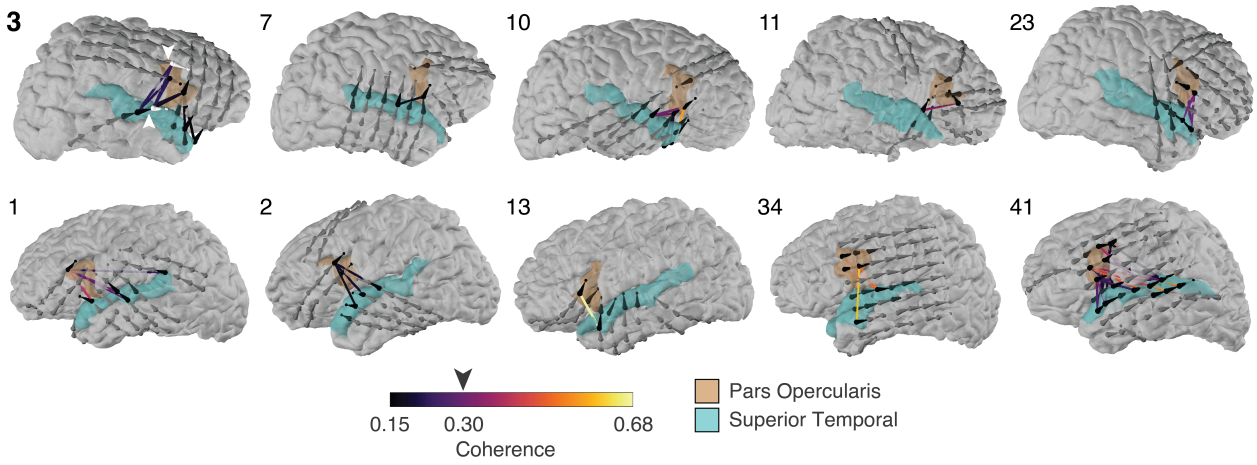

Figure 12. The interaction between Superior Temporal gyrus and Pars Opercularis was consistent across subjects.

Ten subjects (subject numbers shown next to each brain) where there was at least one significant pair of electrodes showing significant interactions between electrodes mapping onto the Superior Temporal gyrus (cyan) and Pars Opercularis (beige). Bipolar electrode pairs are indicated by the droplet-shaped markers where the head indicates the primary electrode and the tail points to the ground electrode. The black markers denote bipolar electrodes participating in significant interactions. The color of the line joining any two dots indicates the degree of coherence (color scale on bottom). The arrow on the color bar shows the average degree of coherence across all these electrode pairs. The white arrows denote the electrodes shown in **Figure 4A** for Subject 3.

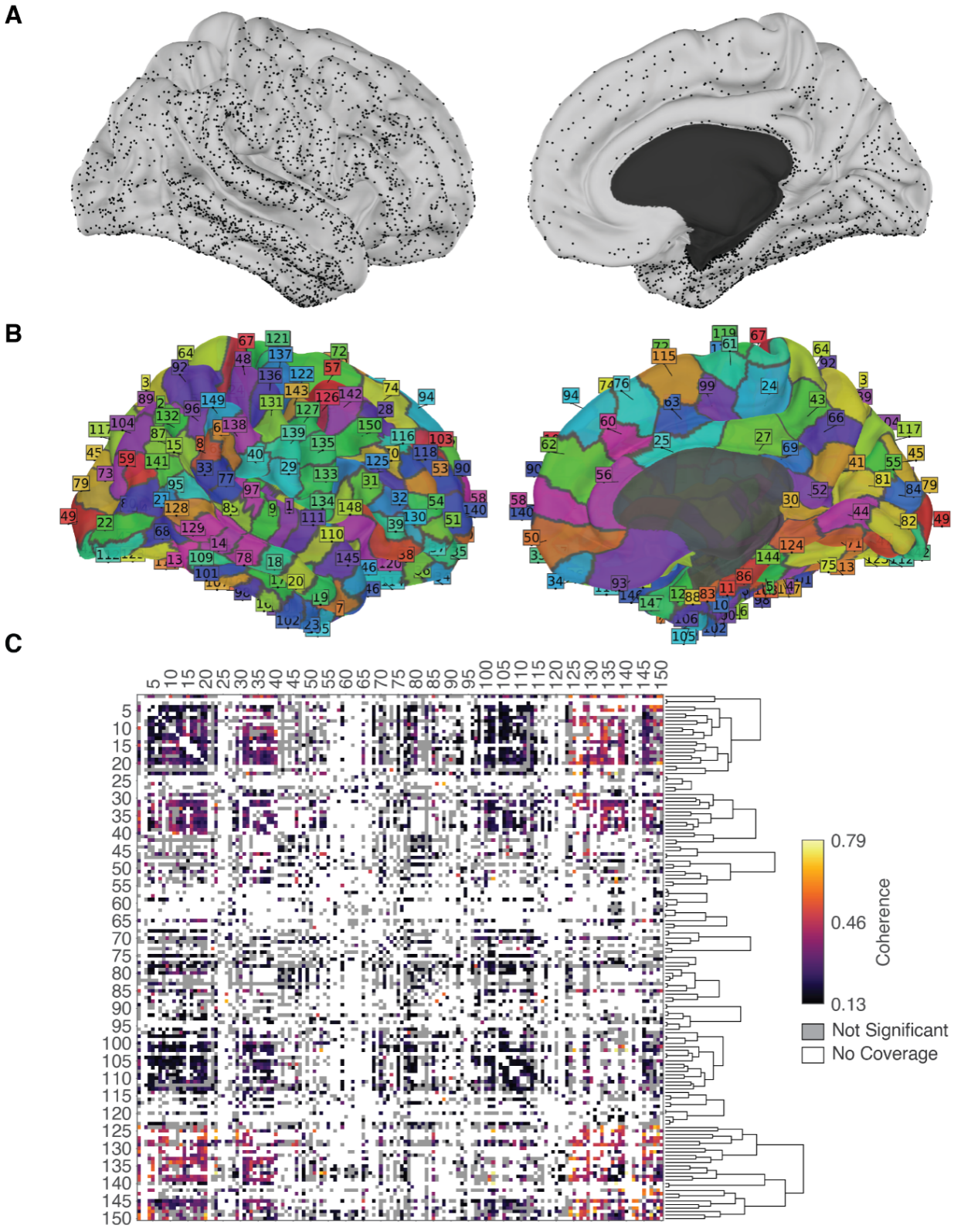

Figure 13. Parcellation of the human brain into 150 areas based on electrode coverage.

(**A**) All 3,615 electrode locations shown as black dots on average pial surface of the right hemisphere. The lateral (left) and medial (right) views are shown. (**B**) Each of the 150 areas obtained by clustering electrode distances is represented as a colored patch on the surface, separated by areal boundaries in dark gray (**Methods**). (**C**) Interactions between areas in the 150-area parcellation. Interactions shown were significant in at least 2 subjects and at least 10 electrode pairs. The fraction of pairs of brain areas that did not have adequate coverage was 58% (6,531 of 11,175). Of the pairs of brain areas that had adequate coverage, 51% (2,387 of 4,644) showed statistically significant interactions. Region numbers correspond to those shown in **B**. The example electrodes from Subject 3 in **Figure 4A** were localized to areas 111 and 148, which showed significant overlap with Desikan-Killiany areas Superior Temporal gyrus and Pars Opercularis, respectively.

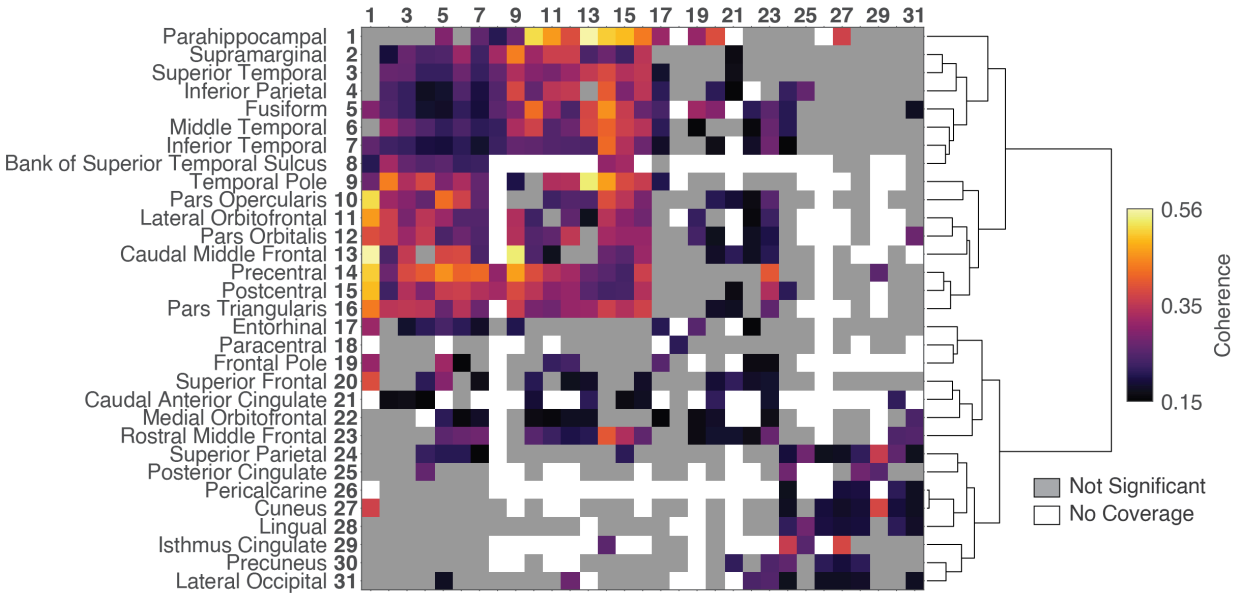

Figure 14. Mesoscopic interactome of the human brain.

This symmetric matrix shows all significant subject-averaged coherence values between areas in the Desikan-Killiany parcellation**.** Pairwise interactions between anatomical areas defined in the Desikan-Killiany parcellation (Desikan et al., 2006). There was electrode coverage in 31 of the 36 defined areas (**Methods**). Of the 31-choose-2 = 961 pairs of areas, 180 (19%) did not have electrode coverage in our data (white squares). Of the 781 covered pairs of areas, 345 (44%) interactions were statistically significant, and the color shows the average coherence (see color scale on right). Interactions shown are significant in at least 2 subjects, and across at least 10 bipolar electrode pairs. Gray squares denote interactions that were not significant. The interaction between the Superior Temporal gyrus and Pars Opercularis (**Figure 4** and **3A**) showed an average coherence of 0.30±0.02 and can be seen at row 3, column 10. The hierarchical clustering dendrogram on the right shows the relationship between Desikan-Killiany areas based on their similarities in coherence with other areas (**Methods**).

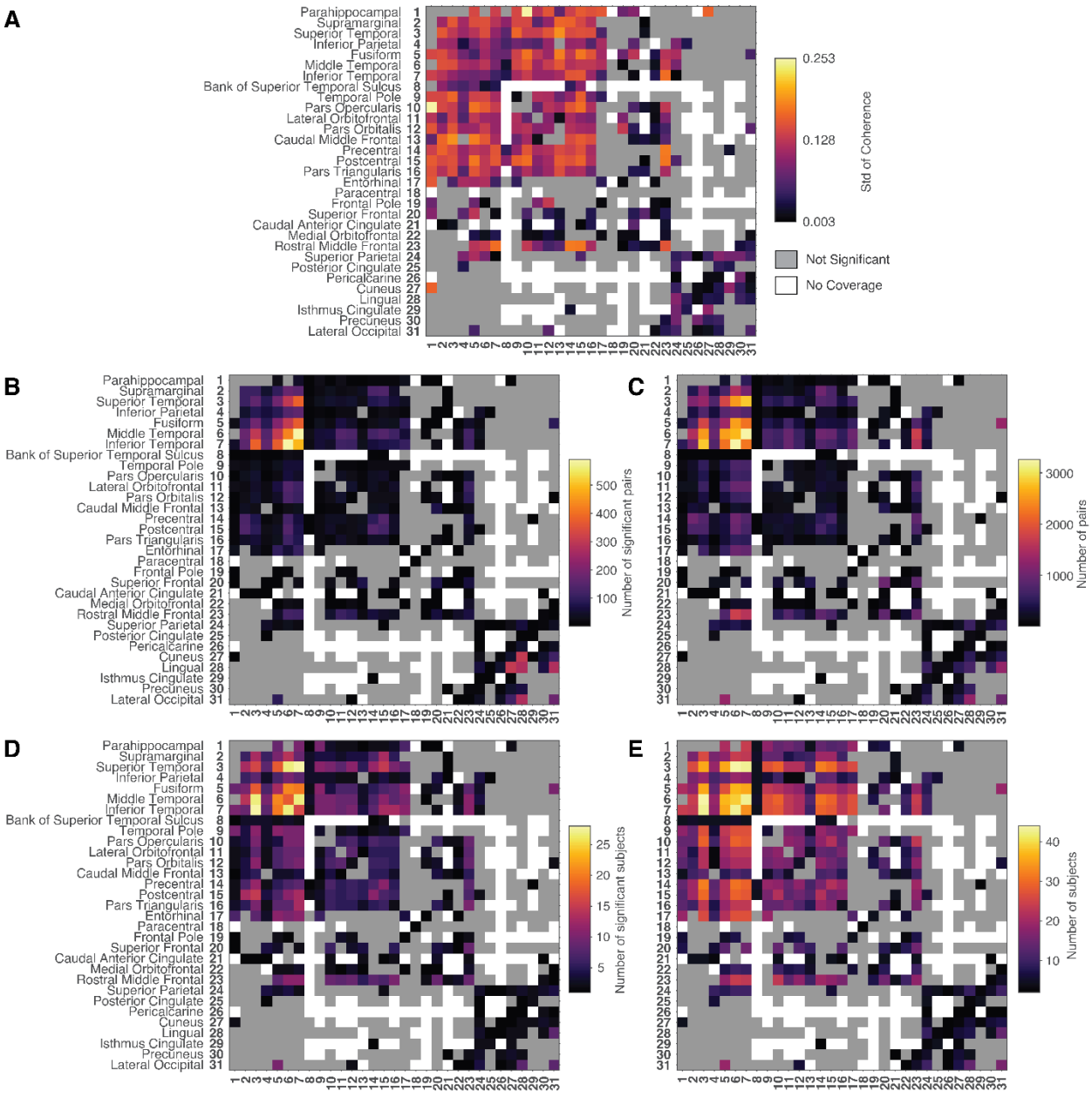

Figure 15. Coherence standard deviation across bipolar electrode pairs and across subjects.

(**A**) Following the format from **Figure 14**, standard deviation of coherence calculations. (**B**) Number of significant bipolar pairs used for calculating the coherence averages shown in **Figure 14**. (**C**) Total number of bipolar pairs used for any given pair of regions. (**D**) Number of subjects spanned by significant bipolar pairs. (**E**) Total number of subjects for any given pair of regions.

Of those area pairs that showed significant interactions, the weakest interaction was between the Inferior Temporal gyrus and Superior Parietal gyrus (#7 and #24 in **Figure 14**, 0.145±0.003 coherence), and the strongest interaction was between the Parahippocampal gyrus and Caudal Middle Frontal gyrus (#1 and #13, 0.563±0.072 coherence).

The distribution of interaction strengths followed a log-normal distribution (**Figure 16A**, p=0.59, Kolmogorov-Smirnov test) rather than a normal distribution (p=0.04, Kolmogorov-Smirnov test). The Supplementary Website (**Appendix**) renders all the interactions in a 3D brain that can be rotated to scrutinize the location and coherence of each electrode pair. The Paracentral gyrus had the least number of interactions (#18 in **Figure 14**): only electrode pairs where both coordinates mapped within the Paracentral gyrus showed significant interactions. The Fusiform gyrus showed the most interactions (#5 in **Figure 14**): 23 of 29 (79%) areas with electrode coverage interacted with the Fusiform gyrus.

The areas in the interaction matrix shown in **Figure 14** reflected a common parcellation of the human brain based on anatomical landmarks (Desikan et al., 2006). We also implemented a custom parcellation dictated by electrode coverage. We mapped electrodes from each of the 48 subjects onto a common average surface (**Figure 13**) and used K-means clustering to form 150 non-overlapping areas (**Figure 13B**, **Methods**). The pair of electrodes in **Figure 4** mapped onto areas 111 and 148 in this custom parcellation (**Figure 17B**). Area 111 was one of 10 areas in the custom parcellation that overlapped with the Superior Temporal gyrus. Area 148 was one of 3 areas that overlapped with the Pars Opercularis. We described the interaction in **Figure 12** in terms of the custom parcellation (**Figure 17C-D**): within the 10 x 3 = 30 possible area pairs between these two sets of custom parcellation areas, 25 had electrode coverage. Of these 25 custom area

pairs, 18 (72%) showed significant interactions, with an average coherence value of 0.30±0.10 that was comparable to the one reported for Desikan-Killiany areas in **Figure 12** (0.30±0.13).

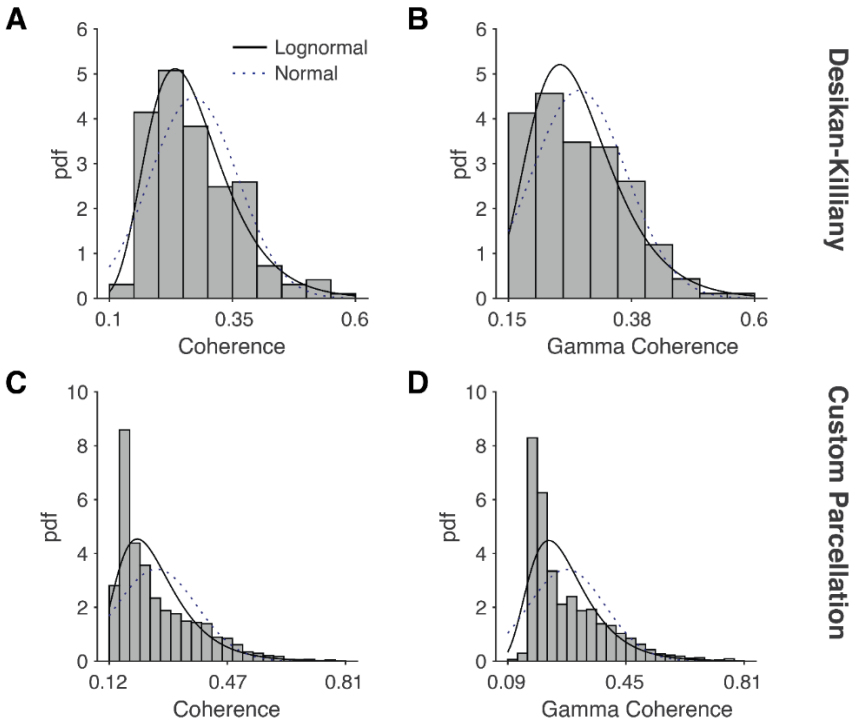

Figure 16. Log-normal distributions of physiological interaction coherence values.

(**A**) Histogram of the 193 significant broadband coherence values from **Figure 14**. The log-normal fit is indicated by the solid line, the normal fit is indicated by the blue dotted line. (**B**) Histogram and log-normal fit for the 184 significant gamma band coherence values from **Figure 26**. (**C**) Histogram of the 2,387 significant broadband coherence values between areas defined by the custom 150-area parcellation from **Figure 13C**. (**D**) Histogram of the 2,110 significant gamma band coherence values from **Figure 17A**.

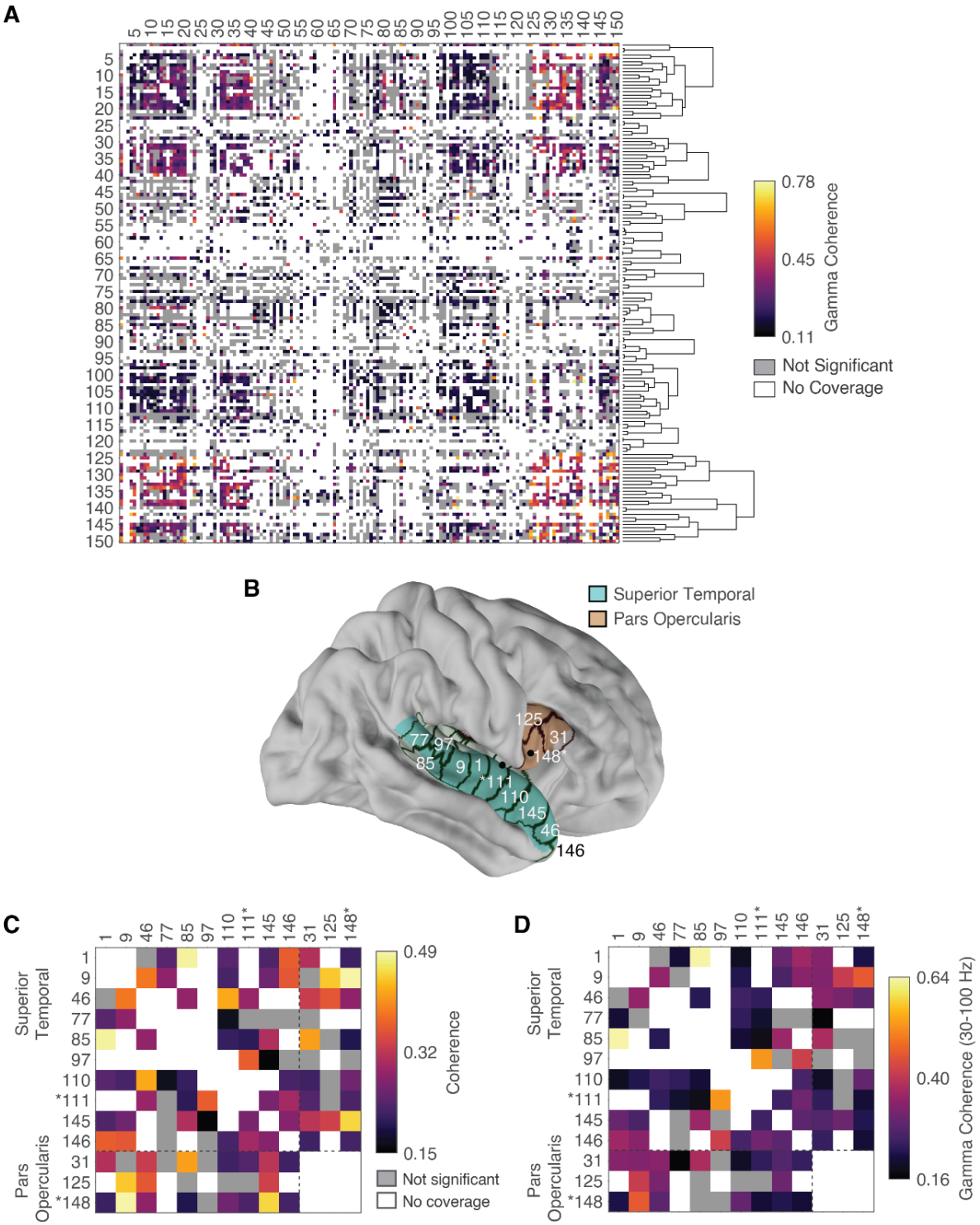

Figure 17. Gamma band coherence in the 150-area parcellation.

(**A**) Following the format from **Figure 13C**, here we report the gamma band coherence [30,100) Hz. Of the covered pairs of brain areas, 45% (2,110 of 4,644) showed statistically significant interactions. (**B**) The electrodes illustrated in **Figure 4A** are shown on the average pial surface of the right hemisphere, with the Superior Temporal and Pars Opercularis highlighted in cyan and

beige, respectively. These electrodes mapped onto areas 111 and 148 according to the 150-area parcellation, which are indicated by the asterisks in **C-D**. Areas with significant overlap with Pars Opercularis (31,125,148) are shown as dark red outlines. Similarly, areas overlapping with the Superior Temporal gyrus are shown as dark green outlines. (**C**) A subset of the physiological interactions shown in **Figure 13C** is reproduced, except only the regions that had significant overlap with Desikan-Killiany areas in **B** are shown. (**D**) Following the format in **C**, we report gamma band coherence.

We described the interactions from the whole set of 11,175 custom area pairs (150 choose 2). Of the 4,644 custom area pairs with electrode coverage, 2,387 (51%) showed significant interactions (**Figure 13C**). Interaction strengths ranged from 0.13 (between areas 121 and 143, both overlapping with the Precentral regions in the Desikan-Killiany map) to 0.79 (between areas 137 and 140, overlapping with the Precentral and Rostral Middle Frontal regions in the Desikan-Killiany map). As described for the anatomical map, the distribution of interaction strengths followed a log-normal distribution fit (**Figure 16C**). The area that showed the most interactions with other areas was area 19, which overlaps with the Middle Temporal gyrus in the Desikan-Killiany map. Area 19 interacted with 82 of the 111 regions with coverage.

Our dataset contained subjects from 3 to 47 years old (**Table 1**). We evaluated whether there was a difference in the brain interactome between young and older subjects by splitting the data using the median age of 17 into two subgroups of ages 11.2 ± 3.9 and 26.9 ± 10.2. We re-calculated physiological interaction networks in each subgroup (**Figure 18**). Of the original 193 significant brain area pairs, there were 140 (73%) brain area pairs that were found to be significant in both age subgroup datasets. We found a significant difference in coherence values between the two groups ($p = 2 \cdot 10\text{-}17$, two-sided ranksum test). Similarly, for the gamma-band coherence, of the original 184 significant brain area pairs, 125 (68 %) were found to be significant in both age

subgroups. There was also a difference in gamma band coherence values between the two groups ($p = 2 \cdot 10\text{-}19$, two-sided ranksum test).

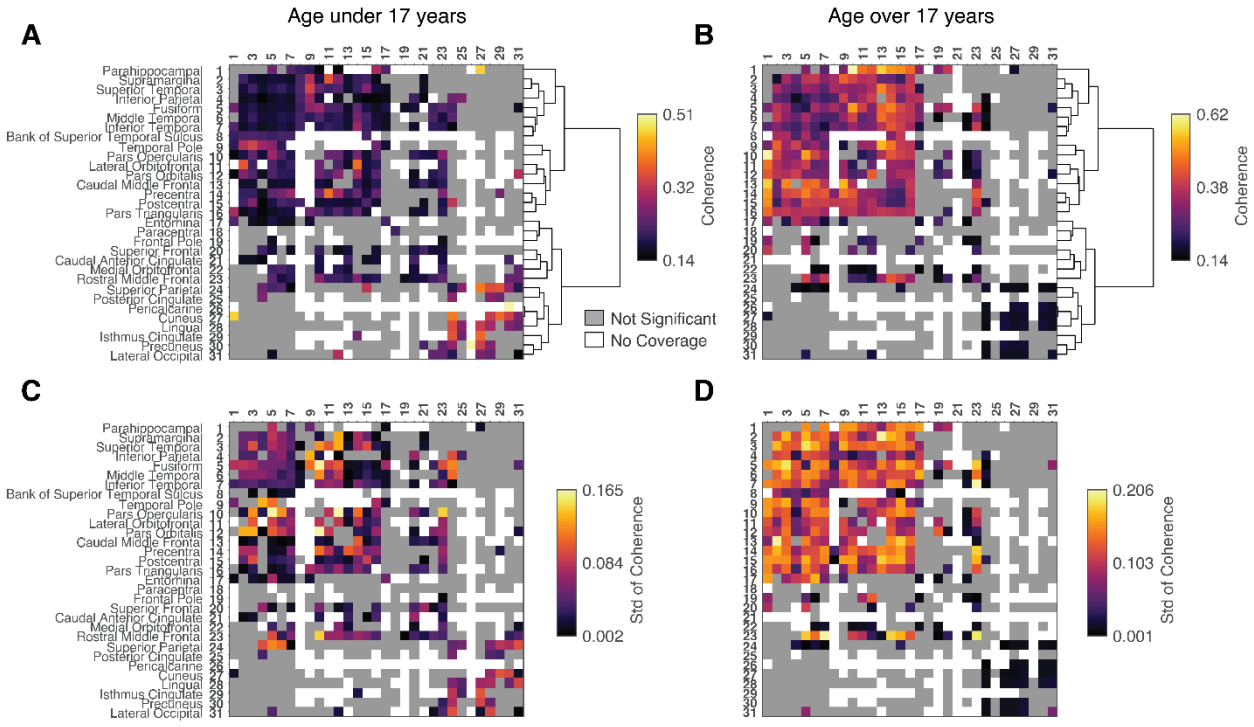

Figure 18. The effects of age on coherence between Desikan areas.

All subjects were split into two equal-sized groups: below 17 years old (A) and above 17 years old (B). Following the format from Figure 4, this figure shows interactions between all brain areas for these two groups. The standard deviations of coherence values are shown in (C) and (D) for the corresponding age groups.

Interactions reflect small-world network properties that enable rapid and flexible communication

The interaction matrix (**Figure 14**) can be thought of as a network graph composed of nodes (brain areas), connected by weighted edges (coherence values). As noted above, the number of edges per node (i.e., the number of other areas that any brain region interacted with) was not

uniformly distributed. Therefore, we sought to describe the network structure of the interaction matrix by asking whether or not it exhibited small-world properties (Watts and Strogatz, 1998). In a small-world network, connections between nodes are neither distributed uniformly nor randomly; instead, the connectivity includes "neighborhoods" with high local connectivity and sparser interconnectivity between neighborhoods, enabling traversing from one node to any other node in a small number of steps. Using the reciprocal of the coherence as a proxy for the length between two nodes, we measured the mean shortest path length (L) and the clustering coefficient (C) of the interaction matrices (Bassett and Bullmore, 2017) (**Methods**). Small-world networks are characterized by short path lengths and high clustering coefficients. We calculated these metrics in both the human (**Figure 19**) and monkey (**Figure 20**) brains.

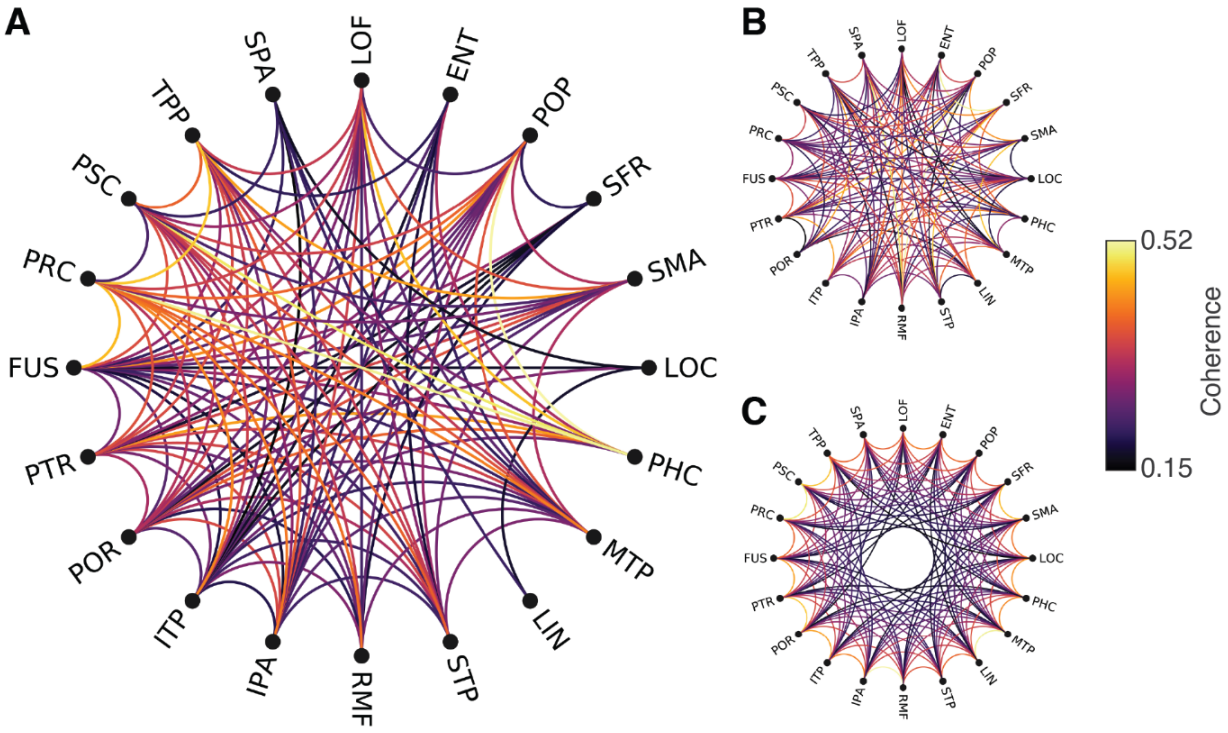

Figure 19. The mesoscopic interactome showed small-world network properties.

(**A**) Graph of neural interactions based on twenty nodes corresponding to areas in the Desikan-Killiany parcellation after removing areas with missing values (see **Table 2** for abbreviations). The color indicates the coherence value (see scale on right). (**B**) Random graph of neural interactions obtained by re-assigning coherence weights from the network in **A**. (**C**) Lattice graph of neural interactions. The networks in **B** and **C** have the same number of nodes and edges as the actual network in **A**. The small-world coefficient (Humphries and Gurney, 2008) was σ=1.2 (95% CI: 1.1, 1.3), satisfying the range σ>1. The small-world measurement (Telesford et al., 2011) was ω=-0.41 (95% CI: -0.42, -0.39), satisfying the range -0.5<ω<0.5 (**Methods**).

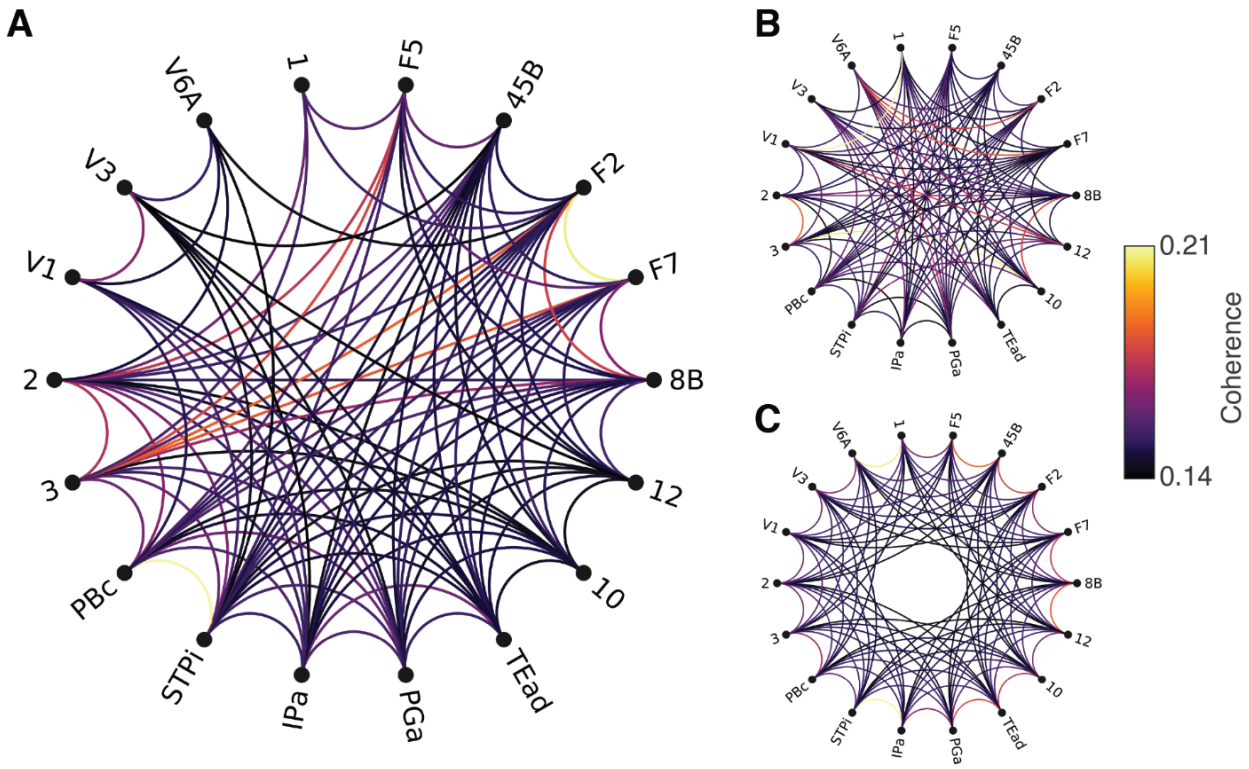

Figure 20. The macaque monkey physiological interactivity small-world network.

Following the format from **Figure 19**, here we show the physiological interaction network from recordings in macaque monkeys (**A**), the restructured random network (**B**), and the lattice network (**C**). The small-world coefficient (Humphries and Gurney, 2008) was σ=1.15 (95% CI: 1.09, 1.20), satisfying the small-world range σ>1. The small-world measurement (Telesford et al., 2011) was ω=-0.188 (95% CI: -0.195, -0.182), satisfying the small-world range -0.5<ω<0.5.

We compared the *L* and *C* values against two null models: random graphs (*rand*, **Figure 19B**), and lattice graphs (*latt*, **Figure 19C**). Both null models have the same number of nodes and edges as the original network but they show different topology. We computed the small-world

coefficient, σ, defined as the ratio between the clustering coefficient and the mean shortest path length, both normalized by the corresponding values for the random graph ($\sigma = C/C_{rand} / L/L_{rand}$) (Humphries and Gurney, 2008). For the human brain, we obtained σ=1.20 (95% confidence interval (CI): 1.14,1.26); for the macaque brain, we obtained σ=1.15 (95% CI: 1.09,1.20). Both species revealed small-world networks, which are characterized by σ>1. Another commonly-used small-world metric, ω, is defined as $L_{rand}/L - C/C_{latt}$ (Telesford et al., 2011), and takes values between -0.5 and +0.5 for small-world networks. For the human brain, we obtained ω = -0.406 (95% CI: -0.417, -0.394); for the macaque brain we obtained ω = -0.188 (95% CI: -0.195, -0.182). A summary of all computed small-world measures is shown in **Table 4**. Both the human and monkey interaction networks deviated from random and lattice graphs and were consistent with small-world network properties found in other neural systems (Bassett and Bullmore, 2017). Furthermore, we evaluated small-world properties in 13 individual subjects who had sufficient coverage: all 13 subjects showed small-world properties based on σ and 11 of 13 subjects showed small-world properties based on ω (**Table 5**). In sum, efficient communication via small-world networks was evident at the individual subject level as well as in the whole interactome, in humans and monkeys, and in broadband and gamma-band signals.

	Broadband		Gamma Band	
	Monkeys	Humans	Monkeys	Humans
L	8.82	5.23	8.08	5.34
C	0.57	0.49	0.73	0.53
L_{random}	8.50 (0.03)	4.36 (0.03)	7.87 (0.02)	4.37 (0.03)
$L_{lattice}$	8.85 (0.01)	4.93 (0.004)	8.09 (0.004)	4.92 (0.004)
C_{random}	0.48 (0.01)	0.34 (0.01)	0.58 (0.01)	0.34 (0.01)
$C_{lattice}$	0.49 ($6 \cdot 10^{-5}$)	0.40 ($6 \cdot 10^{-5}$)	0.59 ($4 \cdot 10^{-5}$)	0.42 ($2 \cdot 10^{-5}$)
σ	1.1 (0.03)	1.2 (0.03)	1.2 (0.03)	1.3 ($5 \cdot 10^{-2}$)
ω	–0.19 (0.003)	–0.41 (0.01)	–0.26 (0.002)	–0.44 (0.006)

Table 4. Small-world network measures.

The characteristic pathlength (L) and clustering coefficient (C) are shown for human and macaque monkey physiological networks based on the broadband and gamma band coherence (see **Methods**). Values shown represent means from multiple random initializations of random and lattice networks. Values shown in parentheses represent standard deviations. The small-world coefficient σ (Humphries and Gurney, 2008) and small-world measurement ω (Telesford et al., 2011) both indicated the presence of small-world networks across species and frequency bands.

Subject	L	C	L_{random}	$L_{lattice}$	C_{random}	$C_{lattice}$	σ	ω
1	2.60	0.99	2.60 (0.00)	2.83 (0.05)	0.83 (0.00)	0.73 (0.01)	1.20 (0.00)	-0.34 (0.02)
2	6.71	1.11	6.62 (0.05)	5.34 (0.03)	0.76 (0.01)	0.88 (0.00)	1.44 (0.01)	-0.28 (0.01)
5	5.55	0.83	5.37 (0.10)	4.60 (0.00)	0.58 (0.07)	0.73 (0.00)	1.39 (0.17)	-0.18 (0.02)
7	7.31	1.29	7.30 (0.02)	6.22 (0.02)	0.80 (0.00)	0.97 (0.00)	1.60 (0.01)	-0.32 (0.01)
10	4.36	0.88	4.39 (0.05)	3.61 (0.00)	0.70 (0.08)	0.80 (0.00)	1.30 (0.16)	-0.10 (0.01)
13	3.28	0.81	3.25 (0.04)	3.24 (0.01)	0.61 (0.08)	0.53 (0.00)	1.35 (0.19)	-0.55 (0.01)
15	6.23	0.82	6.20 (0.10)	5.31 (0.01)	0.56 (0.08)	0.72 (0.00)	1.51 (0.23)	-0.14 (0.02)
16	7.08	0.93	8.39 (0.02)	6.97 (0.00)	0.69 (0.05)	0.88 (0.00)	1.61 (0.11)	0.13 (0.00)
25	4.15	0.83	4.66 (0.08)	4.57 (0.01)	0.46 (0.06)	0.51 (0.00)	2.06 (0.27)	-0.49 (0.02)
34	2.03	1.00	2.03 (0.00)	2.08 (0.01)	0.87 (0.00)	0.84 (0.00)	1.15 (0.00)	-0.19 (0.00)
40	9.78	0.71	8.73 (0.11)	8.47 (0.01)	0.39 (0.04)	0.48 (0.00)	1.64 (0.18)	-0.59 (0.01)
41	3.11	0.74	3.10 (0.01)	3.13 (0.01)	0.73 (0.01)	0.60 (0.00)	1.01 (0.01)	-0.23 (0.00)
48	7.19	1.30	7.19 (0.00)	7.16 (0.00)	0.99 (0.00)	0.99 (0.00)	1.31 (0.00)	-0.31 (0.00)

Table 5. Small-world network measures in individual subjects.

Small-world coefficients for 13 subjects with sufficient data following the format in **Table 4**. The coefficient σ (Humphries and Gurney, 2008) indicated the presence of a small-world network in all 13 subjects. The measurement ω (Telesford et al., 2011) indicated the presence of a small-world network in 11 of 13 subjects.

Decoding behaviors from coherence metric

Our measures of coherence and small-world properties showed correlations with periods of sleep and with other task-free, naturalistic behaviors (**Figure 21**). We annotated whether subjects were sleep or wake in 14 subjects and whether subjects were performing one of four naturalistic behaviors in 3 subjects over our measures of physiological interactions and their networks (**Methods**). Our annotations were comparable to that of two clinical experts (inter-rater reliability coefficient = 0.66, Cohen's Kappa) (**Figure 22**). We found that our interaction measures were suitable for decoding sleep using a nearest neighbor classification model, with a cross-validated accuracy of 0.69±0.11 (**Figure 21A**). When classifiers were trained only on small-world metrics, the cross-validated accuracy was 0.59±0.06, and when trained only on coherence features, the cross-validated accuracy was 0.66±0.11. We did not find a significant difference between accuracy scores between models trained on these two types of features ($p = 0.19$, two-sided ranksum test). For naturalistic behaviors, we fitted our models separately to classify physical contact vs. no physical contact (with an accuracy of 0.66±0.16), head movement (0.65±0.03 accuracy), body movement (0.65±0.08), and watching TV (0.69±0.10) (**Figure 21B**). These results demonstrate that physiological interactions showed statistical correspondence with a range of behaviors including wake and sleep states, and vice versa.

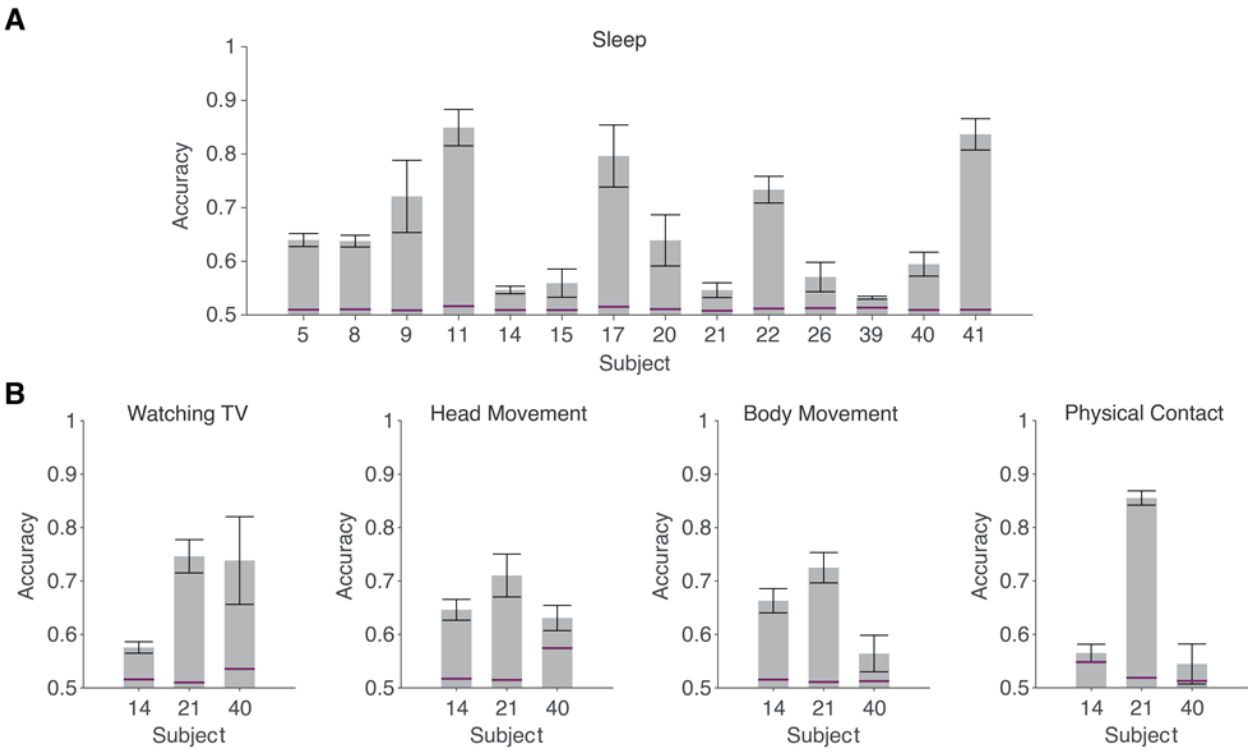

Figure 21. Brain interactions correlate with sleep and natural behaviors.

(A) Cross-validated accuracy of a nearest neighbor classifier trained to decode whether the subject was awake or asleep using coherence values from pairwise interactions in each one of 14 subjects (Methods). Error bars denote standard deviation. Purple lines indicate the permutation significance threshold. Accuracies were significantly above chance (chance = 0.5), in all 14 subjects ($p<0.0025$, permutation test, corrected for multiple comparisons). (B) Cross-validated accuracy of a nearest neighbor classifier trained to decode four possible natural behaviors (Methods). Error bars denote standard deviation. Purple lines indicate the permutation significance threshold. Accuracies were significantly above chance (chance=0.5), in all cases except for the last bar ($p<0.0025$, permutation test, corrected for multiple comparisons).

A

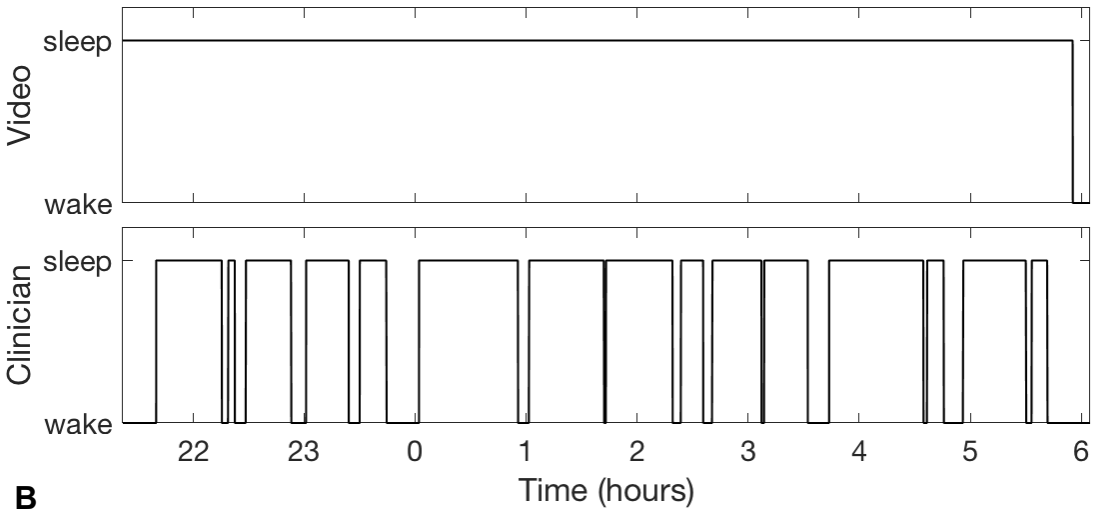

B

Subject	Segment	Length (Hours)	Accuracy	True Positive	True Negative	Cohen's Kappa
1*	Night 1	8.7	0.89	1.0	0.14	0.22
1	Night 2	7.7	0.88	0.96	0	-0.05
1	Night 4	8.4	0.84	0.87	0.74	0.59
2	Night 1	8.5	0.95	0	1.0	0
5	Day 4	2.5	0.97	1.0	0.86	0.91
5	Night 4	1.5	0.67	0.67	0	0
9	Night 2	10	0.95	0.95	1.0	0.17
All		47.3	0.9	0.96	0.64	0.66

Figure 22. Agreement of sleep annotations with clinicians.

A subset of our data was also annotated by certified sleep clinicians. (**A**) An example night of annotations. The top panel shows our annotations, and the bottom panel shows the clinicians' annotations for the same segment. **(B)** Agreement between the two sets of annotations. The segment shown in (A) is marked with an asterisk (*).

Neural interactions in the gamma frequency band

The results presented in the main text are based on coherence calculations based on broadband neural signals between f_1=0.5 Hz and f_2 = 125 Hz. Many studies have documented

interactions between brain areas in narrower frequency bands, particularly in higher frequencies (Bastos et al., 2015; Buzsaki, 2006; Gregoriou et al., 2009; Madhavan et al., 2019). We re-calculated the coherence in four frequency bands: 3-8 Hz (theta), 8-12 Hz (alpha), 12-17 Hz and 23-27 Hz (beta), and 30-100 Hz (gamma). Here we focus on the gamma frequency band; results for the other three frequency bands are shown in the Supplementary Website.

The electrode pair depicted in **Figure 4** also showed prominent interactions in the gamma band, with a coherence of 0.39 for the same 10-second segment in **Figure 4A** (**Figure 5A**), an average coherence of 0.21 ± 0.06 over 5.5 days, and a temporal consistency of 47% (**Figure 25A**). As reported for the broadband interactions (**Figure 11**), gamma-band interactions showed spatial specificity (**Figure 25B-C**). The gamma-band interactions between the Superior Temporal gyrus and Pars Opercularis described in subject 3 were observed in 11 of the 30 (37%) subjects with coverage in both areas (**Figure 23**). Subject 24 showed interactions in the gamma frequency band that were not present in the broadband analysis (compare **Figure 23** versus **Figure 12**). In all the other subjects, interactions were evident in both broadband and gamma-band signals. Of the total of 448 electrode pairs between these areas in these 11 subjects, 51 (11%) showed interactions. The average gamma-band interaction strength for these two brain areas was 0.28±0.13 (mean±SD).

We found a total of 280 significant interactions in the gamma band out of 3,193 (8.8%) electrode pairs in subject 3 (**Figure 25D**). The gamma-band coherence between all Desikan-Killiany areas is shown in **Figure 26**. The standard deviation in coherence measures, the numbers of significant electrode pairs, and the number of subjects for each area pair is summarized in **Figure 27**. A total of 184 out of 378 (49%) area pairs showed significant gamma-band interactions. As reported for the broadband signals, the significant gamma-band interaction weights followed a log-normal distribution (p=0.12, Kolmogorov-Smirnov test) (**Figure 16B**).

The gamma-band interaction strengths ranged from 0.16 (between Superior Parietal gyrus and Pericalcarine gyrus) to 0.57 (between regions Caudal Middle Frontal gyrus and Parahippocampal gyrus). The area that showed the highest fraction of gamma-band interactions with other areas was the Precentral gyrus, which showed interactions with 22 of 30 (73%) areas with electrode coverage.

We also analyzed the gamma band interactions using our custom 150-area parcellation (**Figure 17A**). A total of 2,110 out of 4,644 area pairs with adequate coverage (45%) showed significant gamma-band interactions. The gamma-band interaction strengths ranged from 0.11 (between areas 10 and 51) to 0.78 (between areas 4 and 149). The area with the highest fraction of gamma-band interactions with other areas was area 19, which overlaps the Middle Temporal gyrus in the Desikan-Killiany parcellation, which interacted with 74 of 111 (66%) areas. The distribution of interaction strengths as measured by the gamma coherence and the log-normal distribution fit is shown in **Figure 16D**.

The small-world network properties observed in the broadband physiological interactivity network were also apparent when using the gamma band interaction networks, both in humans: $\sigma = 1.28$ (95% confidence interval (CI): 1.19, 1.37), and $\omega = -0.439$ (95% CI: -0.449, -0.426); and in macaques: σ=1.22 (95% CI: 1.16,1.27) and $\omega = -0.264$ (95% CI: -0.267, -0.260). A summary of these metrics for the gamma interaction network is shown in **Table 4**.

Discussion

Cognition emerges through rapid communication between brain areas. Here we provide an extensive, population-based, and dynamic description of the mesoscopic interactome in the human

cortex over a continuous period of up to 10.4 days. Interactions were defined by coherence measurements between intracranial field potentials (IFPs) recorded from pairs of bipolar-referenced electrodes (**Figure 4**) in 48 subjects (**Figure 1**, **Table 1**). We achieved ample coverage with 4,142 electrodes and 148,404 electrode pairs mapping onto 31 of 36 areas in the Desikan-Killiany parcellation (**Figure 1**, **Table 2**) (Desikan et al., 2006). Interactions were spatially localized (**Figure 7**, **Figure 10**, **Figure 14**), fluctuated over time (**Figure 4A**, **Figure 9**), and were consistent across subjects (**Figure 12**, **Figure 23**). We found 11,682 pairwise interactions between electrodes, summarized by 193 interactions between 31 Desikan-Killiany areas (**Figure 14**), and 2,387 interactions between 150 areas in a custom parcellation (**Figure 13**). The physiological interactome is accompanied by a comprehensive Supplementary Website showing each interaction, in individual and average brains, in different frequency bands, using multiple visualization tools (http://braininteractome.com). Coverage of the human cortex through the 4,142 electrodes was extensive (**Figure 1**, **Table 2**), but not exhaustive. Because mapping electrodes onto an average brain necessarily reduces the precision of reported locations, the Supplementary Website depicts all interactions in each subject's own brain without any distortions. The networks in humans and monkeys showed small-world properties that allow efficient and robust communication between brain regions (**Figure 19**, **Figure 20**).

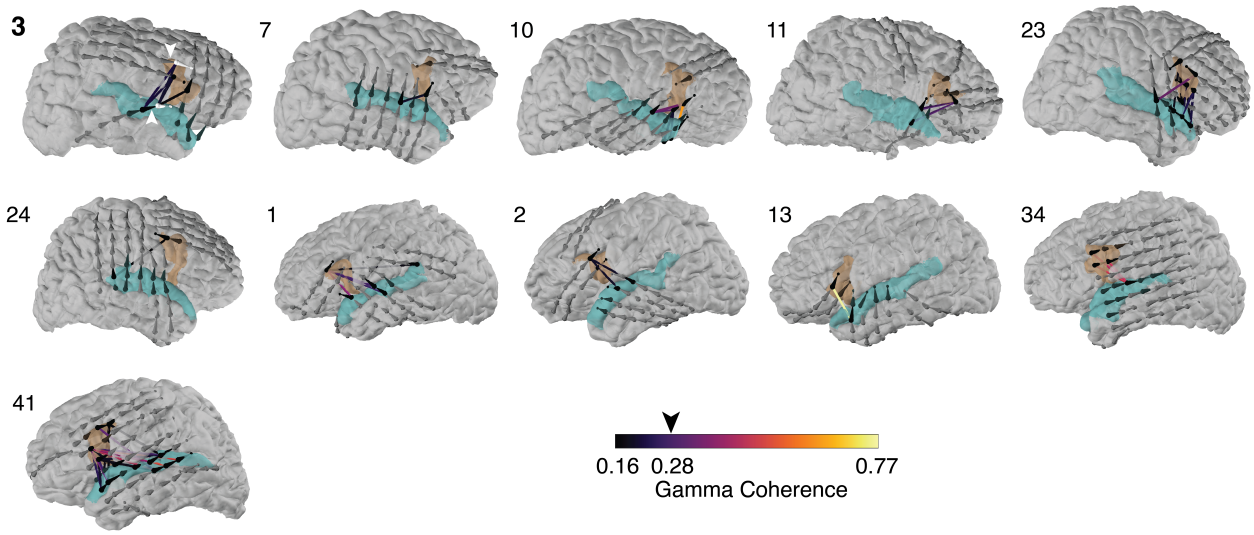

Figure 23. Between-subject comparisons for the gamma band coherence between Superior Temporal Gyrus and Pas Opercularis.

Following the format from **Figure 12A**, here we report the gamma band coherence [30,100) Hz. The average gamma band coherence was 0.28±0.13 (mean ± SD, n=51, black arrow in color scale).

We used the coherence between IFPs to measure interactions (Nunez et al., 1997). This metric has been used extensively to assess neural communication (Baldauf and Desimone, 2014; Bastos et al., 2015; Bullmore and Sporns, 2009; Fries, 2005; Gregoriou et al., 2009; Madhavan et al., 2019; Zhou et al., 2016). We validated the coherence metric against anatomical connections and physiological interactions (**Figure 7**). Additionally, the interaction matrix and small-world network properties were robust to the choice of the interaction metric (**Figure 24, Table 6**) and were also detected in individual subjects (**Table 5**).

Physiological interactions did not reflect global activity changes but instead were locally specific (**Figure 10**). Coherence measurements revealed spatially restricted subnetworks of interactions (**Figure 12, Figure 14, Figure 7B, Figure 11D, Figure 25D**). We refer to the spatiotemporal scale studied here as *mesoscopic*, distinguishing these measurements from finer

resolution in anatomical connections between individual neurons (Kasthuri et al., 2015), and coarser-resolution interactions evaluated by EEG (Nunez et al., 1997), MEG (Michalareas et al., 2016), or fMRI (Baldauf and Desimone, 2014; Glasser et al., 2016; Thomas Yeo et al., 2011).

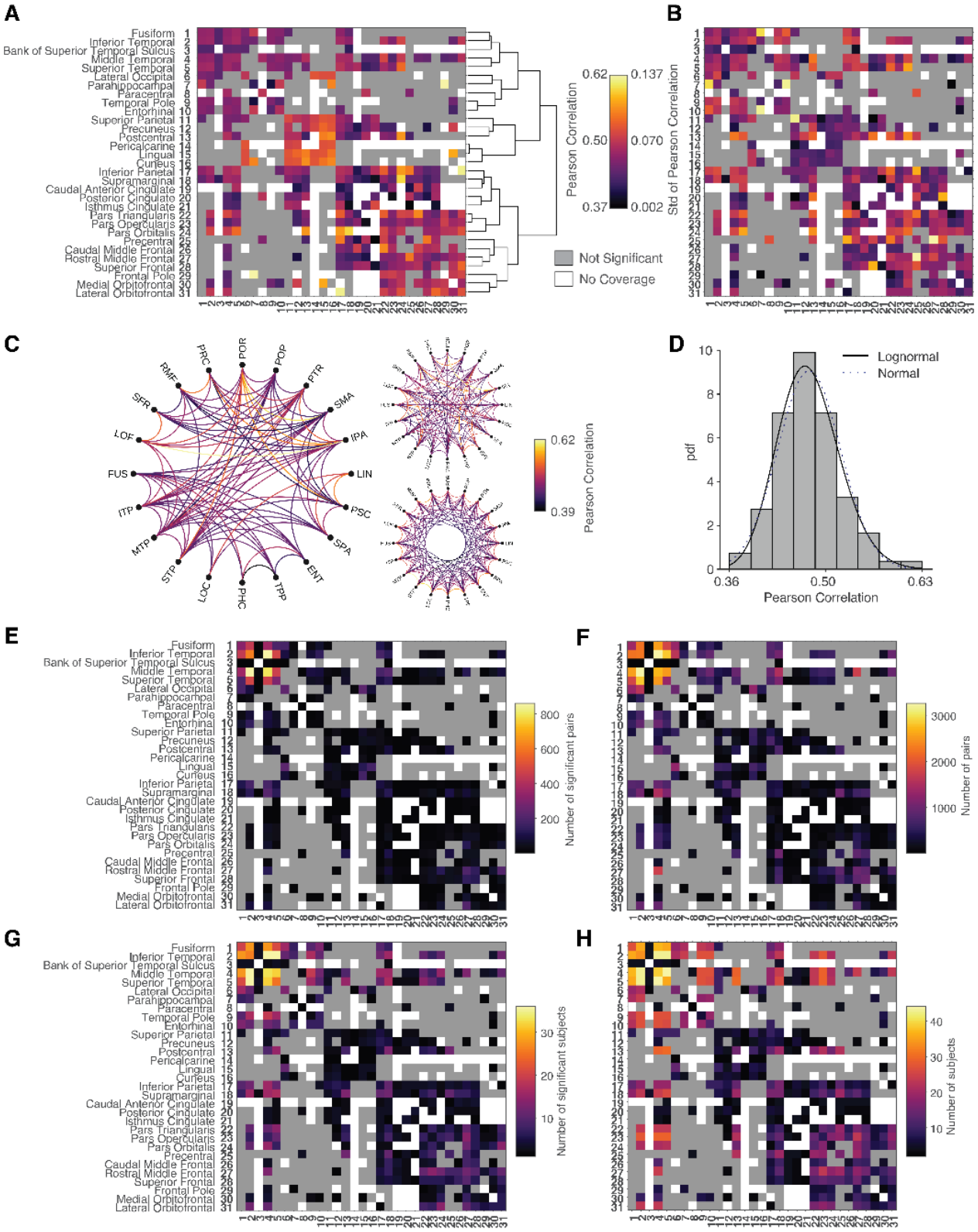

Figure 24. Pearson correlation showed similar networks and small-worldedness.

The main results were consistent when considering Pearson correlation as an alternative metric to broadband and gamma band coherence. (**A**) Following the format from **Figure 14**, this figure shows the between-area interactions calculated using the Pearson correlation coefficient. The matrix in **Figure 24A** was similar to the one in **Figure 14** ($r = 0.27$, $p = 0.001$, $n = 138$), and to the gamma band matrix in **Figure 26** ($r = 0.25$, $p = 0.003$, $n = 138$). (**B**) Standard deviation of Pearson correlation interactions, following the format from (**A**). (**C**) The edge-complete Pearson correlation network showed small-world properties (format as in **Figure 19**). The small-world coefficient was $\sigma=1.8$ (95% CI: 1.7, 2.1), satisfying the range $\sigma>1$. The small-world measurement was $\omega=-0.40$ (95% CI: -0.40, -0.39), satisfying the range $-0.5< \omega <0.5$ (**Methods**). Detailed network coefficients are shown in **Table 6**. (**D**) Distribution of 182 between-area Pearson correlation interaction values (format as in **Figure 16**). (**E-H**) Number of significant and total bipolar pairs and number of subjects used for Pearson correlation calculations (format as in **Figure 15B-E**).

	Coherence	Pearson Correlation
L	5.23	3.27
C	0.49	0.71
L_{random}	4.36 (0.03)	3.07 (0.01)
$L_{lattice}$	4.93 (0.004)	2.99 (0.001)
C_{random}	0.34 (0.01)	0.38 (0.02)
$C_{lattice}$	0.40 ($6 \cdot 10^{-5}$)	0.53 ($5 \cdot 10^{-5}$)
σ	1.2 (0.03)	1.77 (0.10)
ω	–0.41 (0.01)	-0.40 (0.004)

Table 6. Small-world network measures are similar when using Coherence or Pearson correlation as a metric.

Following the format in **Table 4**, here we show small-world network properties of the graph formed using the Pearson correlation coefficient as an alternative to the coherence. The small-world coefficient σ (Humphries and Gurney, 2008) and small-world measurement ω (Telesford et al., 2011) both indicated the presence of small-world networks.

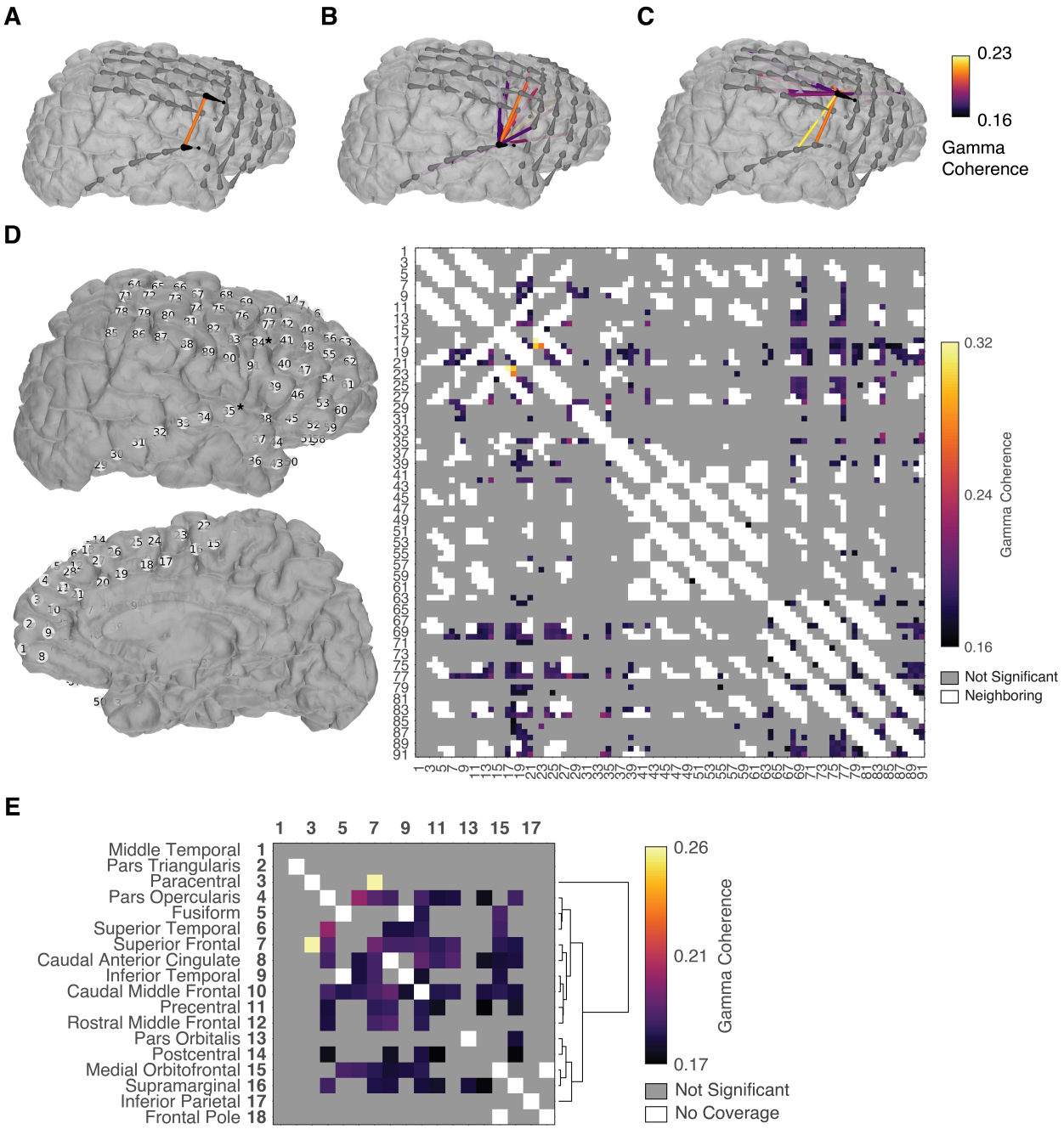

Figure 25. Spatial specificity of time-averaged coherence values in the gamma band.

Following the format in **Figure 11**, here we report results using the gamma band coherence [30, 100) Hz for subject 3. A total of 280 electrode pairs (9%) showed statistically significant and temporally consistent interactions. The coherence for the interaction between the right Superior Temporal gyrus and the right Pars Opercularis can be found in row 6, column 4.

The broadband coherence included signals between 0.5 and 125 Hz. Multiple studies described interactions in narrower frequency bands, particularly in the gamma range (Bastos et al., 2015; Gregoriou et al., 2009; Madhavan et al., 2019). We repeated all analyses for the following 4 bands: 3-8 Hz (theta), 8-12 Hz (alpha), 12-30 Hz (beta), and 30-100 Hz (gamma) (Supplementary Website). Filtering the data in these different frequency bands does not assume oscillatory activity to be the origin of our measures (Miller et al., 2009), but rather describes potentially different bands of communication between areas. The general principles of spatial specificity, temporal fluctuations and small-world properties were consistent across the different frequency bands. However, the fine details of the interaction networks depended on the frequency band. These differences open up the intriguing possibility of multiplexing different routes of communication within the network (Buzsaki, 2006).

The millisecond temporal resolution of IFP recordings was critical to uncovering rapid interactions. Indeed, most previous studies have focused on short-lived interactions during behavioral tasks (Bastos et al., 2015; Gregoriou et al., 2009; Madhavan et al., 2019; Zhou et al., 2016). The results in **Figure 7**, **Figure 13**, **Figure 14** average short-lived interactions spanning a diverse range of unique and repeated behaviors over long periods (**Figure 4**). We captured high frequency (30 - 100 Hz) interactions with the gamma coherence metric (**Figure 26, Figure 27**). Subjects were bedridden; awake behaviors included rest (Glasser et al., 2016; Thomas Yeo et al., 2011), social interactions, eating, and watching movies. Most of the "housekeeping" and pervasive cognitive functions, including visual/auditory processing, language, and internal thought processes are reflected in the interactome. Infrequent brain interactions contribute to a lesser extent to the current results. The temporal dynamics of the coherence signals are averaged in our estimates of the interactivity (Liégeois et al., 2017; Zalesky et al., 2014).

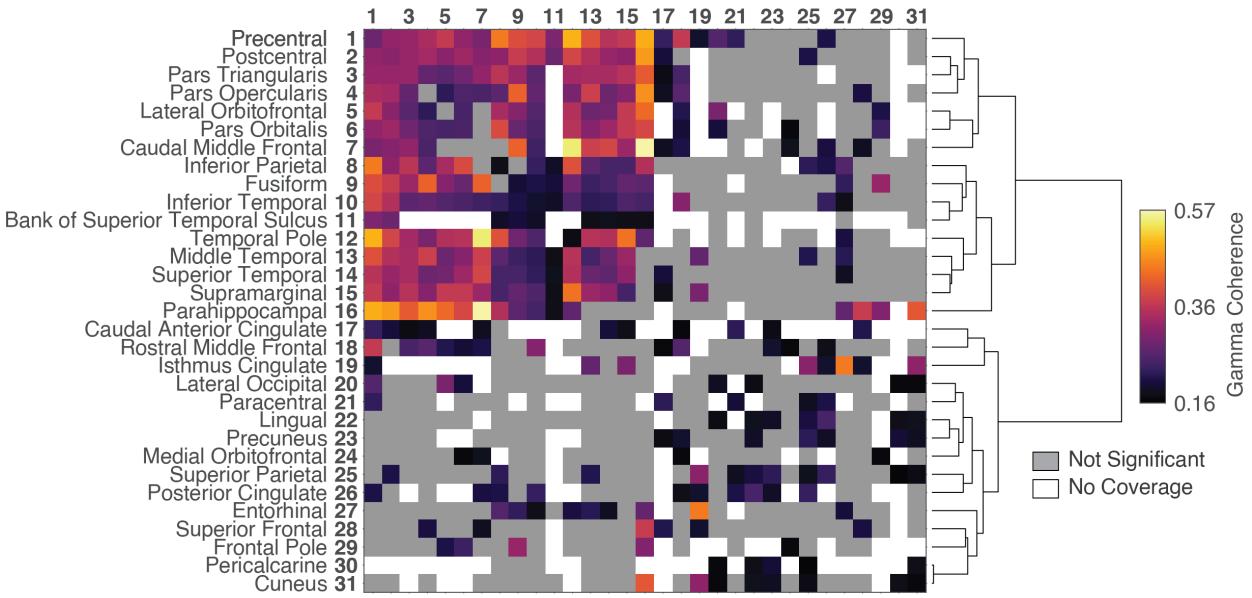

Figure 26. Subject-averaged gamma band coherence between areas in the Desikan-Killiany parcellation.

Following the format from **Figure 14**, here we report the gamma band coherence [30,100) Hz. The interaction between the Superior Temporal gyrus and Pars Opercularis as illustrated in **Figure 23** can be found in row 14, column 4. The dendrogram shows relationships between Desikan-Killiany areas, based on their similarities in gamma band coherence values.

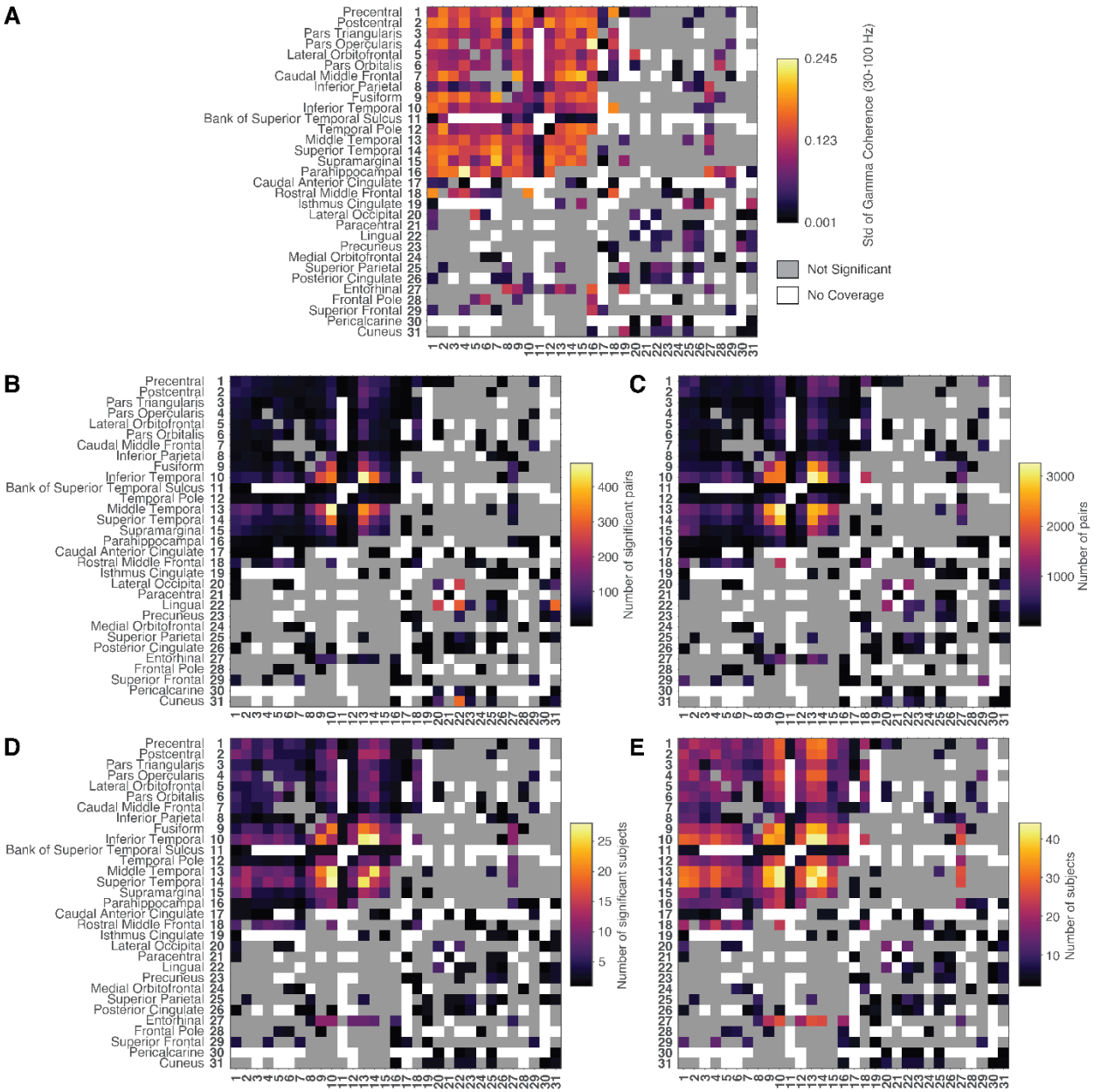

Figure 27. Gamma coherence standard deviation across bipolar electrode pairs and across subjects.

Following the format from **Figure 15**, here we show the standard deviations of the gamma coherence and the numbers of significant and total bipolar pairs and subjects used for calculations.

The interaction strengths follow a log-normal distribution (**Figure 16**), in line with log-normal distributions in anatomical tract-tracing network weights (Buzsáki and Mizuseki, 2014;

Ercsey-Ravasz et al., 2013; Gămănuț et al., 2018; Markov et al., 2012). Such distributions are a key property of hierarchical networks where few weaker long-distance projections are amplified by local circuits that make up the majority of connections (Markov et al., 2013b). The current results extend this notion to mesoscopic physiological interactions.

In small-world networks, it is possible to rapidly convey information from any point in the network to any other point in a small number of steps and edges are configured economically to facilitate both global and local integration (Bullmore and Sporns, 2012; Telesford et al., 2011). The coherence weights used for our network analyses are distinct from measures used in other modalities and in anatomical networks (Muldoon et al., 2016). Despite these differences, the combination of local and long-range connectivity gave rise to a network topology revealing small-world characteristics (**Table 4**, **Figure 19**, **Figure 20)**, consistent with properties of anatomical connectomes (Bassett and Bullmore, 2017). Small-world networks efficiently organize information flow by facilitating both local and global connectivity (Watts and Strogatz, 1998). We speculate that the coherence network characterized here may facilitate information transmission across the cortex (Telesford et al., 2011). The existence of weaker, long-range interactions have been shown to be critical for anatomical network specificity (Markov et al., 2013a). The coherence metric captured these critical "shortcut" interactions.

We examined coherence in relation to the subjects' sleep and wake state and in relation to four naturalistic behavioral annotations (**Figure 21**). We were able to model this relationship using a nonparametric classification model and found cross-validated accuracies of up to 69%, demonstrating that it was possible to decode sleep and behavior from coherence measurements. Our study of interactions in the context of sleep achieved a wider brain area coverage and larger number of sleep/wake cycles by improving on both the number of subjects and duration of

recording per subject from the prior state-of-the-art (Kramer et al., 2011). Our analysis of naturalistic behaviors extends existing characterizations of individual brain areas to mesoscopic region pairs (Wang et al., 2018; Wang et al., 2016). Our inter-rater reliability score for sleep annotations as measured the kappa statistic (**Figure 22B**) was comparable to that of similar studies of sleep (Danker-Hopfe et al., 2009; Magalang et al., 2013).

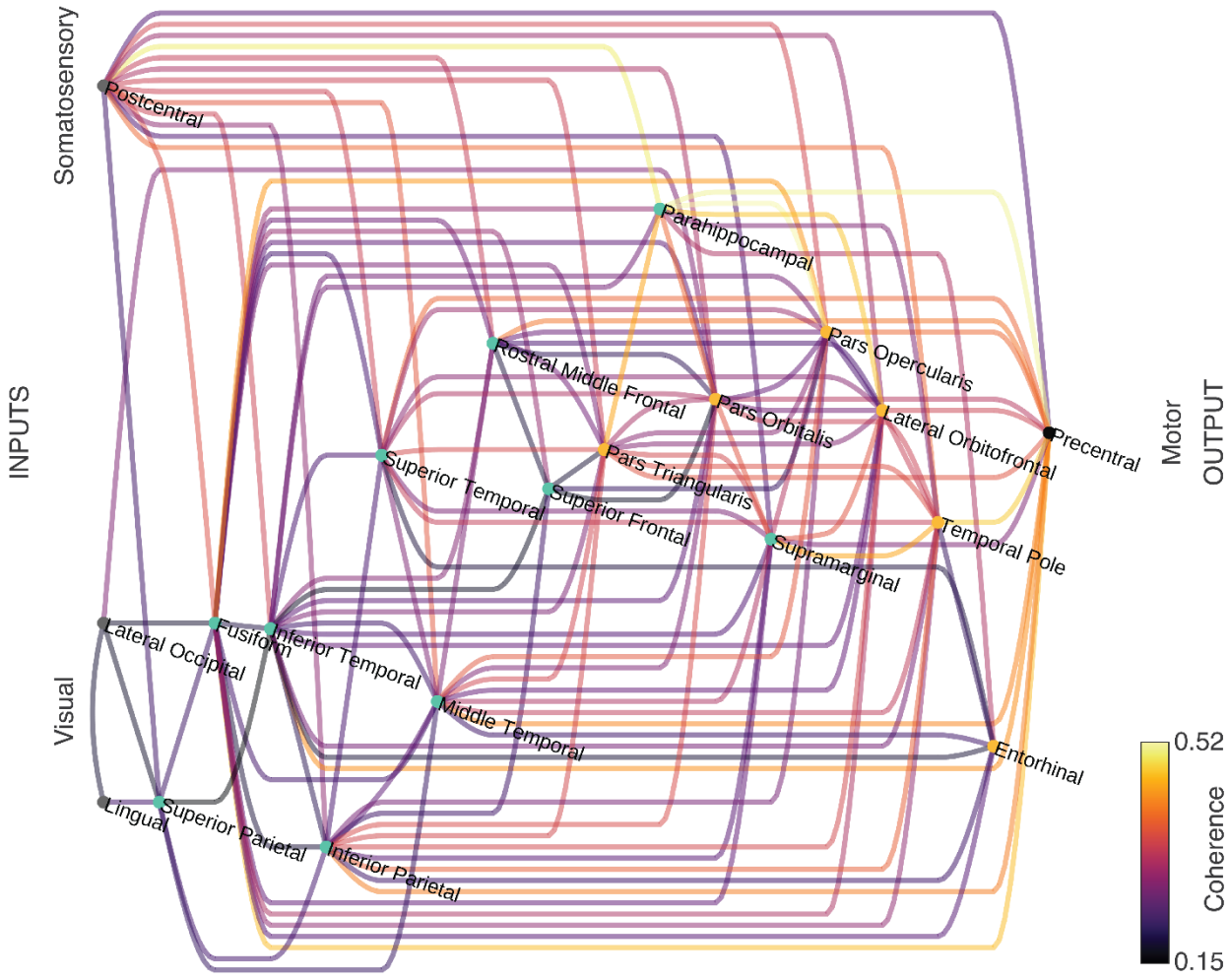

Figure 28. The brain interactome as a functional model.

As an illustrative model, the edge-complete network from **Figure 19** is re-arranged here to show three Desikan regions (Desikan et al., 2006) overlapping with visual (Grossman et al., 2019) and somatosensory (Penfield and Rasmussen, 1950) input areas (Van Essen et al., 2013) on the left,

marked by gray nodes, and one Desikan region corresponding to motor output areas (Penfield and Rasmussen, 1950) on the right, marked by the dark gray node. Colored nodes indicate cluster membership after performing k-means clustering with $k = 2$.

The results presented here provide initial steps towards the mesoscopic characterization of the flow of information in the human brain. The physiological interactome should not be thought of as static, let alone immutable. Interactions between brain areas can be modified over developmental time scales, and much more rapidly during cognitive tasks. The network structure described here provides a reference map for future studies of brain physiology and pathology. To aid such studies, we re-arranged the edge-complete network from **Figure 19** to visualize nodes in relation to their input or output function (**Figure 28**). The Lingual and Lateral Occipital areas were selected as input nodes due to their overlap with highly conserved anatomical landmarks (Van Essen, 2004), myelinated regions of the cortex (Van Essen et al., 2013), and correspondence to areas previously shown to correlate to activations of artificial neural networks during a visual viewing task (Grossman et al., 2019). The Precentral area was selected as the output node due to similar anatomical considerations. This input/output arrangement (Buzsáki, 2013) contextualizes areas and interactions in terms of their putative overlaps with regions of known computational specialization.

Methods

Supplementary Website

Additional materials and interactive rendering of the results can be obtained from the following Supplementary Website: http://braininteractome.com

The web materials include:

- Maps of all physiological interactions in the average brain
- Maps of all physiological interactions in each of 48 subjects
- Maps of all physiological interactions in additional frequency bands
- Interactive maps that allow the user to rotate the brains, highlight specific areas and electrodes, and visualize individual pairs of interacting areas and electrodes.

Note about the displays in the Supplementary Website: we use line objects to show interactions between two positions in the Supplementary Website. Bipolar electrodes positions were first defined on a three-dimensional coordinate system using the *iELVis* package (Groppe et al., 2017). These positions were represented by spheres plotted on reconstructed pial surfaces. Next, a series of line segments were constructed to connect pairs of spheres. The lines connecting different electrodes *do not represent an anatomical basis for interactions, nor are they meant to represent axonal tracts*. These representations were used only for visualization purposes. To construct these line segment paths, electrode positions were first localized on spherical surfaces using *freesurfer* tools (Dale et al., 1999). The path between these two electrode vertices was then determined by tracing the great-circle that passed through these two points, taking the shorter of the two possible paths. The path was mapped back onto the pial surface of the corresponding subject following a nearest-neighbor assignment of points to the great-circle path. Meshes were generated from each path using the *tubeplot* package (Wesenberg, 2016). Following these preparatory steps, graphical elements were combined into one common view in the Supplementary Website. The website was made using *blender* (The Blender Foundation, Amsterdam, Netherlands) and *blend4web* (Triumph LLC, Moscow, Russia).

Custom brain parcellation

Electrode localization

In some cases (**Figure 13, Figure 17**), we rendered electrodes from different subjects onto an average brain. Registration of electrodes from individual subjects onto the average brain was done using *iELVis*, followed by cross-hemispheric registration using *freesurfer* to register electrodes from the *fsaverage* right and left hemisphere surfaces onto the symmetric fsaverage_sym right hemisphere surface. Electrodes from all 48 subjects on a common pial surface (**Figure 13A**) revealed extensive coverage over a large expanse of the cerebral cortex surface. Electrode positions were measured on a three-dimensional coordinate system and were used to calculate inter-electrode distances for neighborhood identification (**Figure 3B**).

We summarized the electrode locations by mapping them onto one of 36 brain areas based on the parcellation of the Desikan-Killiany atlas (Desikan et al., 2006) using the *recon-all* function in *freesurfer*. **Table 2** provides summary information about the number of electrodes in each of these 36 areas. We also present results under a custom parcellation based on electrode coverage (**Figure 13**).

Construction of a 150-area parcellation

The Desikan-Killiany parcellation is based on anatomical landmarks denoted by brain sulci and gyri. When describing electrode locations, we also used an alternative custom parcellation map based on the density of electrode locations. We constructed a 150-area parcellation of

locations that best matched the electrode coverage (**Figure 13C**, **Figure 17**). This parcellation was constructed by first considering the 3,615 bipolar electrodes across all subjects and their coordinates on the *fsaverage_sym* pial surface (**Figure 13A**). Distances between these coordinates were calculated and used to define regions based on electrode coverage (**Figure 13B**). We defined 150 areas, a number approximating that of the multimodal parcellation of brain regions in (Glasser et al., 2016). Following the reconstruction procedure computed by the *freesurfer* package (Dale et al., 1999), 3,615 bipolar electrodes were given coordinates in the corresponding subject spaces. These coordinates were then transformed into the fsaverage_sym space using the *iELVis* package (Groppe et al., 2017). The 3,615 by 3,615 distance matrix was calculated by taking the arclength of all pairwise combinations of the spherical electrode coordinates **u** and **v**, using *freesurfer* spherical reconstructions (Dale et al., 1999). The *freesurfer* default radius of 100 millimeters for spherical surfaces was used as the value for *r* to calculate the distance:

$$distance = r\theta = r\ \tan^{-1}\frac{\|\boldsymbol{u}\times\boldsymbol{v}\|}{\boldsymbol{u}\cdot\boldsymbol{v}}$$

Using this distance matrix, each of the 3,615 bipolar electrodes was assigned to one of 150 clusters to form sets of coordinates delineated into custom brain areas. The k-means clustering algorithm was computed using the function *kmeans* in MATLAB. Multiple runs of the algorithm were used to overcome the noise introduced by random initializations. The final version was taken as the clustering with the minimum total within-cluster variance after running the algorithm for 900 random initializations (**Figure 13**).

In addition to clustering bipolar electrodes into 150 regions, we further defined region membership for the other vertices making up the *fsaverage_sym* surface. Each vertex of the

fsaverage_sym surface was given membership in one of the 150 regions by considering the 3-nearest-neighboring bipolar electrodes. The majority cluster out of 3 was assigned to that vertex. The distance was computed using the same arclength definition as before. The rendering of the new parcellation as shown in **Figure 13B** revealed 150 regular and non-overlapping regions. Regions contained 5 to 78 bipolar electrodes, with an average of 24±14. Regions measured between 8.8 mm to 28 mm at their widest dimension, with a mean distance of 7.7±1.9 mm across.

Temporal consistency

Coherence values were computed for every segment of size T over the entire data set (**Table 1**). For each pair of bipolar electrodes, given the number of segments where coherence was above the significance threshold, n, and the total number of segments, N, we defined the temporal consistency as n/N. The coherence between two electrodes was defined to be consistent over time if the temporal consistency was above 5%. This threshold was well above (i.e., more conservative), than the one obtained by considering a Bonferroni-corrected binomial distribution based on each time segment. In a simulated dataset of coherence values generated by randomly sampling from the fitted null distribution, only 1 bipolar electrode pair was temporally consistent out of 124,865 bipolar electrode pairs across the 48 subjects. Thus, the method was confirmed to be robust at controlling the Type-I error rate.

To summarize the interactions occurring through time for each bipolar electrode pair, we defined the time-averaged coherence value to be the average coherence of those n segments where coherence was above the significance threshold (**Figure 4B-C, Figure 5**). The exclusion of

coherence values below the threshold ensured a high-quality metric at the cost of potentially missing weak interactions with low coherence magnitudes.

Between-subject consistency

To summarize physiological interactions across subjects, it was necessary to reconcile electrode maps from one subject to another. We considered two types of anatomical maps for these analyses: (i) the locations of all electrodes were registered onto a standardized cortical parcellation (Desikan et al., 2006) (see "Electrode localization"; e.g., for subject 3, the 91 bipolar electrodes mapped onto 18 areas, **Figure 11E**); (ii) electrodes were mapped onto our custom 150-area parcellation (see "Custom brain parcellation").

Area-wise interactions

Once each bipolar electrode was assigned to a brain area, we combined results from multiple bipolar electrode pairs mapping onto the same pair of areas. In the example shown for subject 3 in **Figure 12**, there were 8 bipolar electrodes in the Superior Temporal Gyrus and 3 bipolar electrodes in the Pars Opercularis, yielding a total of 24 bipolar electrode pairs between these two areas. For a given pair of areas *i* and *j*, the symmetric matrix *M(i,j)* indicates the total number of bipolar electrode pairs. The size of *M* was 36 by 36 for the Desikan-Killiany parcellation (**Figure 14**), and 150 by 150 for the custom parcellation (**Figure 13**). Only 31 of the 36 areas had electrode coverage (**Figure 14, Table 2**). We followed the same procedure for the monkey data, resulting in a 39 by 39 matrix (**Figure 7B**).

Bipolar electrode pairs mapping onto the same area were also considered. In some cases, significant interactions occurred within brain areas, as shown on the diagonal of **Figure 14**, **Figure 26**. These interactions were possible when an area pair involved an electrode pair where both electrodes localized to the same area. The distance criterion was applied to all analyzed electrodes (see **Methods**, **Figure 3**); thus, these intra-areal interactions mostly occurred in areas with a large surface. The interactions reported here represented interactions between sub-areas and do not necessarily represent a type of internal correlation. The interaction networks calculated using the custom parcellation (**Figure 13C, Figure 17A**) did not contain these intra-areal interactions. The larger number of areas resulted in smaller surfaces that did not accommodate electrode pairs that could pass the distance criterion (**Figure 13B**).

Between-subject consistency

We combined the area-wise interaction matrices across subjects. Given the number of bipolar electrode pairs with significant interactions $m(i,j)$ for a given pair of areas i and j, and the total number of bipolar electrode pairs $M(i,j)$, the between-subject consistency was defined as $m(i,j)/M(i,j)$. The significance of the between-subject consistency was determined in a similar way as for the temporal consistency. A threshold of between-subject consistency ≥10% was used to define significant interactions for a pair of brain areas. An analysis of simulated coherence values using the null hypothesis was conducted to validate the methodology. The method reported no pairs of brain areas showing significant interactions in this null dataset.

Electrode coverage

The placement of intracranial recording electrodes varied from subject to subject (**Figure 1**, **Table 2**). To minimize potential sampling bias when combining multiple subjects, we restricted the analyses to $M(i,j) \geq 10$. We further restricted analyses to cases where bipolar electrode pairs came from at least 2 subjects.

Subject-averaged coherence

The coherence values from significant electrode pairs mapping onto each brain area pair were averaged to give the area-pair coherence (color-mapped values in **Figure 14**). We performed this averaging for each of the 193 significant between-area interaction sets, each of which contained 401±518 electrode pairs, and 14±9.2 unique subjects. The standard deviations, numbers of significant and total pairs, and the numbers of subjects spanned by these pairs is shown in **Figure 15**. For the gamma frequency band, in each of the 184 significant interactions between areas (color-mapped values in **Figure 26**), there were 377±515 electrodes pairs and 13±10 unique subjects. The standard deviations of the gamma coherence, numbers of significant and total pairs and the numbers of subjects spanned are shown in **Figure 27**. For each of the 2,387 significant interactions between areas in the custom parcellation (**Figure 13C**), there were 23±18 electrode pairs and 7.4±3.9 unique subjects. For the gamma frequency band, in each of the 2,110 significant interactions between areas in the custom parcellation (**Figure 17A**), there were 23±14 electrode pairs and 7.4±4.0 unique subjects. In the simulated dataset where coherence values were generated by randomly sampling from the fitted null distribution, no significant interactions were found in the broadband coherence or other frequency bands.

Log-normal distribution

We assessed whether the coherence values from the interaction networks shown in **Figure 14** and **Figure 26** for the Desikan-Killiany areas (Desikan et al., 2006), and the networks shown in **Figure 13C** and **Figure 17A** for our custom parcellation, were fit by a log-normal distribution. These distributions are shown in **Figure 16A-B** for the Desikan-Killiany areas and in **Figure 16C-D** for the custom parcellation. Areas with insufficient electrode coverage or nonsignificant interactions were not considered for distribution fits. A one-sample Kolmogorov-Smirnov test was performed for the empirical observations using the Matlab function *kstest* after normalizing coherence values according to a standard normal distribution. The resulting p-value was interpreted as significantly deviating from a standard normal distribution if $p < 0.05$. In cases where we performed the test against a log-normal distribution, we performed the *kstest* algorithm after taking the logarithm of coherence values. We found no significant interactions (as shown in **Figure 14, Figure 26**) when we sampled coherences from the null distribution, thus there was no opportunity for log-normal assessment for the distribution of coherence values under the null distribution.

Robustness of the subject-averaged coherence results

We assessed the robustness of our subject-averaged coherence metric by splitting our dataset in half based on the electrode pairs, calculating the physiological interaction network individually for the two halves, and comparing the results. Of the 193 significant brain area pairs reported from the original 124,865 bipolar pairs (see **Results**), there were 186 (96%) brain area

pairs that were found to be significant in both half datasets. The difference in coherence values between the two halves was 0.005±0.048 and was not significantly different (p=0.78, two-sided rank-sum test, n=186). The gamma-band frequency coherence was also found to be robust. Of the 184 significant brain area pairs, there were 174 (95%) brain area pairs that were found to be significant in both half datasets. The difference in gamma coherence values between the two halves was 0.001±0.055 and was not significantly different (p=0.75, two-sided rank-sum test, n=186).

As an additional control, instead of splitting the data by electrode pairs, we further assessed the robustness of our subject-average coherence metric by splitting the dataset in half by time windows. For each of 48 subjects, coherence time windows were segmented into 4-hour epochs. These epochs were split evenly to form two derived datasets, each receiving half the amount of data from the full dataset. Of the 193 significant brain area pairs reported for the full dataset, there were 186 (96%) brain area pairs that were found to be significant in both half datasets. There was no significant difference between the coherence values in the two halves (p=0.88, two-sided rank-sum test, n=186, absolute difference of 5.4%±6.1%). The gamma frequency coherence was also found to be robust. Of the 184 significant brain area pairs, there were 179 (97%) brain area pairs that were found to be significant in both half datasets. There was no significant difference between the gamma band coherence values in the two halves (p=0.79, two-sided rank-sum test, n=179, absolute difference of 3.3%±3.7%).

The current study examines a large dataset encompassing 6,024 hours of neurophysiological recordings. To assess whether short recordings could be sufficient to elucidate brain interactions, we considered 130 random segments of 10-minute duration (encompassing 60 segments of 10-second duration) for each of the 48 subjects. Of the 193 significant brain area pairs reported for the full dataset, there were 142 (74%) brain area pairs that were found to be significant

in both the short segment and in the complete data. The coherence values in the complete data and short samples were significantly different (p=5·10-4, two-sided rank-sum test, n=142, absolute difference of 17.2%±14.2%). The gamma frequency band coherence showed similar results: of the 184 significant brain area pairs, there were 120 (65%) brain area pairs that were found to be significant in both the short segments and in the complete data. The gamma band coherence values in the complete data and short segments were significantly different (p = 8·10-6, two-sided rank-sum test, n=120, absolute difference of 19.5%±13.3%).

Both the number of electrodes (**Table 1**) and the regions covered (**Table 2**) varied widely across subjects. To assess the effect of individual subjects on the results, we considered the 193 between-area interactions shown in **Figure 14** and randomly removed *n* subjects from the analysis. After removing all bipolar electrode pairs of the selected subjects, each of the 193 area pair coherence averages were re-calculated using data from the remaining subjects. We then examined the interactome matrix (**Figure 14**), the log-normal distribution, and the small-world network properties.

Interactome matrix

After 50,000 random removals and re-calculations, there was a high correlation between the original 193 significant coherences and the mean of the random re-calculations (r = 1.00, p = 0.00, n = 193) for *n* = 1. This correlation remained high (r = 0.99, p = 0.00, n = 193) for *n* = 24 when half of the subjects were randomly removed. For the broadband signals, the maximum absolute difference between the original 193 significant coherences and the mean of the random re-calculations was 0.003 for *n*=1 (this maximum occurred for the interaction between Parietal

Gyrus and Pars Orbitalis and represented 0.9% of the original coherence value of 0.36 between these two areas), and 0.06 for *n*=24 (this maximum occurred for the interaction between the Cuneus and Parahippocampal Gyrus and represented 16.5% of the original value of 0.37 between these two areas). In the gamma frequency band, the maximum absolute difference between the 184 significant gamma coherence interactions and the mean of the random re-calculations was 0.002 for *n*=1 (this maximum occurred for the interaction between the Pars Orbitalis and Frontal Pole and represented 0.9% of the original coherence value of 0.23 between these areas), and 0.04 for *n*=24 (this maximum occurred for the interaction between the Pars Orbitalis and Supramarginal gyrus and represented 9.7% of the original coherence value of 0.37 between these areas) (**Figure 26**).

Log-normal distribution

The distributions of coherence values remained log-normal after re-calculation. The deviation from a normal distribution at $n = 1$ was significant ($p = 0.033$, Kolmogorov-Smirnov test), while a deviation from a lognormal distribution was not ($p = 0.59$, K-S test). For $n = 24$, the deviation from a normal distribution was no longer significant ($p = 0.064$, K-S test), but the deviation from a lognormal distribution was not significant ($p = 0.56$, K-S test). Lognormality was less robust in the gamma coherence values, where for $n = 1$, the K-S test p-value was 0.052 for deviation from a normal distribution, and 0.12 for deviation from a lognormal distribution. For $n = 24$, the K-S test p-value was 0.091 for deviation from a normal distribution, and 0.23 for deviation from a lognormal distribution. Thus, taking these analyses together, our metric of inter-areal coherence was robust to variations across individual subjects.

Robustness of small-world properties

Following our analysis of randomly re-calculated coherence values after removing subjects, we found small-world properties in the re-calculated networks. For random removal of *n* = 1 subjects, there were 20 nodes remaining (of the original 20 nodes, as shown in **Figure 19**) that formed an edge-complete network suitable for network analysis. The re-calculated small-world coefficient σ (Humphries and Gurney, 2008) and small-world measurement ω (Telesford et al., 2011) showed small-worldedness: σ = 1.20 (95% CI: 1.14 to 1.26), ω = -0.40 (95% CI: -0.42 to -0.39) for the broadband coherence network, and σ = 1.28 (95% CI: 1.19 to 1.36), ω = -0.44 (95% CI: -0.45 to -0.43) for the gamma coherence network. For random removal of *n* = 24 subjects, there were again 20 nodes remaining that formed an edge-complete network. The resulting network measures also showed small-worldedness: σ = 1.21 (95% CI: 1.14 to 1.27), ω = -0.41 (95% CI: -0.42 to -0.40) for the broadband coherence network, and σ = 1.28 (95% CI: 1.19 to 1.37), ω = -0.44 (95% CI: -0.45 to -0.42) for the gamma coherence network.

Distance metric

For each area *i*, the *n*-dimensional vector $\boldsymbol{c}(i)=\{c_1(i),c_2(i),\ldots,c_n(i)\}$ contained the coherence values between that area and each of the other areas of the parcellation of interest. The distance *d(j,k)* between two areas *j* and *k* was calculated by taking the Euclidean distance between vectors ***c(j)*** and ***c(k)***. Missing coherence values with insufficient coverage were omitted from the distance calculation.

Hierarchical clustering algorithm

Hierarchical clustering was computed according to Ward's method (Ward, 1963). The resulting hierarchical clustering was visualized as a dendrogram. The position on the horizontal axis corresponded to the relative value of the within-group variance metric, where shorter distances indicated better group fit. Hierarchical clustering was performed using the following functions in MATLAB: *linkage, optimalleaforder, dendrogram*.

Hierarchical clustering observations

Hierarchical clustering provided an initial step for examining interaction networks (**Figure 7, Figure 11E, Figure 13, Figure 14, Figure 17, Figure 25E, Figure 26**). High-level clusters mapped approximately onto the temporal-parietal, lateral prefrontal, medial prefrontal, and occipital lobe areas. Brain areas with similar functional localization also had similar physiological interactivity patterns. The clustering algorithm was not given anatomical information *a priori*, yet we found correspondence between the clustered order and anatomic proximity. For example, the Precentral gyrus and Postcentral gyrus were clustered together (see areas *14*, *15* in **Figure 14**, **Figure 26**). These neighboring areas are related both functionally and anatomically (Van Essen et al., 2013).

Network graph analyses

We considered the graph formed by brain areas as nodes and interactions as edges. We performed several calculations described in this section to characterize the structure of this interaction network graph, both in monkeys (**Figure 20A**) and in humans (**Figure 19A**).

In monkeys, the Markov-Kennedy areas (Markov et al., 2012) served as the nodes. Of the 91 areas in the atlas, 39 areas were covered by intracranial electrodes (**Figure 7B**). In humans, the Desikan-Killiany areas served as the nodes (**Figure 14**). Of the 36 areas in the atlas, 31 areas were covered by intracranial electrodes.

Missing values

We converted networks into edge-complete networks by removing nodes with incomplete coverage. The node with the highest number of missing values was identified and removed from the adjacency matrix. This operation removed all edges associated with the identified node. The procedure was repeated iteratively until no missing values were present. An 18 by 18 matrix remained in the macaque physiological interaction network (**Figure 20**), and a 20 by 20 matrix remained in the human network (**Figure 19**).

Network graph analyses calculations

To investigate whether the network graphs showed small-world properties, we calculated the characteristic path length (L), and the clustering coefficient (C) (Humphries and Gurney, 2008; Muldoon et al., 2016; Telesford et al., 2011; Watts and Strogatz, 1998).

Two small-world indices were derived from the values of L and C for both the original networks and generated random and lattice networks described below. Physiological interaction network edges were constructed from the magnitude of coherence, ranging from 0 to 1. We used the extended definitions of L and C suitable for weighted networks as defined by (Muldoon et al., 2016), as implemented using the accompanying MATLAB code, with modifications. The weighted clustering coefficient C was computed using the definition given by (Onnela et al., 2005). To compute the characteristic path length L, the coherence values c_{ij} between nodes i and j were converted to path lengths $w_{ij} = 1 / c_{ij}$, following the definition from (Newman, 2001). The resulting distance matrix was the input to compute path lengths using the MATLAB function *graphallshortestpaths*. The magnitude of the path length between any two nodes was calculated as the sum of the individual distances of the edges making up the shortest path between them. The path length was calculated for all pairs of nodes, excluding self-paths, and the average of the resulting values represented the weighted characteristic path length. If a node was disconnected from the network (no edge connected it to any other node), it was excluded from the average calculation.

Random and lattice network generation

We compared the characteristic path length L and the clustering coefficient C of physiological interaction networks (**Figure 19A**) with two classes of null-hypotheses networks: (i) random network, assuming that the network arose from a random edge assignment (**Figure 19B**), and (ii) lattice network, assuming that the network arose from a regular lattice edge assignment

(**Figure 19C**)(Watts and Strogatz, 1998). Random and regular lattice networks were generated as described in (Muldoon et al., 2016). Randomization was performed by preserving weights from the edges of the original network. New networks were randomly initialized with the same number of edges and non-edges, where the order was determined by random permutation (*randperm* MATLAB function). To compute network indices, 10,000 random networks were generated to estimate confidence intervals. The same procedure was repeated for the macaque monkey interaction network (**Figure 20A**), with corresponding constructions of the random network (**Figure 20B**) and the lattice network (**Figure 20C**).

Lattice networks were generated while preserving coherence weights from the original networks. Network edge weights were sorted in descending order to prioritize assigning higher weights closer to the lattice center. The innermost radius was filled first, containing n edges across n nodes. The initial network was the ring network where all nodes were connected to every other node via one circular path. The order of weights for filling the ring was determined by random permutation using the n highest weights. Following this construction, the next innermost radius was filled containing up to n edges with the n next highest edge weights. These edges connected every node to its second-neighboring node. The procedure was repeated until all edge weights had been depleted. The final assignment at level k required the random permutation of $mod(m,k)$ weights, where m is the total number of edges in the network. Randomization was performed k times, with either n or $mod(m,k)$ number of elements per batch. The lowest edge weight from each batch was greater than or equal to the highest edge weight from the next batch.

For each network graph, we created the random and lattice null network models and calculated the respective L_{random}, $L_{lattice}$, C_{random}, and $C_{lattice}$ values. We sampled the random and lattice graphs with 10,000 initializations (**Table 4**, **Table 6**).

Small world network indices

We normalized the L and C metrics using the following definitions. The small-world coefficient (Humphries and Gurney, 2008) was defined as $\sigma = \frac{\gamma}{\lambda}$, where $\gamma = \frac{C_{network}}{C_{random}}$ and $\lambda = \frac{L_{network}}{L_{random}}$. $\sigma > 1$ indicate networks with small-world properties. We also considered the following alternative small-world measurement (Telesford et al., 2011), defined as $\omega = \frac{L_{random}}{L_{network}} - \frac{C_{network}}{C_{lattice}}$. Values $-1 \le \omega \le 1$ indicate networks with small-world properties.

We computed small-world coefficients in individual subjects when individual networks had adequate coverage and the network was reachable (13 of 48 subjects). Coherence values between Desikan-Killiany areas, as shown for subject 3 in **Figure 11E**, were used to compute small-world network coefficients. Following the same missing-value removal procedure as applied to the 31-node subject-averaged coherence value matrix (as shown in **Figure 14**), individual subject networks were converted to edge-complete networks. There were 5 of 48 subjects where this conversion resulted in an empty matrix and these subjects were omitted from further analysis. After omitting subjects without sufficient electrode coverage, an additional 30 subjects did not have sufficient interactions for calculating both σ and ω. The path length, clustering coefficient, σ and ω was calculated for the remaining 13 individual subject networks, where the number of nodes ranged from 4 to 12 (**Table 5**).

Functional model of the edge-complete network

The edge-complete network shown in **Figure 19** was rearranged to fit an input/output functional organization model of the brain (Buzsáki, 2019), shown in **Figure 28**. The MATLAB function *layout* was used with the 'layered' method, the areas Postcentral, Lateral Occipital, and Lingual as source, and the area Precentral as the sink. After removing the 3 source nodes, 1 sink node, the remaining 16-node network was used for k-means clustering using the MATLAB function kmeans with $k = 2$ clusters and 2400 random re-initializations. The ordering of the nodes from left to right were determined by cluster membership.

Robustness to the choice of coherence metric

As an alternative to the coherence metric, we computed the Pearson correlation coefficient for each pair of 10-second IFP signals and repeated the analyses. The Pearson correlation network (**Figure 24A**) revealed significant interactions between 182 pairs of Desikan areas. Of these area pairs, 138 (76%) overlapped with the 193 area pairs that showed significant interactions using the coherence metric (**Figure 14**). The correlation between the interaction matrices calculated using the Pearson metric and the coherence metric was significant (r = 0.27, p = 0.001, n = 138). The correlation between the Pearson metric and the gamma band coherence metric was also significant (r = 0.25, p = 0.003, n = 138). The standard deviation of the Pearson correlation values (**Figure 24B**) was comparable to that of the coherence metric (**Figure 15A**, **Figure 27A**). We also found small-world network properties in the Pearson correlation metric (**Figure 24C**, **Table 6**). The distribution of 182 Pearson correlation coefficients did not deviate from a log-normal distribution (p = 0.71, n = 182, Kolmogorov-Smirnov test), or from a normal distribution (p = 0.36, n = 182,

Kolmogorov-Smirnov test) (**Figure 24D**). The numbers of significant bipolar pairs and numbers of significant subjects using the Pearson correlation metric (**Figure 24E-H**) was similar to those using the coherence metric (**Figure 15B-E**, **Figure 27B-E**). Therefore, the main findings were robust to the choice of the interaction metric.

Sleep and behavioral annotations for decoding

We manually annotated parts of the continuous video recordings of the patients in order to assess whether the brain interactions correlated with cognitive state and behavior (**Figure 21**).

Sleep annotations

We selected a random subsample of 14 out of the 48 subjects to continuously annotate whether subjects were awake or asleep. These annotations were based on the video recordings. We also selected a subset of 4 out of these 14 subjects who had scalp EEG recordings to validate the annotations. Two certified sleep clinicians performed sleep and wake annotations based on the scalp EEG recordings in Subjects 5, 8, 14, and 21 for a total of 6 nights of sleep, 47.3 hours. We annotated periods of sleep and wake based on audiovisual recordings in the same subset of data and found good agreement with clinical experts with an overall accuracy of 0.90, true positive rate of 0.96, true negative rate of 0.64, and an inter-rater reliability of 0.66 (Cohen's kappa). We then annotated sleep based on audiovisual recordings for a total of 1362.4 hours in the 14 subjects (97.3 ± 36.0 hours per subject).

Natural behavior annotations

We also annotated naturalistic behaviors from the same audiovisual recordings. We selected a random subset of three subjects. We analyzed a continuous period of 23.8 hours in Subject 14, 24.0 hours in Subject 21, and 13.3 hours in Subject 40 at one-second resolution. We considered four behaviors that were distinct and prevalent in our bedridden subjects: (i): "physical contact", defined as contact between the subject and anyone else in the room (this label was present in a total of 1.5 ± 1.2 hours per subject); (ii) "head movement", defined as movements of the neck or head, excluding facial movements or chewing (1.6 ± 1.3 hours per subject); (iii) "body movement", defined as any movement of the body that was not the head (3.2 ± 0.5 hours per subject); and (iv) "watching TV", defined as a segment when the subject was watching television and paying attention to it (3.0 ± 2.3 hours per subject). These behaviors are not disjoint (that is, a given segment can have more than one label). We used a custom software to show the videos and a graphical user interface for the annotations. Two subjects annotated the videos independently, without consulting with each other. In all, there was a large agreement between the two sets of annotations (88±11 % agreement) and we focused here on those 1-second segments where both annotators agreed.

Classification of sleep and natural behaviors

We used a machine learning approach to assess whether it was possible to decode the annotation labels from the brain interaction data (Kriegeskorte and Kreiman, 2011).

First, we used a nearest neighbor classifier to decode whether the subject was asleep or awake using only the coherence measurements. Each 10-second segment was assigned a binary

label: sleep or awake. Transitions from sleep to wake and vice versa created ambiguous windows and were removed. Since there were more periods of wake than sleep in every subject, the wake labels were randomly subsampled to maintain an equal balance of wake and sleep labels. We used 20-fold cross-validation to separate the data into a training set and a test set, using 400 iterations. We considered all pairwise coherence measurements for each subject. Using only the training data, we selected the top 10 most significant coherence features, based on the p-value of a two-sided ranksum test between awake and sleep states. The results shown in **Figure 21A** represent cross-validated test accuracy values ranging from 0 to 1, where chance=0.5. Statistical significance was determined by comparing the accuracies against those obtained after randomly shuffling the sleep/wake labels. The statistical analyses were corrected for multiple comparisons across subjects by Bonferroni's method.

A similar procedure was followed to decode the 4 naturalistic behaviors. Because these 4 behaviors could have shorter durations than sleep/wake, and even often shorter than the 10-second segments used throughout the study, we recomputed all the coherence values using a window of 2 seconds. We considered segments that had only one annotation and we used binary classification for each behavior, that is, whether the behavior was present or not in each window (e.g. whether the subject was watching TV or not in each segment). The number of positive and negative examples for each behavior was balanced by random subsampling to ensure that chance was 0.5 in each case and the same number of training samples across behaviors. The classifiers were cross-validated and balanced in a similar fashion as for sleep classification.

Conclusion

In this work, we defined a quantitative measure of interactivity between pairs of electrical signals from electrical recordings inside the brain. We demonstrated that our pre-processing pipeline maximized the temporal and spatial sensitivity of the coherence metric. Our definition of physiological interactions was shown to be free from methodological artifacts and demonstrated both anatomical and physiological correlations in a macaque monkey model. Our network of interactions was found to be small-world and interaction weights demonstrated log-normal distributions. We showed that these main results were robust to our choice of subjects, durations of recording, interactivity metric, and frequency bands. In a subset of our dataset, we annotated whether subjects were sleeping and whether they were performing a range of naturalistic behaviors. We showed that our interaction metric was able to decode sleep vs. wake, and the engagement of each of four behaviors.

To share our results in an accessible format, we performed unsupervised clustering to delineate a 150-area parcellation of the human brain and built an interactive website which allows users to easily scrutinize each interaction in detail. In sum, these efforts represent an advancement in our understanding of mesoscopic networks in the human brain. We anticipate that the research community will be glad to find these data in an easily accessible format, and that these characterizations will be useful in our ongoing quest to unlock the mysteries of the brain.

Appendix

Interactive web atlas

The accompanying website provides three-dimensional renderings of the electrode locations for each subject (http://braininteractome.com). A step-by-step tutorial introduces all features of the interactive atlas. Briefly, interactions may be viewed as measured by the coherence in each of five frequency bands. Subject-averaged coherence matrices may be re-rendered using one of four available parcellations. The matrix view highlights interactions in the three-dimensional view. Hovering over interactions shows detailed statistics of each interaction. We hope this resource may facilitate researchers in the general neuroscience community.

Data and code download

All data and code used in this study are available upon request. Additionally, code and sample data are freely available online (https://github.com/kreimanlab/MesoscopicInteractions) via the GPLv3 open-source license. The provided scripts can generate all figures in this dissertation starting from raw intracranial EEG recordings.

Brain oscillations during sleep

This work was done jointly with Annabelle Tao, Faculty of Arts and Sciences

Intracranial signals recorded during sleep have been described to travel in macro-scale waves (Muller et al., 2016). We characterized oscillations in the broadband power in our dataset of 14 subjects with sleep annotations. We show a 12-hour segment of IFP signal and its broadband power from an electrode in the Superior Frontal Gyrus in **Figure A1**. Overall, 673 out of 1034 electrodes (65%) showed significant decoding accuracy. The average decoding accuracy was: 0.62 ± 0.067, range 0.51 to 0.84 (**Figure A1B**).

We mapped the significant electrodes to Desikan-Killiany regions (Desikan et al., 2006). We had adequate electrode coverage in 25 out of 36 ROIs. We show the electrode location and decoding accuracy per ROI in **Figure A1C**. The correlation between the number of significant electrodes in a region and the average decoding accuracy of that region was not significant (Spearman's $\rho = -0.07$, $p = 0.74$). The summary of decoding accuracy across frequency bands is shown in **Figure A1D**.

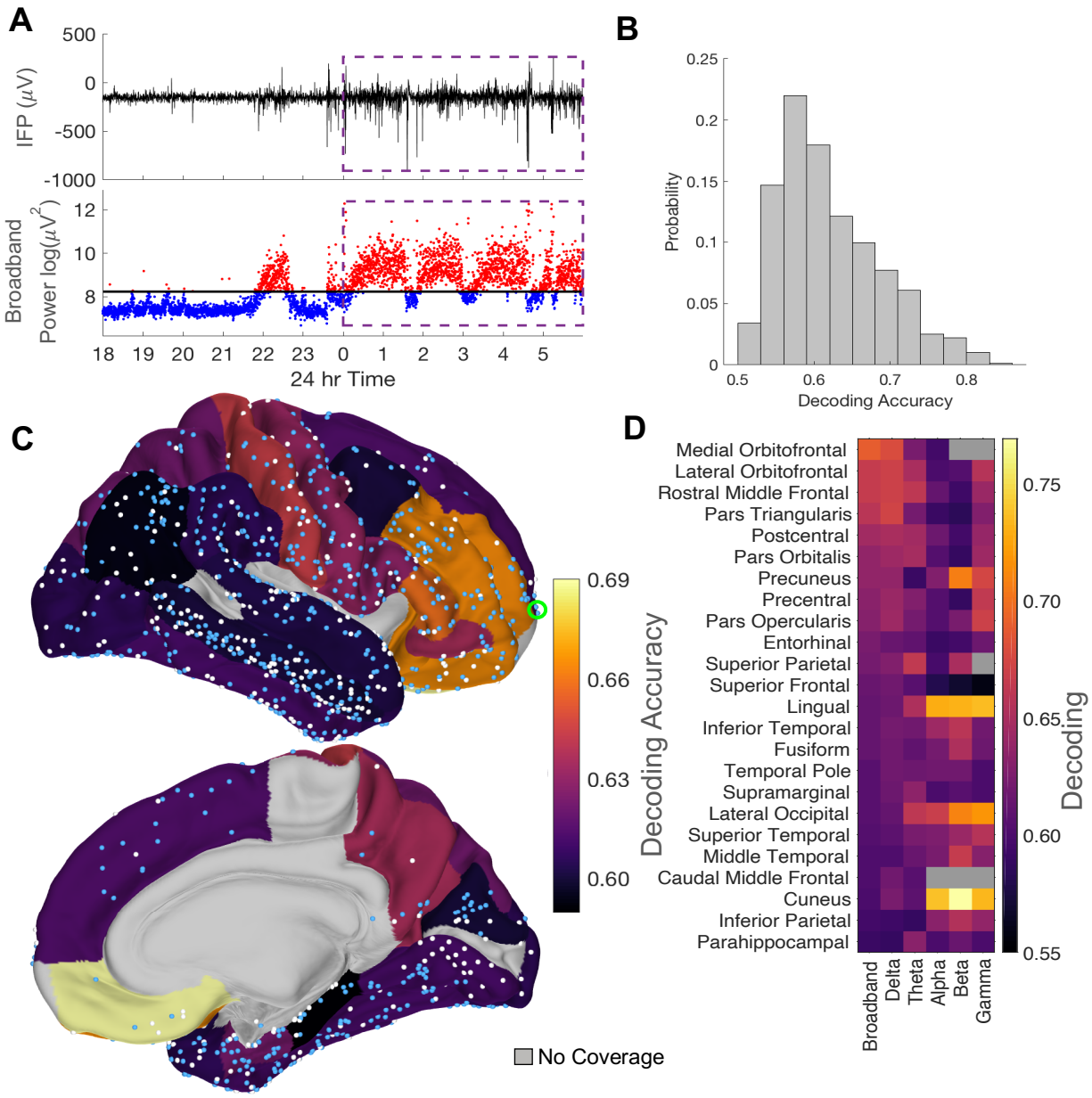

Figure A1: Intracranial field potentials at different frequency bands revealed differences between sleep and wake. (**A**) Top panel: 12-hours of intracranial field potential (IFP) signal from an electrode in the superior frontal cortex (circled in green in **C**). Bottom Panel: We calculated the broadband power of every 10-second segment of the IFP signal and trained support vector machines (SVMs) to classify sleep and wake based on frequency band power (Methods). The decision boundary for this electrode is shown as a horizontal black line. Data points that were classified as wake are blue, data points that were classified as sleep are red. The decoding accuracy of the SVM was 0.84 for this 12-hr segment and 0.74 for the entire recording (chance = 0.5). (**B**) Distribution of broadband decoding accuracy for all electrodes with significant performance (n=673 electrodes, bin size = 0.03). The average decoding accuracy over all electrodes was 0.62 ± 0.07. (**C**) Location of 673 electrodes with significant decoding accuracy (blue) and not-significant electrodes (n=361, white) depicted on a common brain. For

visualization purposes, electrodes on the left hemisphere are replotted onto the right hemisphere. Each Desikan-Killiany region is colored according to the average decoding accuracy of all significant electrodes in that region. Regions without coverage are shown in gray. **(D)** Average decoding accuracy for significant regions (rows) in each frequency band (columns). Regions are sorted by broadband decoding accuracy. See color scale on right.

Methods

Preprocessing: When computing frequency band power, we handled artifacts as follows. The detection process described in "Signal Preprocessing: Artifact Removal" marked 1-second segments as artifacts. Frequency band power was calculated for 10-second segments. If more than 1 second of the 10-second window was marked as an artifact, then we removed the entire 10-second window from analysis.

After computing the frequency band power, we preprocessed the frequency band power to remove anomalous data segments. For every 10-minute window of the data, we removed it if (1) greater than or equal to 10% of its component 1-second windows were marked as artifacts, or (2) greater than 50% of the window is below the power threshold. The power threshold was defined as $\bar{x} - 2\sigma$ where $\bar{x}$ is the signal mean and σ is the standard deviation. Time windows flagged were excluded from the remaining analysis (5.2% removed total).

Electrodes showing significant differences between sleep and wake in different frequency bands: To determine whether frequency band power was significantly different between sleep and wake, we conducted a permutation test for each frequency band in each electrode. We tested whether the difference in frequency band power during sleep and wake is the same as the difference in

frequency band power between two random subsets of the data. More precisely, let X be the power in a frequency band for an electrode. Let $\bar{x}_s$ and $\bar{x}_w$ be the average power during sleep and wake respectively. Let R be a random partition of X into two subsets: X_R and $X_{\neg R}$ with sample averages $\bar{x}_R$ and $\bar{x}_{\neg R}$. The number of elements in X_R is the same as the number of windows annotated as sleep for that subject after preprocessing. Let D be the distribution of $\bar{x}_R - \bar{x}_{\neg R}$. Our null hypothesis was that $\bar{x}_s - \bar{x}_w$ comes from D.

To test the null hypothesis, we created a null distribution by calculating $\bar{x}_R - \bar{x}_{\neg R}$ for 100,000 permutations. We used the null distribution to create a significance threshold for each frequency band in each electrode. We will refer to these electrodes with significantly different frequency band power during sleep and wake as "significant frequency band power electrodes."

For all significant frequency band power electrodes, we z-scored the frequency band power and calculated the mean and standard deviation of the difference in power between sleep and wake.

Frequency Decoding: To assess whether we could decode sleep and wake from IFPs, we used the frequency band power to train support vector machine (SVMs) with a linear kernel. One SVM was trained per frequency band per electrode (1,034 electrodes × 7 frequency bands = 7,238 SVMs total). To train the SVMs, we used the Matlab function *fitcsvm* with the following parameters: "standardize" was set to "true" so that the training data was z-scored prior to training, and "OptimizeHyperparameters" set to auto in order to optimize the box constraint and kernel scale.

To prevent overfitting, we trained the SVM on the first half of the data set and tested its performance on the second half of the dataset. Each SVM had one feature: a frequency band's power in one electrode during the first half of the subject's recording. The SVMs were trained to classify sleep and wake based on our sleep annotations for that half of the data.

We calculated SVM accuracy as follows:

i) We randomly selected time indices from the second half of the dataset. The indices were selected so that chance accuracy = 0.5.

ii) We used the trained SVM to classify those indices as sleep or wake.

iii) Then, we calculated the SVM's accuracy by computing their agreement with the sleep annotations.

We repeated i – iii ten times, and report the mean value as the accuracy.

We used a permutation test to evaluate whether an SVM achieved significant decoding accuracy (Combrisson and Jerbi, 2015; Meyers and Kreiman, 2011; Ojala and Garriga, 2010). Our null hypothesis was that the SVM performed as well as a classifier that randomly labeled each one-hour segment as sleep or wake. We created a null distribution as follows:

i) We divided the second half of the dataset into one-hour segments. We randomly labeled each one-hour segment as sleep or wake

ii) We randomly selected time indices from the second half of the dataset. The indices were labeled based on the labels generated in i).

iii) We computed the agreement of these labels with the sleep annotations. This gave us an accuracy value.

iv) We repeated ii)-iii) ten times and averaged over the ten accuracy values.

We repeated i – iv 10^4 times, resulting in a null distribution. We performed a one-sided significance test, Bonferroni correcting for the number of electrodes in each subject. We refer to electrodes with significant decoding accuracy as "significant frequency decoding electrodes."

We checked whether the classifiers captured differences in frequency band power. We calculated the correlation between the absolute value of the difference in frequency band power and the decoding accuracy for electrodes that showed both significant decoding and significant differences in power (**Figure A1**).

ROI: We calculated the classification accuracy for each ROI by averaging the classification accuracy for all significant frequency decoding electrodes in that ROI (**Figure A1**). Electrode placement varied from subject to subject. For robustness, we only considered ROIs that contained ≥ 4 significant frequency decoding electrodes from ≥ 2 subjects.

References

Anumanchipalli, G.K., Chartier, J., and Chang, E.F. (2019). Speech synthesis from neural decoding of spoken sentences. Nature *568*, 493-498.

Assaf, Y., and Pasternak, O. (2008). Diffusion Tensor Imaging (DTI)-based White Matter Mapping in Brain Research: A Review. Journal of Molecular Neuroscience *34*, 51-61.

Baldauf, D., and Desimone, R. (2014). Neural Mechanisms of Object-Based Attention. Science *344*, 424.

Bansal, A.K., Madhavan, R., Agam, Y., Golby, A., Madsen, J.R., and Kreiman, G. (2014). Neural Dynamics Underlying Target Detection in the Human Brain. The Journal of Neuroscience *34*, 3042.

Barabási, A.-L., and Albert, R. (1999). Emergence of Scaling in Random Networks. Science *286*, 509-512.

Bassett, D.S., and Bullmore, E.T. (2017). Small-World Brain Networks Revisited. The Neuroscientist *23*, 499-516.

Bassett, D.S., and Sporns, O. (2017). Network neuroscience. Nature Neuroscience *20*, 353-364.

Bastos, André M., Vezoli, J., Bosman, Conrado A., Schoffelen, J.-M., Oostenveld, R., Dowdall, Jarrod R., De Weerd, P., Kennedy, H., and Fries, P. (2015). Visual Areas Exert Feedforward and Feedback Influences through Distinct Frequency Channels. Neuron *85*, 390-401.

Betzel, R.F., Medaglia, J.D., Kahn, A.E., Soffer, J., Schonhaut, D.R., and Bassett, D.S. (2019). Structural, geometric and genetic factors predict interregional brain connectivity patterns probed by electrocorticography. Nature Biomedical Engineering *3*, 902-916.

Bullmore, E., and Sporns, O. (2009). Complex brain networks: graph theoretical analysis of structural and functional systems. Nature Reviews Neuroscience *10*, 186-198.

Bullmore, E., and Sporns, O. (2012). The economy of brain network organization. Nature Reviews Neuroscience *13*, 336-349.

Burkhalter, A., and Bernardo, K.L. (1989). Organization of corticocortical connections in human visual cortex. Proceedings of the National Academy of Sciences *86*, 1071-1075.

Buzsaki, G. (2006). Rhythms of the Brain (Oxford University Press).

Buzsáki, G. (2013). Time, space and memory. Nature *497*, 568-569.

Buzsáki, G. (2019). The brain from inside out (Oxford University Press).

Buzsáki, G., Anastassiou, C.A., and Koch, C. (2012). The origin of extracellular fields and currents — EEG, ECoG, LFP and spikes. Nature Reviews Neuroscience *13*, 407.

Buzsáki, G., and Mizuseki, K. (2014). The log-dynamic brain: how skewed distributions affect network operations. Nature Reviews Neuroscience *15*, 264-278.

Casimo, K., Darvas, F., Wander, J., Ko, A., Grabowski, T.J., Novotny, E., Poliakov, A., Ojemann, J.G., and Weaver, K.E. (2016). Regional Patterns of Cortical Phase Synchrony in the Resting State. Brain Connectivity *6*, 470-481.

Churchland, P.S. (1992). The computational brain (Cambridge, Mass.: MIT Press).

Combrisson, E., and Jerbi, K. (2015). Exceeding chance level by chance: The caveat of theoretical chance levels in brain signal classification and statistical assessment of decoding accuracy. Journal of neuroscience methods *250*, 126-136.

Crone, N.E., Sinai, A., and Korzeniewska, A. (2006). High-frequency gamma oscillations and human brain mapping with electrocorticography. In Progress in Brain Research, C. Neuper, and W. Klimesch, eds. (Elsevier), pp. 275-295.

Dale, A.M., Fischl, B., and Sereno, M.I. (1999). Cortical Surface-Based Analysis: I. Segmentation and Surface Reconstruction. NeuroImage *9*, 179-194.

Danker-Hopfe, H., Anderer, P., Zeitlhofer, J., Boeck, M., Dorn, H., Gruber, G., Heller, E., Loretz, E., Moser, D., Parapatics, S.*, et al.* (2009). Interrater reliability for sleep scoring according to the Rechtschaffen & Kales and the new AASM standard. Journal of Sleep Research *18*, 74-84.

Desikan, R.S., Ségonne, F., Fischl, B., Quinn, B.T., Dickerson, B.C., Blacker, D., Buckner, R.L., Dale, A.M., Maguire, R.P., Hyman, B.T.*, et al.* (2006). An automated labeling system for subdividing the human cerebral cortex on MRI scans into gyral based regions of interest. NeuroImage *31*, 968-980.

Dubey, A., and Ray, S. (2016). Spatial spread of local field potential is band-pass in the primary visual cortex. Journal of Neurophysiology *116*, 1986-1999.

Dubey, A., and Ray, S. (2019). Cortical Electrocorticogram (ECoG) is a local signal. The Journal of Neuroscience *39*, 2917-2918.

Dzwonczyk, R., Fujii, J.T., Simonetti, O., Nieves-Ramos, R., and Bergese, S.D. (2009). Electrical Noise in the Intraoperative Magnetic Resonance Imaging Setting. Anesthesia & Analgesia *108*, 181-186.

Ercsey-Ravasz, M., Nikola, Lamy, C., David, Knoblauch, K., Toroczkai, Z., and Kennedy, H. (2013). A Predictive Network Model of Cerebral Cortical Connectivity Based on a Distance Rule. *80*, 184-197.

Felleman, D.J., and Van Essen, D.C. (1991). Distributed hierarchical processing in the primate cerebral cortex. Cereb Cortex *1*, 1-47.

Fox, K.C.R., Shi, L., Baek, S., Raccah, O., Foster, B.L., Saha, S., Margulies, D.S., Kucyi, A., and Parvizi, J. (2020). Intrinsic network architecture predicts the effects elicited by intracranial electrical stimulation of the human brain. Nature Human Behaviour.

Fried, I., Rutishauser, U., Cerf, M., and Kreiman, G. (2014). Single Neuron Studies of the Human Brain: Probing Cognition (The MIT Press).

Fries, P. (2005). A mechanism for cognitive dynamics: neuronal communication through neuronal coherence. Trends in Cognitive Sciences *9*, 474-480.

Fu, Z., Wu, D.-A.J., Ross, I., Chung, J.M., Mamelak, A.N., Adolphs, R., and Rutishauser, U. (2019). Single-Neuron Correlates of Error Monitoring and Post-Error Adjustments in Human Medial Frontal Cortex. Neuron *101*, 165-177.e165.

Gămănuţ, R., Kennedy, H., Toroczkai, Z., Ercsey-Ravasz, M., Van Essen, D.C., Knoblauch, K., and Burkhalter, A. (2018). The Mouse Cortical Connectome, Characterized by an Ultra-Dense Cortical Graph, Maintains Specificity by Distinct Connectivity Profiles. Neuron *97*, 698-715.e610.

Glasser, M.F., Coalson, T.S., Robinson, E.C., Hacker, C.D., Harwell, J., Yacoub, E., Ugurbil, K., Andersson, J., Beckmann, C.F., Jenkinson, M.*, et al.* (2016). A multi-modal parcellation of human cerebral cortex. Nature *536*, 171.

Graham, D.J. (2021). An Internet in Your Head (Columbia University Press).

Gregoriou, G.G., Gotts, S.J., Zhou, H., and Desimone, R. (2009). High-Frequency, Long-Range Coupling Between Prefrontal and Visual Cortex During Attention. Science *324*, 1207.

Groppe, D.M., Bickel, S., Dykstra, A.R., Wang, X., Mégevand, P., Mercier, M.R., Lado, F.A., Mehta, A.D., and Honey, C.J. (2017). iELVis: An open source MATLAB toolbox for localizing and visualizing human intracranial electrode data. Journal of Neuroscience Methods *281*, 40-48.

Grossman, S., Gaziv, G., Yeagle, E.M., Harel, M., Mégevand, P., Groppe, D.M., Khuvis, S., Herrero, J.L., Irani, M., Mehta, A.D.*, et al.* (2019). Convergent evolution of face spaces across human face-selective neuronal groups and deep convolutional networks. Nature Communications *10*.

Humphries, M.D., and Gurney, K. (2008). Network 'Small-World-Ness': A Quantitative Method for Determining Canonical Network Equivalence. PLOS ONE *3*, e0002051.

Hutchison, R.M., Womelsdorf, T., Allen, E.A., Bandettini, P.A., Calhoun, V.D., Corbetta, M., Della Penna, S., Duyn, J.H., Glover, G.H., Gonzalez-Castillo, J.*, et al.* (2013). Dynamic functional connectivity: Promise, issues, and interpretations. NeuroImage *80*, 360-378.

Iaselli, E., Kreiman, G., and Herzog, M. (2018). 24 hours in the human brain.

Jones, E., Oliphant, T., and Peterson, P. (2001). {SciPy}: Open source scientific tools for {Python}.

Kajikawa, Y., and Schroeder, Charles E. (2011). How Local Is the Local Field Potential? Neuron *72*, 847-858.

Kasthuri, N., Kenneth, Daniel, Richard, José, Knowles-Barley, S., Lee, D., Vázquez-Reina, A., Kaynig, V., Thouis*, et al.* (2015). Saturated Reconstruction of a Volume of Neocortex. Cell *162*, 648-661.

Keller, C.J., Honey, C.J., Entz, L., Bickel, S., Groppe, D.M., Toth, E., Ulbert, I., Lado, F.A., and Mehta, A.D. (2014). Corticocortical Evoked Potentials Reveal Projectors and Integrators in Human Brain Networks. Journal of Neuroscience *34*, 9152-9163.

Kramer, M.A., Eden, U.T., Lepage, K.Q., Kolaczyk, E.D., Bianchi, M.T., and Cash, S.S. (2011). Emergence of Persistent Networks in Long-Term Intracranial EEG Recordings. The Journal of Neuroscience *31*, 15757-15767.

Kriegeskorte, N., and Kreiman, G. (2011). Visual Population Codes, Towards a Common Multivariate Framework for Cell Recording and Functional Imaging (MIT Press).

Liégeois, R., Laumann, T.O., Snyder, A.Z., Zhou, J., and Yeo, B.T.T. (2017). Interpreting temporal fluctuations in resting-state functional connectivity MRI. NeuroImage *163*, 437-455.

Liu, H., Agam, Y., Madsen, J.R., and Kreiman, G. (2009). Timing, Timing, Timing: Fast Decoding of Object Information from Intracranial Field Potentials in Human Visual Cortex. Neuron *62*, 281-290.

Logothetis, N.K., Pauls, J., Augath, M., Trinath, T., and Oeltermann, A. (2001). Neurophysiological investigation of the basis of the fMRI signal. Nature *412*, 150-157.

Madhavan, R., Bansal, A.K., Madsen, J.R., Golby, A.J., Tierney, T.S., Eskandar, E.N., Anderson, W.S., and Kreiman, G. (2019). Neural Interactions Underlying Visuomotor Associations in the Human Brain. Cerebral Cortex *29*, 4551-4567.

Magalang, U.J., Chen, N.-H., Cistulli, P.A., Fedson, A.C., Gíslason, T., Hillman, D., Penzel, T., Tamisier, R., Tufik, S., Phillips, G.*, et al.* (2013). Agreement in the Scoring of Respiratory Events and Sleep Among International Sleep Centers. Sleep *36*, 591-596.

Markov, N.T., Ercsey-Ravasz, M., Lamy, C., Ribeiro Gomes, A.R., Magrou, L., Misery, P., Giroud, P., Barone, P., Dehay, C., Toroczkai, Z.*, et al.* (2013a). The role of long-range connections on the specificity of the macaque interareal cortical network. Proceedings of the National Academy of Sciences *110*, 5187-5192.

Markov, N.T., Ercsey-Ravasz, M., Van Essen, D.C., Knoblauch, K., Toroczkai, Z., and Kennedy, H. (2013b). Cortical High-Density Counterstream Architectures. Science *342*, 1238406-1238406.

Markov, N.T., Ercsey-Ravasz, M.M., Ribeiro Gomes, A.R., Lamy, C., Magrou, L., Vezoli, J., Misery, P., Falchier, A., Quilodran, R., Gariel, M.A.*, et al.* (2012). A Weighted and Directed Interareal Connectivity Matrix for Macaque Cerebral Cortex. Cerebral Cortex *24*, 17-36.

Meyers, E., and Kreiman, G. (2011). Understanding Visual Population Code.

Michalareas, G., Vezoli, J., Stan, Schoffelen, J.-M., Kennedy, H., and Fries, P. (2016). Alpha-Beta and Gamma Rhythms Subserve Feedback and Feedforward Influences among Human Visual Cortical Areas. Neuron *89*, 384-397.

Miller, K.J., Sorensen, L.B., Ojemann, J.G., and Den Nijs, M. (2009). Power-Law Scaling in the Brain Surface Electric Potential. PLoS Computational Biology *5*, e1000609.

Mountcastle, V. (1997). The columnar organization of the neocortex. Brain *120*, 701-722.

Muldoon, S.F., Bridgeford, E.W., and Bassett, D.S. (2016). Small-World Propensity and Weighted Brain Networks. *6*, 22057.

Muller, L., Piantoni, G., Koller, D., Cash, S.S., Halgren, E., and Sejnowski, T.J. (2016). Rotating waves during human sleep spindles organize global patterns of activity that repeat precisely through the night. eLife *5*.

Nassi, J.J., Lomber, S.G., and Born, R.T. (2013). Corticocortical Feedback Contributes to Surround Suppression in V1 of the Alert Primate. *33*, 8504-8517.

Newman, M.E.J. (2001). Scientific collaboration networks. II. Shortest paths, weighted networks, and centrality. Physical Review E *64*.

Nolte, G., Bai, O., Wheaton, L., Mari, Z., Vorbach, S., and Hallett, M. (2004). Identifying true brain interaction from EEG data using the imaginary part of coherency. Clinical Neurophysiology *115*, 2292-2307.

Nunez, P.L., Srinivasan, R., Westdorp, A.F., Wijesinghe, R.S., Tucker, D.M., Silberstein, R.B., and Cadusch, P.J. (1997). EEG coherency: I: statistics, reference electrode, volume conduction, Laplacians, cortical imaging, and interpretation at multiple scales. Electroencephalography and Clinical Neurophysiology *103*, 499-515.

Ojala, M., and Garriga, G.C. (2010). Permutation tests for studying classifier performance. Journal of Machine Learning Research *11*.

Onnela, J.-P., Saramäki, J., Kertész, J., and Kaski, K. (2005). Intensity and coherence of motifs in weighted complex networks. Physical Review E *71*.

Opanchuk, B. (2014). Reikna, the pure python gpgpu library.

Parvizi, J., and Kastner, S. (2018). Promises and limitations of human intracranial electroencephalography. Nature Neuroscience *21*, 474-483.

Penfield, W., and Rasmussen, T. (1950). The cerebral cortex of man; a clinical study of localization of function.

Petersen, S., and Sporns, O. (2015). Brain Networks and Cognitive Architectures. Neuron *88*, 207-219.

Power, J.D., Cohen, A.L., Nelson, S.M., Wig, G.S., Barnes, K.A., Church, J.A., Vogel, A.C., Laumann, T.O., Miezin, F.M., Schlaggar, B.L.*, et al.* (2011). Functional Network Organization of the Human Brain. Neuron *72*, 665-678.

Reid, A.T., Headley, D.B., Mill, R.D., Sanchez-Romero, R., Uddin, L.Q., Marinazzo, D., Lurie, D.J., Valdés-Sosa, P.A., Hanson, S.J., Biswal, B.B.*, et al.* (2019). Advancing functional connectivity research from association to causation. Nature Neuroscience *22*, 1751-1760.

Schwiedrzik, C.M., Sudmann, S.S., Thesen, T., Wang, X., Groppe, D.M., Mégevand, P., Doyle, W., Mehta, A.D., Devinsky, O., and Melloni, L. (2018). Medial prefrontal cortex supports perceptual memory. Current Biology *28*, R1094-R1095.

Shirhatti, V., Borthakur, A., and Ray, S. (2016). Effect of Reference Scheme on Power and Phase of the Local Field Potential. Neural Computation *28*, 882-913.

Solomon, E.A., Kragel, J.E., Sperling, M.R., Sharan, A., Worrell, G., Kucewicz, M., Inman, C.S., Lega, B., Davis, K.A., Stein, J.M.*, et al.* (2017). Widespread theta synchrony and high-frequency desynchronization underlies enhanced cognition. Nature Communications *8*.

Sparks, D.L., Lue, L.-F., Martin, T.A., and Rogers, J. (2000). Neural tract tracing using Di-I: a review and a new method to make fast Di-I faster in human brain. Journal of Neuroscience Methods *103*, 3-10.

Sporns, O., Tononi, G., and Kötter, R. (2005). The Human Connectome: A Structural Description of the Human Brain. PLoS Computational Biology *1*, e42.

Stepaniants, G., Brunton, B.W., and Kutz, J.N. (2020). Inferring causal networks of dynamical systems through transient dynamics and perturbation. Physical Review E *102*.

Steven, and Sporns, O. (2015). Brain Networks and Cognitive Architectures. Neuron *88*, 207-219.

Tang, H., Buia, C., Madhavan, R., Crone, Nathan E., Madsen, Joseph R., Anderson, William S., and Kreiman, G. (2014). Spatiotemporal Dynamics Underlying Object Completion in Human Ventral Visual Cortex. Neuron *83*, 736-748.

Teillac, A., Hou, Y., Magrou, L., Lamy, C., Misery, P., Richard, N., Descoteaux, M., Ye, C., Shen, Z., Knoblauch, K.*, et al.* (2019). Within Animal Comparison of Tract-tracing and High Resolution Tractography Yields High Correlations. Paper presented at: Organization for Human Brain Mapping (Rome, Italy).

Telesford, Q.K., Joyce, K.E., Hayasaka, S., Burdette, J.H., and Laurienti, P.J. (2011). The Ubiquity of Small-World Networks. Brain Connectivity *1*, 367-375.

Thomas Yeo, B.T., Krienen, F.M., Sepulcre, J., Sabuncu, M.R., Lashkari, D., Hollinshead, M., Roffman, J.L., Smoller, J.W., Zöllei, L., Polimeni, J.R.*, et al.* (2011). The organization of the human cerebral cortex estimated by intrinsic functional connectivity. Journal of Neurophysiology *106*, 1125-1165.

Trebaul, L., Deman, P., Tuyisenge, V., Jedynak, M., Hugues, E., Rudrauf, D., Bhattacharjee, M., Tadel, F., Chanteloup-Foret, B., Saubat, C.*, et al.* (2018). Probabilistic functional tractography of the human cortex revisited. NeuroImage *181*, 414-429.

Van Essen, D.C. (2004). Surface-based approaches to spatial localization and registration in primate cerebral cortex. *23*, S97-S107.

Van Essen, D.C. (2005). A Population-Average, Landmark- and Surface-based (PALS) atlas of human cerebral cortex. NeuroImage *28*, 635-662.

Van Essen, D.C., and Dierker, D.L. (2007). Surface-Based and Probabilistic Atlases of Primate Cerebral Cortex. Neuron *56*, 209-225.

Van Essen, D.C., Drury, H.A., Dickson, J., Harwell, J., Hanlon, D., and Anderson, C.H. (2001). An Integrated Software Suite for Surface-based Analyses of Cerebral Cortex. Journal of the American Medical Informatics Association *8*, 443-459.

Van Essen, D.C., Smith, S.M., Barch, D.M., Behrens, T.E.J., Yacoub, E., and Ugurbil, K. (2013). The WU-Minn Human Connectome Project: An overview. NeuroImage *80*, 62-79.

Vidal, J., Ossandón, T., Jerbi, K., Dalal, S., Minotti, L., Ryvlin, P., Kahane, P., and Lachaux, J.-P. (2010). Category-Specific Visual Responses: An Intracranial Study Comparing Gamma, Beta, Alpha, and ERP Response Selectivity. Frontiers in Human Neuroscience *4*.

Wang, N., Farhadi, A., Rao, R., and Brunton, B. (2018). AJILE Movement Prediction: Multimodal Deep Learning for Natural Human Neural Recordings and Video. Proceedings of the AAAI Conference on Artificial Intelligence *32*.

Wang, N.X.R., Olson, J.D., Ojemann, J.G., Rao, R.P.N., and Brunton, B.W. (2016). Unsupervised Decoding of Long-Term, Naturalistic Human Neural Recordings with Automated Video and Audio Annotations. Frontiers in Human Neuroscience *10*.

Ward, J.H. (1963). Hierarchical Grouping to Optimize an Objective Function. Journal of the American Statistical Association *58*, 236-244.

Watts, D.J., and Strogatz, S.H. (1998). Collective dynamics of 'small-world' networks. Nature *393*, 440-442.

Welch, P. (1967). The use of fast Fourier transform for the estimation of power spectra: A method based on time averaging over short, modified periodograms. IEEE Transactions on Audio and Electroacoustics *15*, 70-73.

Wesenberg, J. (2016). TubePlot: Construct a tube, or warped cylinder, along any 3D curve. MATLAB Central File Exchange.

Womelsdorf, T., Schoffelen, J.M., Oostenveld, R., Singer, W., Desimone, R., Engel, A.K., and Fries, P. (2007). Modulation of Neuronal Interactions Through Neuronal Synchronization. Science *316*, 1609-1612.

Yanagawa, T., Chao, Z.C., Hasegawa, N., and Fujii, N. (2013). Large-Scale Information Flow in Conscious and Unconscious States: an ECoG Study in Monkeys. PLOS ONE *8*, e80845.

Zalesky, A., Fornito, A., Cocchi, L., Gollo, L.L., and Breakspear, M. (2014). Time-resolved resting-state brain networks. Proceedings of the National Academy of Sciences *111*, 10341-10346.

Zhao, Q. (2016). Computational and Cognitive Neuroscience of Vision (Springer).

Zhou, H., Schafer, Robert J., and Desimone, R. (2016). Pulvinar-Cortex Interactions in Vision and Attention. Neuron *89*, 209-220.